Titre: Title:	In-Situ Mechanical Properties Identification of Composite Materials Using Inverse Methods Based on Full-Field Measurements
Auteur: Author:	Behzad Rahmani
Date:	2014
Type:	Mémoire ou thèse / Dissertation or Thesis
Référence: Citation:	Rahmani, B. (2014). In-Situ Mechanical Properties Identification of Composite Materials Using Inverse Methods Based on Full-Field Measurements [Thèse de doctorat, École Polytechnique de Montréal]. PolyPublie. https://publications.polymtl.ca/1411/

UNIVERSITÉ DE MONTRÉAL

IN-SITU MECHANICAL PROPERTIES IDENTIFICATION OF COMPOSITE MATERIALS USING INVERSE METHODS BASED ON FULL-FIELD MEASUREMENTS

BEHZAD RAHMANI
DÉPARTEMENT DE GÉNIE MÉCANIQUE
ÉCOLE POLYTECHNIQUE DE MONTRÉAL

THÈSE PRÉSENTÉE EN VUE DE L'OBTENTION
DU DIPLÔME DE PHILOSOPHIÆ DOCTOR
(GÉNIE MÉCANIQUE)
AVRIL 2014

UNIVERSITÉ DE MONTRÉAL

ÉCOLE POLYTECHNIQUE DE MONTRÉAL

Cette thèse intitulée :

IN-SITU MECHANICAL PROPERTIES IDENTIFICATION OF COMPOSITE MATERIALS USING INVERSE METHODS BASED ON FULL-FIELD MEASUREMENTS

présentée par : RAHMANI Behzad
en vue de l'obtention du diplôme de : Philosophiæ Doctor
a été dûment acceptée par le jury d'examen constitué de :

M. THERRIAULT Daniel, Ph.D., président
M. LÉVESQUE Martin, Ph.D., membre et directeur de recherche
Mme VILLEMURE Isabelle, Ph.D., membre et codirectrice de recherche
M. LE DIGABEL Sébastien, Ph.D., membre
M. GRÉDIAC Michel, Doct., membre

DEDICATION

To my parents :

Raheleh and Davood

To my wife :

Mahnaz

To my whole family . . .

ACKNOWLEDGEMENTS

I would like to take this opportunity to express my deepest gratitude to my supervisors, Professor Martin Lévesque and Professor Isabelle Villemure, for their guidance and support during this research work. Their great interest and constructive ideas encouraged me to be creative and persistent at different stages of this research.

I gratefully acknowledge Farhad Mortazavi, my recently graduated colleague from École Polytechnique de Montréal, for his contributions and advices and for providing the required data during our closely related works. I would also like to thank Elias Ghossein at École Polytechnique de Montréal for feeding this research with very interesting numerical data necessary for the evaluations. Many thanks also goes to Professor Fabrice Pierron from the University of Southampton and Professor Charles Audet from École Polytechnique de Montréal for their fruitful comments about the work.

A great thank you goes to all my colleagues in office A-114, especially to Ali Shahvarpour for the fruitful discussions we had everyday and to Anne-Laure Menard for her great helps and comments that improved my French writings.

I would like to thank the Fonds Québécois de la Recherche sur la Nature et les Technologies (FQRNT) for the financial support that made this project possible.

Finally and most importantly, I would like to express my gratitude to my family : to my beloved, Mahnaz, for her unwavering love, quiet patience and encouragements as an extraordinary wife, and last but not the least, to my parents who provided unconditional supports throughout my educations and devoted all their life to my success. I wish you health and happiness during the rest of your life.

RÉSUMÉ

Des essais homogènes macroscopiques, tels que les tests classiques de tension et de compression, peuvent être réalisés pour obtenir une mesure des propriétés moyennes d'un composite donné. Cependant, ces tests ne permettent pas d'identifier les paramètres mécaniques in situ des phases constitutives ou encore de l'interface d'adhésion entre la matrice et les fibres. Grâce aux avancées récentes au niveau des appareils optiques et des technologies d'imagerie, plusieurs techniques de mesures en champ complet telle que la Corrélation d'Images Numériques (CIN) et la Corrélation de Volumes Numériques (CVN) ont fait leur apparition. Ces techniques permettent la quantification des champs de déplacements/déformations en 2D ou 3D sur la surface ou même à l'intérieur d'un matériau opaque soumis à des chargements externes. La disponibilité de telles informations a permis le développement de différentes méthodes inverses d'identification de paramètres des matériaux. Parmi ces dernières, l'Actualisation du Modèle Éléments Finis (AMÉF) et la Méthode des Champs Virtuels (MCV) ont été grandement exploitées. L'utilisation combinée d'une technique de mesure en champ complet et d'une méthode d'identification inverse constitue une stratégie très prometteuse pour identifier simultanément plusieurs propriétés mécaniques locales.

L'objectif principal de cette thèse était de développer et d'améliorer des approches inverses en 2D et en 3D, étant efficaces à la fois en termes de précision et de temps de calcul. Les approches développées ont été validées en réalisant différentes expériences virtuelles permettant l'identification des propriétés mécaniques locales de composites avec diverses caractéristiques mécaniques et morphologiques.

En premier lieu, un algorithme inverse basé sur la technique d'Actualisation du Modèle Éléments Finis (AMÉF) a été développé et ensuite amélioré. L'amélioration a d'abord consisté à utiliser une technique d'optimisation hybride, i.e. combinaison d'une méthode globale sans dérivées et d'une méthode d'optimisation de premier ordre, afin d'augmenter la précision des paramètres identifiés. De plus, une série de contraintes mécaniquement pertinentes, comprenant un modèle d'homogénéisation approprié, a été ajoutée pour régulariser le problème d'identification. La fonctionnalité de cette nouvelle approche numérique et analytique, à savoir l'Actualisation du Modèle Régularisé (AMR), a été comparée à celle de la AMÉF en présence de champs de déplacements bruités de composites unidirectionnels à fibres longues.

En second lieu, une nouvelle approche basée sur la Méthode de Champs Virtuels (MCV) a été développée pour concilier précision et efficacité numérique. La nouveauté de cette Méthode de Champs Virtuels Régularisée (MCVR) est qu'une régularisation, similaire à celle

de l'AMR, a été introduite dans la formulation classique de la MCV. L'évaluation sur des expériences simulées a révélé que la MCVR est plus robuste que la MCV en présence de bruit. En outre, la MCVR a conduit à une précision de résultats semblable à celle de l'approche AMR, mais pour un temps de calcul significativement plus court. De plus, la taille optimale de la région d'intérêt a été déterminée en considérant un compromis raisonnable entre les besoins de magnification de la CIN pour mieux obtenir les hétérogénéités de déformation et la précision des paramètres identifiés.

En dernier lieu, la MCV a été étendue en 3D dans le but d'identifier les paramètres constitutifs des composites particulaires. Elle a été subséquemment améliorée en développant la MCVR en ajoutant des contraintes de régularisation. L'évaluation sur des données 3D de déformations bruitées en champ complet a prouvé la supériorité de cette approche. La taille optimale de la région d'intérêt a également été déterminée par une procédure semblable à celle présentée en 2D.

La contribution principale de cette thèse est le développement de méthodes d'identification robustes et efficaces en termes de temps de calcul, qui résultent en des paramètres mécaniques appropriés en 2D et 3D. La thèse a aussi fait la démonstration que l'ajout de techniques de régularisation s'inspirant de modèles d'homogénéisation peut significativement améliorer la précision des solutions.

ABSTRACT

Macroscopic homogeneous testing, such as classical tension and compression tests, can be performed for obtaining the average behavior of a given composite. However, these tests cannot provide the local fiber and matrix properties, nor the matrix-fiber interface adhesion properties. Thanks to recent advances made in optical devices and imaging technologies, several full-field measurement techniques such as Digital Image Correlation (DIC) and Digital Volume Correlation (DVC) have been developed. These techniques allow quantifying 2D or 3D displacement/strain fields over the surface, or even inside an opaque material subjected to external loadings. The experimental availability of such rich information has given rise to several inverse material parameters identification techniques. Among these, the Finite Element Model Updating (FEMU) and the Virtual Fields Method (VFM) have been widely exploited due to their inherent advantages such as their lower sensitivity to noise. The combination of a full-field measurement technique and an inverse identification method is a very promising strategy for simultaneously identifying several local mechanical properties.

The main objective of this thesis was to develop improved inverse identification approaches in 2D and 3D, that were efficient in terms of both accuracy and computational time. The developed approaches were validated by conducting several virtual experiments through local mechanical properties identification of composites with various mechanical and morphological characteristics.

First, an inverse algorithm based on the Finite Element Model Updating (FEMU) technique was developed and improved. The improvement consisted first in using a hybrid optimization technique, i.e. a combination of a global derivative-free algorithm and a gradient-based optimization method, so as to enhance the accuracy of the identified parameters. In addition, a set of mechanically relevant constraints, consisting of an appropriate homogenization model, were included so as to regularize the identification problem. The functionality of this new numerical-analytical approach, named the Regularized Model Updating (RMU), was compared to that of the FEMU method in the presence of noisy measured displacement fields for uni-directional long fiber composites.

Second, a new approach based on the Virtual Fields Method (VFM) was developed with the capability of reconciling accuracy and computational efficiency. The novelty of this Regularized Virtual Fields Method (RVFM) was that mechanically relevant constraints were exploited within an optimization framework to regularize the solution of the related system of equations in the VFM. Application of the RVFM using simulated experiments revealed

that it outperformed the VFM when dealing with noisy measured strain fields. Furthermore, the RVFM led to results of an accuracy similar to that obtained from the RMU, but in a significantly shorter calculation time. Moreover, the optimum size of the region of interest was determined considering a reasonable compromise between DIC magnification requirements and the accuracy of the identified parameters.

Finally, the VFM was extended to 3D with the aim of identifying constitutive parameters of particulate composites. It was subsequently improved by developing RVFM to achieve lower uncertainties in the sought parameters by adding regularization constraints. The evaluation on 3D artificial noisy full-field strain data proved the full potential of the approach. The optimum size of region of interest was also determined through a similar procedure as that used in 2D.

The main contribution of this thesis was to develop robust inverse identification approaches that are computationally efficient, while yielding appropriate constitutive parameters in 2D and 3D. This thesis work also showed that addition of mechanically motivated constraints can significantly improve the robustness of existing approaches

TABLE OF CONTENTS

LIST OF TABLES

LIST OF FIGURES

LIST OF SYMBOLS AND ABBREVIATIONS

$\boldsymbol{A}$	Square matrix created in the Virtual Fields Method
c	Volume fraction of reinforcing phase
$\mathbf{C^0}$	stiffness tensors of matrix
$\mathbf{C^1}$	stiffness tensors of fibers
C_{ijkl}	Stiffness matrix components
$\mathbf{D}$	Strain localization tensor
d_f	Diameter of fibers
E	Isotropic Young's modulus
E_f	Young's modulus of reinforcing fiber
E_l	Out-of-plane effective Young's modulus
E_m	Young's modulus of matrix
E_p	Young's modulus of reinforcing particle
E_t	in-plane effective Young's modulus
F_i	Applied load
f_k	Sequence of correlated random coefficients of signal's Fourier transform
H_κ	Gaussian mask in the Fourier domain with cutoff wavenumber κ
$\mathbf{I}$	Identity matrix
k	Signals frequency
ℓ	Characteristic subset length
L_{opt}	Edge length of optimum size of ROI
M	Number of unknown constitutive parameters
N	Total number of mechanical constraints
N_{RVE}	RVE size
$\mathbf{p}$	Vector of unknown constitutive parameters
$p(\mathbf{p})$	Penalty function
$\mathbf{Q}$	Stiffness matrix for orthotropic material in plane stress condition
Q_{ij}	Stiffness matrix components in plane stress condition
$r(\mathbf{p})$	Residuals of kinematical fields
$\mathbf{S^1}$	Eshelby's tensor
$\boldsymbol{T}$	Traction acting on the boundary of material
$\mathbf{u}$	Vector of displacement field in x direction
$\mathbf{u}^*$	Virtual displacement fields

u_i^*	Virtual displacement fields components
V	Volume of bulk material
$x_n \quad (n = 1, 2, 3)$	Spatial coordinates
$\mathbf{x}$	Spatial coordinate vector
$\nabla\,[\,]$	Gradient operator containing partial derivatives
$\|\mathbf{a}\|_2^2$	ℓ^2-norm for vector $\mathbf{a}$ (also denoted by $\|\,\|^2$)
$\mathbf{A} : \mathbf{B}$	Frobenius inner product of matrices $\mathbf{A}$ and $\mathbf{B}$
$\mathbf{a} \cdot \mathbf{b}$	Dot product of matrices $\mathbf{a}$ and $\mathbf{b}$
$\langle \mathbf{A_{ij}} \rangle$	Spatial average of tensor $\mathbf{A}$ components
∂V	Boundary of bulk material
ΔV_i	Volume associated to the FE model integration points

Greek symbols

α_i	Positive-definite penalty parameters
β_i	Measure of texture roughness
$\tilde{\lambda}$	Predicted effective mechanical property
$\hat{\lambda}$	Experimentally measured effective property
δ	Very small positive-definite value
$\boldsymbol{\varepsilon}$	Elastic strain tensor
ε_{ij}	Elastic strain tensor components
$\boldsymbol{\varepsilon^*}$	Virtual strain tensor
ε_{ij}^*	Virtual strain tensor components
$\mathcal{K}$	Kinematically admissible
ν	Isotropic Poisson's ratio
ν_f	Poisson's ratio of fiber in FRP
ν_{lt}	In-plane effective Poisson's ratio
ν_m	Poisson's ratio of matrix
ν_p	Poisson's ratio of the reinforcing particle
$\boldsymbol{\sigma}$	Stress tensor
σ_{ij}	Stress tensor components
Ω	Domain of feasible set of parameters

Abbreviations

CPS8R	8-node reduced integration elements
DIC	Digital image correlation

DVC	Digital volume correlation
FE	Finite elements
FEMU	Finite element model updating
FFT	Fast Fourier transform
FRP	Fiber-reinforced polymer
GA	Genetic algorithm
HSB	Hashin-Shtrikman Bounds
ISA	Improved spectral approach
KA	Kinematically admissible
LM	Levenberg-Marquardt
MT	Mori-Tanaka
MADS	Mesh adaptive direct search
NOMAD	Nonlinear Optimization with Mesh Adaptive Direct Search
μCT	Micro computed tomography
RMU	Regularized model updating
ROI	Region of interest
RVE	Representative volume element
RVFM	Regularized virtual fields method
SEM	Scanning electron microscopy
SCS	Self-consistent scheme
TOA	Third order approximation
VFM	Virtual fields method

CHAPTER 1

INTRODUCTION

Lighter commercial aircrafts made of composite materials, bio materials used in orthopaedic surgeries and optimization of acoustic absorbing foams are successful examples of innovative materials development. Accurate mechanical properties evaluation is one of the keys to these innovations. Reliable identification strategies to determine constitutive materials parameters are required in many applications such as damage detection in structural health monitoring, accurate prediction of composites strength using micromechanical models and determination of spatial distribution of tissues properties for abnormal tissues detection in medical diagnosis. Direct methods, such as classical tension or compression tests, can be implemented to identify only a limited number of overall mechanical properties from a single test under the assumptions that the materials are homogenous and isotropic. However, such identification approaches are more demanding for adequate characterization of heterogenous and/or non isotropic materials such as composites (Pierron *et al.*, 1998). Moreover, such mechanical tests are not capable of determining *in-situ* local mechanical behavior in heterogenous materials such as the interface between fiber and matrix in a composite, or the modified polymer around a nano-clay reinforcement in nano-composites. Several studies revealed that *in-situ* mechanical properties of composites constituent phases are different from those measured in bulk material as a consequence of manufacturing processes such as consolidation and curing procedure (Gregory et Spearing, 2005; Guicciardi *et al.*, 2008).

A very promising way for simultaneously determining several mechanical parameters of a material is to use an *inverse* strategy along with non-contact full-field measurement techniques (Grediac, 2004). In contrast to the classical tests, where displacement or strain values are measured at the mounting positions of measuring devices, full-field measurement techniques provide these kinematic quantities (displacement/strain fields) over a large region on the specimen. With the improvements in image processing techniques, optical measurement methods, such as Digital Image Correlation (DIC) (Hild et Roux, 2006a) and Digital Volume Correlation (DVC) (Bay, 2008), have become popular techniques, especially in the context of inverse problems. They can provide full-field displacement measurements on the surface or even *inside* opaque materials subjected to external loadings. The availability of such rich information from the whole field of an experiment has given rise to different inverse methods for identification of complex constitutive laws.

Several attempts have already been made to estimate mechanical properties using inverse methods. The earliest and the most widely used inverse identification approach relies on updating finite element models (Lecompte *et al.*, 2007). This so-called Finite Element Model Updating (FEMU) method enables to reconstruct the unknown material parameters from full-field measured displacement or strain data. This mixed numerical-experimental identification technique is a powerful tool for cases where sufficient knowledge of the geometry of specimen and the boundary conditions is available. Although this approach has been successfully applied to identify constitutive parameters of different materials, inaccurate solutions might still be obtained due to the ill-posed nature of the inverse problem. Furthermore, the procedure involves iterative finite element simulations within an optimization framework that can becomes computationally expensive. The Virtual Fields Method (VFM) (Pierron et Grédiac, 2012) is an alternative technique which allows direct (i.e., non-iterative) identification of sought parameters from full-field measured strain data. This procedure eludes the difficulties associated with the geometrical modelling of the specimen and the definition of the boundary conditions. Moreover, when compared to other methods, the VFM is quite insensitive to noise detrimental effects. In the case of composite materials, however, measurement uncertainties as well as high deformation heterogeneity between constitutive phases might influence the efficiency of both characterization methods.

The main propose of this thesis was to develop reliable inverse identification approaches both in terms of their accuracy and their computational time to determine in-situ mechanical parameters of composites constituents. To this end, improved identification algorithms based on FEMU and VFM were developed by adding mechanically relevant regularization constraints in 2D and 3D. The regularization relied on homogenization models predictions, in the sense that solutions providing perfect compromise between the predicted and real effective properties of the composite were considered as identified parameters.

The research work presented in this study covers the following fundamental themes:

- The development and validation of an improved FEMU method based on a parallel hybrid optimization algorithm. The method was applied to noisy measured displacement fields of 2D artificial composites of different mechanical and morphological properties.
- The development and validation of an improved VFM in 2D with the aim of identifying the material parameters at a lower computational cost than the FEMU identification method. The method was validated by applying to noisy measured strain fields of various 2D composites. Moreover, the accuracy and computational performance of the developed approach were compared to those of finite element based methods in the presence of noisy measured data.

– The extension of the developed improved VFM to 3D. The method was validated on noisy strain fields of different 3D artificial composites.

The thesis is organized as follows. Chapter 2 presents background information and a literature review on inverse identification methods and their relevant applications. The objectives of the research project are outlined in Chapter 3 according to the remarks made in Chapter 2, followed by the publication strategy of the scientific articles. The three articles resulting from this work are presented in Chapters 4 to 6. Chapter 4 introduces an improved FEMU approach, according to defined objectives, and its validation using 2D artificial fiber composites. Chapter 5 presents an improved VFM and its application to 2D artificial fiber composites. The performance of the approach is evaluated for different sizes of ROIs, and the optimum size is determined according to the accuracy of resulting parameters. Chapter 6 extends the VFM and improved VFM to 3D and presents its potential applications to particulate composites with different microstructures. Similar study as for 2D is carried out for determining optimum size of ROI in 3D. Chapter 7 discusses the connection between the articles and the reviewed literature. The contributions from this thesis are finally summarized and topics for future studies are recommended in the conclusion.

The following convention has been adopted, unless specified otherwise:

– Lower case letters (such as a, α) denote scalars;
– Boldfaced lower case latin letters (such as $\mathbf{a}$) denote vectors;
– Boldfaced lower case greek letters (such as $\boldsymbol{\alpha}$) denote second order tensors;
– Boldfaced upper case latin letters (such as $\mathbf{A}$) denote fourth order tensors.

CHAPTER 2

LITERATURE REVIEW

2.1 Direct method versus inverse problem

The response of a complex system can be predicted with known input parameters and a reliable model. This kind of problem, which aims at finding the response of the system with respect to input parameters, is referred to as a *direct* problem. In contrast, an *inverse* problem deals with the estimation of a set of parameters based on the system response and a given model. The parameters may define a physical entity directly, e.g. density, voltage, seismic velocity, mass (Asma et Bouazzouni, 2007) or may be coefficients or other constants of a functional relationship that describes the physical system (Aster *et al.*, 2005). Assuming that a physical system is modeled by an adequately understood function $\mathbf{g}$, given a vector of input parameters $\mathbf{p}$ and collected output vector $\mathbf{z}$, a direct problem might be defined in a simplified form as follows:

$$\mathbf{g}(\mathbf{p}) + \boldsymbol{\epsilon} = \mathbf{z} \tag{2.1}$$

where $\boldsymbol{\epsilon}$ is the total error vector (sum of data and modeling errors) of the problem. An inverse problem thus refers to a process of estimating unknown parameters $\mathbf{p}$ given real measured output data for $\mathbf{z}$. Function $\mathbf{g}$ is called an *operator*; It can take forms of a linear or nonlinear system of algebraic equations, ordinary differential equations (ODEs) or partial differential equations (PDEs).

In experimental mechanics, direct methods rely on the implementation of conventional (standardized) experimental techniques so as to determine constitutive parameters of a given material. In such a case, a graphical representation of the relationship between load and displacement (or stress and strain) can be obtained. The resulting data always contain some amounts of unavoidable errors such as those caused by testing setup and measurement devices. Tensile/compressive tests, biaxial tensile tests, 3-point/ 4-point bending tests, pure shear tests, etc. are common examples of direct measurement techniques used in experimental mechanics. In the case of elastostatics, the direct problem is referred to a set of boundary-value partial differential equations (PDEs) for the unknown displacement field (U(x)) assuming that the boundary conditions, geometry, and the mechanical properties are known. Such a problem is schematically depicted in Figure 2.1(a).

Analytical methods have also been developed to determine distribution of properties by taking the advantage of advanced mathematical techniques. This kind of closed form solutions, however, can be used for simple geometries, boundary conditions and under simplifying assumptions on material models (Barbone et Oberai, 2007).
Inverse problems, fall into two broad categories in experimental mechanics: problems associated with identifying unknown constitutive parameters (type 1 (see Figure 2.1(b))), and those related to unknown boundary conditions characterization (type 2 (see Figure 2.1(c))), in which parameters governing the constitutive equations are assumed to be known (Pierron et Grédiac, 2012). Identification of materials properties distribution is classified as an inverse problem of type 1 (Avril *et al.*, 2008a). In this type of problem, given values are a set of observed data, typically the displacement or strain fields ($U(x)$ or $\varepsilon(x)$), boundary conditions and external forces. In this case, one deals with a set of overdetermined displacements and boundary conditions and the unknowns are the mechanical properties represented by the stiffness tensor elements. Therefore, one seeks minimization of the residuals in one of the governing equations. Based on the residuals to be minimized, several inverse identification methods have been developed in the literature.

2.1.1 Challenges in inverse problems

One of the main challenges in inverse methods is the lack of solution uniqueness, which means that several solutions might satisfy the optimality condition provided by the measured data (Ballester et Carter, 2006). Such a situation arises in practice because of noise in the measured data, round-off error in inverse problem calculations, and also because the direct model is not exact. It is essential to specify what solutions have been acquired, which of them are physically plausible and perhaps which of them are stable in various conditions of constraints. So, some essential issues that must be considered include: *solution existence*, *uniqueness* and *instability* (Aster *et al.*, 2005).

Solution existence: In an inverse problem, there might be no admissible sets of parameters that make the model to perfectly match the measured data. This may occur when the mathematical model of the system is approximate (i.e. it does not involve exact boundary conditions, constraints, etc.) or when the measured data are noisy.

Solution uniqueness: Even if an exact solution exists, there is no guarantee that it is unique. It means that irrelevant solutions may satisfy Eq. 2.1. This situation occurs commonly in rank-defficient discrete linear inverse problems and may lead to a significantly smoothed or biased estimated model.

Solution instability: One of the important issues in inverse problems is inconsistency of

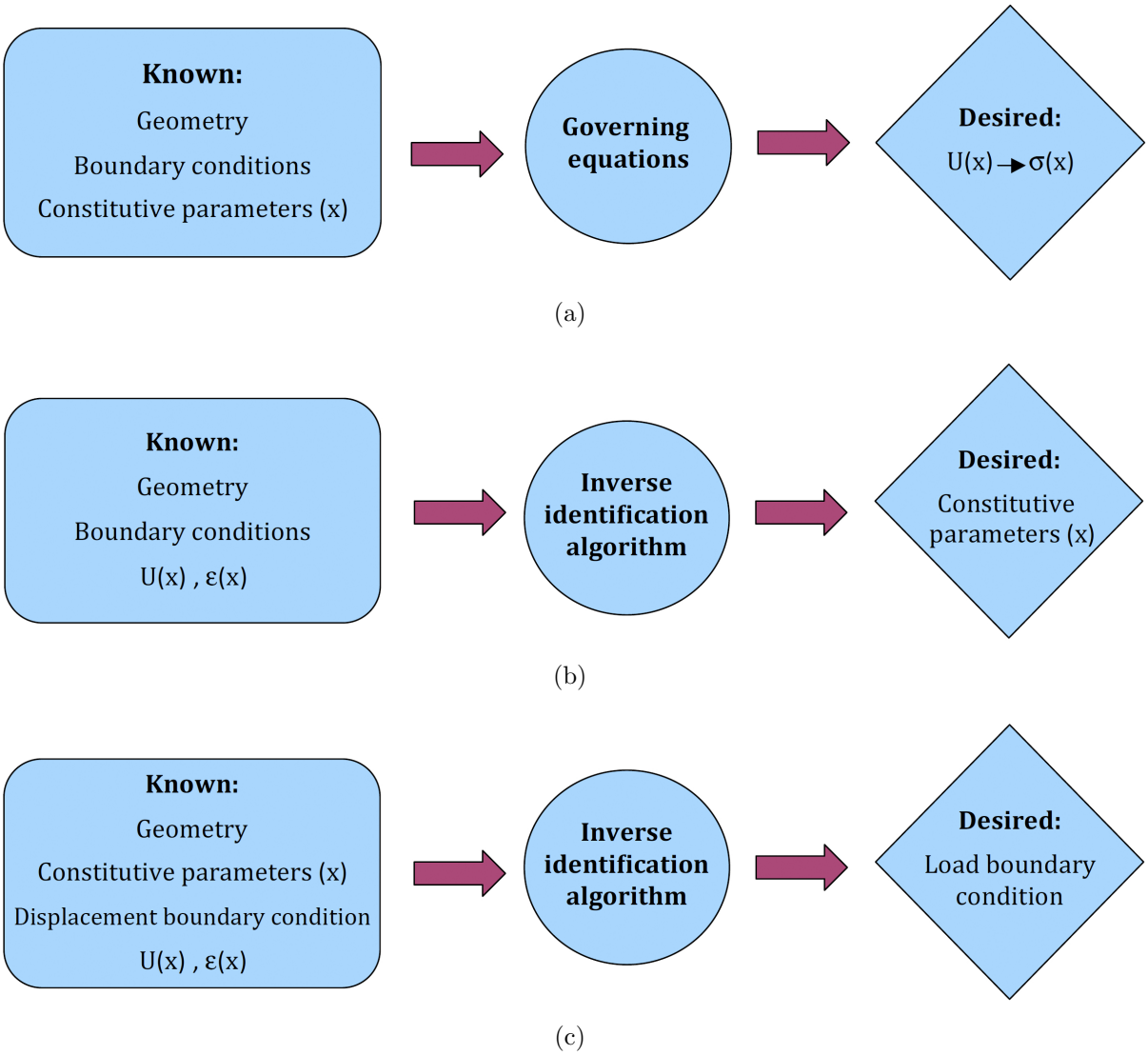

Figure 2.1: Comparison of direct and inverse identification in elasticity; (a) Direct problem, (b) Inverse problem of type 1 , (c) Inverse problem of type 2

the estimated model against trivial changes of measurements. They are respectively referred to as *ill-posedness* and *ill-conditioning* in the case of continuous and discrete inverse problems respectively. The concept of well-posed and ill-posed problems dates from Hadamard's definition in 1902 (Hadamard, 1902) and, accordingly, an inverse problem is considered as ill-posed if the solution is not unique or if the solution is not a continuos function of the data.

Ill-posedness of inverse problems in engineering might arise in practice due to several factors that can generally be divided into three categories: (i) imperfection of the forward problem (mathematical or finite element model) that might stem from different issues such as misuse of mathematical models or inappropriate definition of boundary conditions. Discretization error is a part of modeling error that is created due to the fact that measured data is not continuous and is available only at discrete points. Discretization of the geometry (known as 'meshing' in finite element method) and constitutive relation as a linear combination of basis functions also fall within this category. The influence of the discretization in inverse problems has been investigated in several studies (Kaipio et Somersalo, 2007; Ballester et Carter, 2006); (ii) round-off errors coming from approximations in the numerical analysis, and (iii) inconsistency of the model against trivial variations (perturbations) of measured data due to the presence of noise. Data errors are inherent in experimental setups and measurement algorithms. Despite the important efforts deployed to reduce the influence of this type of errors, either by a careful experimental setup calibration or through analysis of their statistical characteristics (Mosegaard et Sambridge, 2002), they still remain as one of the most important uncertainty sources.

In such cases, when inverse problem is ill-posed, additional information, such as mathematical or physical constraints, must be applied to stabilize the inversion process. Such a procedure is called *regularization* and can be imposed to avoid undesired oscillating behavior of the solution. This important issue will be discussed further in the sequel.

2.2 Governing equations in linear elasticity

Consider the deformable solid illustrated in Figure 2.2(a) subjected to a combination of external tractions (T_1 and T_2) and supported on a part of its external surface. The fundamental governing equation to be solved in linear elasticity (Bonnet et Constantinescu, 2005) under the static conditions reduces to the equilibrium equations, which in the absence of body forces (e.g. negligible weight) and for a small material element, reads:

$$\mathrm{div}\boldsymbol{\sigma}(\mathbf{x}) = \sum_{j=1,2,3} \frac{\partial \sigma_{ij}(x)}{\partial x_j} = 0 \text{ (for } i = 1, 2, 3) \tag{2.2}$$

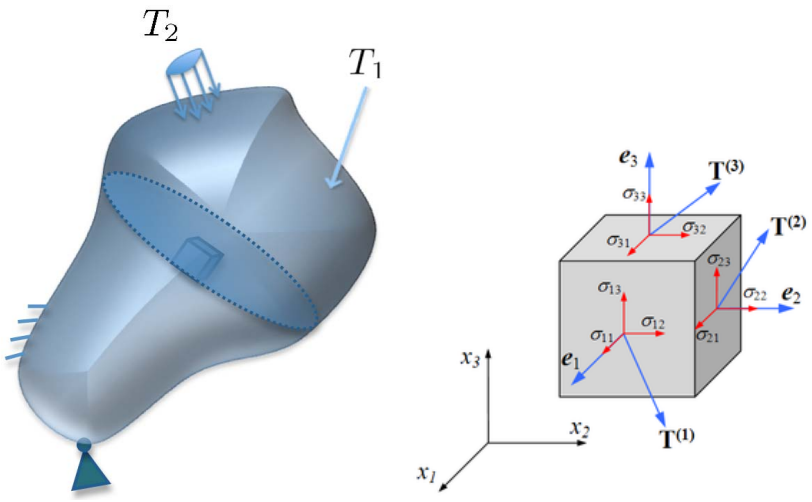

(a) (b)

Figure 2.2: (a) Deformable solid of any shape subjected to mechanical loading (tractions). (b) Stress components on a typical element of a deformable solid (Sanpaz, 2008)

where $\boldsymbol{\sigma} = \{\sigma_{ij}\}$ is the second-order stress tensor and $\mathbf{x} = (x_1, x_2, x_3)^T$ is the position vector of a material point. Figure 2.2(b) depicts spatial components of the stress tensor for a deformable body. Strains are defined as:

$$\boldsymbol{\varepsilon}(\mathbf{x}) = \frac{1}{2}(\nabla \mathbf{u}(\mathbf{x}) + \nabla \mathbf{u}^T(\mathbf{x})) \tag{2.3}$$

where $\mathbf{u}$ is the displacement vector. Finally, the constitutive equation, namely Hooke's law, links the state of the stress and deformation for a linearly elastic material as:

$$\sigma_{ij} = C_{ijkl}\, \varepsilon_{kl} \tag{2.4}$$

where C_{ijkl} is the symmetric fourth-order *local* elasticity (or stiffness) tensor having between 2 and 21 independent coefficient, depending on the material symmetry. For the particular case of an isotropic material in a plane state of stress, the matrix form of the stress-strain relationship reduces to (with the usual definition of simplified indices for stress and strain: $11 \rightarrow 1$, $22 \rightarrow 2$, $12 \rightarrow 6$):

$$\begin{Bmatrix} \sigma_1 \\ \sigma_2 \\ \sigma_6 \end{Bmatrix} = \begin{bmatrix} Q_{11} & Q_{12} & 0 \\ Q_{21} & Q_{22} & 0 \\ 0 & 0 & Q_{66} \end{bmatrix} \begin{Bmatrix} \varepsilon_1 \\ \varepsilon_2 \\ \varepsilon_6 \end{Bmatrix} \tag{2.5}$$

or

$$\boldsymbol{\sigma} = \mathbf{Q}\,\boldsymbol{\varepsilon} \tag{2.6}$$

where $\mathbf{Q}$ is the in-plane stiffness matrix and its components are defined as follows

$$\begin{cases} Q_{11} = Q_{22} = \dfrac{E}{(1-\nu^2)} \\ Q_{12} = Q_{21} = \dfrac{\nu E}{(1-\nu^2)} \\ Q_{66} = \dfrac{Q_{11} - Q_{12}}{2} \end{cases} \tag{2.7}$$

The strain energy stored in a linearly elastic material after loading can also be obtained by integrating the strain energy density over the volume (V):

$$\begin{aligned} W &= \frac{1}{2}\int_V \sigma_{ij}\varepsilon_{ij}\,\mathrm{d}V \\ &= \frac{1}{2}\int_V C_{ijkl}\,\varepsilon_{kl}\,\varepsilon_{ij}\,\mathrm{d}V \end{aligned} \tag{2.8}$$

2.3 Full-field measurement techniques

The need for integrating experimental information with analytical or numerical models in inverse problems has given rise to the development of different non-contact full-field measurement techniques. Recent advances in computer vision and 2D/3D imaging systems, triggered the development of optical methods such as moiré interferometry (Han *et al.*, 2001), Electronic Speckle Pattern Interferometry (ESPI) (Schajer et Steinzig, 2005), speckle photography (Joenathan, 1997) and Digital Image Correlation (DIC) in 2D and 3D (Mortazavi *et al.*, 2013b, 2014; Hild et Roux, 2006a; Bay, 2008). These techniques enable measuring physical quantities such as displacements and strains for a large number of discrete points at the surface or even inside a specimen. Among the mentioned methods, the DIC is one of the most popular methods thanks to its simplicity and straightforwardness.

The main advantage of these measuring techniques is that they can provide the required heterogenous kinematic fields with a single test and without inducing damage to the material. This consequently saves time and expenses for sample preparation. Unlike point-wise measurement techniques done by strain gauges and displacement transducers, full-field mea-

surement techniques enable capturing local phenomena such as damage and stress concentration and also inclusions localization. Such a rich information is the key for determining in-situ mechanical properties such as the fiber-matrix interface strength in composites, the modified polymer properties in a nano-clay nanocomposite, etc. By providing heterogenous full-field measured data using a single undetermined setup, several unknown parameters can be simultaneously identified. This is because heterogeneous strain fields are affected by a greater number of constitutive parameters than homogenous one. Finally, using full-field measurement techniques, specimens with any complex geometry can be used in an in-situ mechanical testing without needing for manufacturing standard coupons. An investigation on the advantages of full-field measurement techniques and their applications to composite materials has been presented by Grédiac in (Grediac, 2004).

Several inverse identification methods based on full-field measured data have been reported in the literature for identifying mechanical constants of different constitutive models, e.g. elastic, viscoelastic, hyperelastic or even plastic models (Avril *et al.*, 2008a; Avril et Pierron, 2007). The following sub-sections introduce existing inverse identifcation methods, especially the most commonly used methods, namely Finite Element Model Updating (FEMU) and the Virtual Fields Method (VFM).

2.4 Material parameter identification methods based on full-field measurements

2.4.1 Finite Element Model Updating method (FEMU)

Thanks to progresses in computers capabilities in terms of both hardware and software, the finite element method has become one of the most powerful numerical tools to solve solid mechanics problems. This kind of analysis is refered to as *forward* or *direct analysis* and can be used to solve the inverse problem of type 1 (Figure 2.1(b)). In the FEMU method (also known as *Displacement Gap Method*) (Springmann et Kuna, 2003; Zhou *et al.*, 2006; Kim et Park, 2004), material parameters input into the finite element model are iteratively updated based on the comparison of the corresponding output data after forward analysis (typically displacement or strain fields) and their experimental counterparts. The objective is to identify the set of parameters that provide the best match between numerical outputs and real behavior, captured through experiments. To this end, optimization techniques are exploited so as to minimize the discrepancy between numerically (FE) predicted and experimentally measured displacement/strain fields with respect to the mechanical parameters in

a least square objective function such as:

$$r(\mathbf{p}) = \|\hat{\mathbf{u}} - \mathbf{u}(\mathbf{p})\|_W^2 = \Big(\hat{\mathbf{u}} - \mathbf{u}(\mathbf{p})\Big)^T \cdot W \cdot \Big(\hat{\mathbf{u}} - \mathbf{u}(\mathbf{p})\Big) \tag{2.9}$$

where $\hat{\mathbf{u}}$ is the measured displacement field, $\mathbf{u}$ is the displacement field calculated with the FE model and W is a symmetric positive definite weight matrix. The vector of model parameters $\mathbf{p}$ is then updated at each iteration until convergence is achieved. Figure 2.3 illustrates the relevant algorithm based on a gradient-based optimization technique.

The accuracy of the identified parameters depends strongly on the level of uncertainty in the experimentally measured data used in the optimization procedure. The most significant drawback of the approach is the need for an iterative computational process for adjusting the sought parameters. This can become prohibitive when dealing with the identification problems consisting of 3D finite element models. Another drawback is associated with the convergence of the algorithm, which is mainly affected by some well-known factors such as type of optimization technique, material model, boundary conditions and sensitivity of the algorithm to noisy measured data. Unlike conventional mechanical tests performed under the assumption of material homogeneity, the FEMU can be applied to determine the distribution of properties in materials with heterogeneous stress/strain fields. One of the advantages of the method is the fact that it does not require full-field measurements on the whole domain, and therefore, parameter identification can be carried out using partial knowledge on the displacement data (Genovese *et al.*, 2004). Indeed, inverse solutions within smaller region of interests are normally preferred as these would be more stable and give rise to less discretization error. Furthermore, material models with complex geometries and boundary conditions can be characterized taking the advantages of finite element simulation capabilities. Owing to its flexibility, the FEMU technique has been exploited in different scientific branches such as structural dynamics (Friswell et Mottershead, 1995; Asma et Bouazzouni, 2005) and medical applications (Van Ratingen, 1994) over the last decades, and is still being utilized to determine mechanical constants of materials(Nair *et al.*, 2007). Since there is no restriction on the type of constitutive equation, a wide range of material behavior, from linear isotropic elasticity to hyper-visco-elasticity can be characterized. In linear elasticity for example, Genovese et. al. (Genovese *et al.*, 2006) identified elastic constants of transversely isotropic materials based on Phase Shifting ESPI measurements. Cardenas-Garcia et. al. (Cárdenas-García et Preidikman, 2006) determined elastic properties of a synthetic polymer plate loaded under plane stress conditions using displacement fields derived from the moiré interferometry method. Lecompte et al. (Lecompte *et al.*, 2005, 2007; Ramault *et al.*, 2009) reconstructed

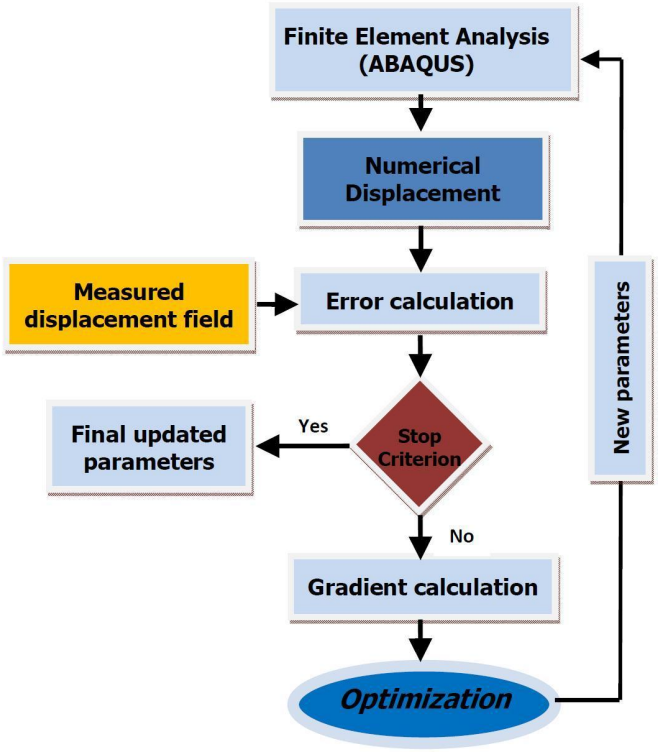

Figure 2.3: Finite Element Model Updating algorithm

the four in-plane elastic parameters of an orthotropic composite subjected to a biaxial load. However, instead of minimizing the misfit between the displacements, they used strains as output data. Identification of in-plane elastic properties of an eight-ply woven composite laminate based on Simulated Annealing (SA) optimization technique was also investigated in (Genovese *et al.*, 2005). Other studies have also been carried out for characterizing the anisotropy behavior of materials (Molimard *et al.*, 2005; Silva *et al.*, 2009). Several attempts have also been made to characterize materials consisting of inelastic constitutive laws. The mixed numerical-experimental inverse method as proposed by Magorou et. al. (Le Magorou *et al.*, 2002) focused on genetic optimization and optical metrology, with the aim of identifying viscoelastic parameters of wood-based panels. Meuwissen et al. (Meuwissen *et al.*, 1998) obtained isotropic von Mises and orthotropic Hill yield criterion in an elasto-plastic constitutive model of aluminum plates. Displacements of retro-reflective markers on the surface of plates were measured optically in a uniaxial tensile test and compared with those of finite element analysis in a Gauss-Newton optimization framework. Identification of constitutive parameters of linear plasticity and parabolic hardening models for materials subjected to large deformation was investigated in (Kajberg et Lindkvist, 2004). A comprehensive review

of FEMU techniques in statics can be found in (Ienny *et al.*, 2009).

Mechanical behavior of composite materials, such as strength and toughness, depend strongly on the mechanical characteristics of the constituent phases, particularly at the matrix/reinforcement interface (Achenbach et Zhu, 1989). The importance of this issue has given rise to the development of several in-situ local mechanical parameter identification algorithms. An inverse/genetic method for interfacial parameter identification has been proposed by Kang et al (Kang *et al.*, 2004). Tensile and shear mechanical properties at the interface region in a planar metal matrix composite were identified based on failure information at this region using a Genetic Algorithm (GA) optimization method. Wang et al (Wang *et al.*, 2010) developed an inverse technique to identify viscoelastic adhesive interfacial parameters relying on damage state at the interface. Deformation images were recorded at the surface of the specimen in order to record failure positions of interfacial area. Fedele et al. (Fedele *et al.*, 2009) proposed an inverse strategy to estimate mechanical parameters of a cohesive law of an adhesive layer using full-field displacement data provided by DIC. Maranon et al. (Maranon *et al.*, 2003) developed a methodology to characterize the magnitude and location of delamitation in composite laminates making use of central moments obtained from finite element model and full-field ESPI displacements. It is interesting to note that other studies have been conducted for identifying local loss of tensile and compressive stiffnesses in impacted composite laminates using digital image correlation (DIC) and finite element (FE) model updating (Sztefek et Olsson, 2008, 2009). Other important research efforts have also dealt with the determination of damage constitutive laws for fiber reinforced composites (Geers *et al.*, 1999a) and woven fabric composites (Anghileri *et al.*, 2005a).
In a different strategy, namely the least square method (Ghouati et Gelin, 2001; Jadamba *et al.*, 2008), the *average* response of material (e.g. displacement data) obtained either using finite element method or solving the relevant PDEs is compared with experimental data. The practical advantages of this method is that it requires neither imaging setup nor full-field kinematic quantities measurements and their derivatives calculation.

The concept in all of the above-mentioned works has been to minimize an objective function such as Eq. 2.9. The developed algorithms, however, can not ensure the reliability of the obtained parameters owing to the inevitable ill-posed nature of such inverse problems. Ill-posdness is mainly caused because of inevitable noise in the image and systematic errors associated with full-field measurement algorithms. The former is typically caused by experimental setup imperfection and image acquisition noise and the latter is rather related to correlation criterion, sub-pixel algorithm, subset size, etc. For stabilizing the optimization process, additional constraint can be added as a regularization scheme to the objective

function such that:

$$p(\mathbf{p}) = \|\hat{\mathbf{u}} - \mathbf{u}(\mathbf{p})\|_W^2 + \alpha\|\boldsymbol{\epsilon}(\mathbf{p})\|^2 \tag{2.10}$$

where $\boldsymbol{\epsilon}(\mathbf{p})$, often having a physical meaning, is another residue to be simultaneously minimized. α is called the regularizing parameter defining the contribution of the added constraint to the objective function(Aster *et al.*, 2005). Indeed, this regularization term restricts admissible solution space of the given inverse problem by a priori information of the system. Several regularization strategies have been employed by other researchers. For instance, Oberai et al.(Oberai *et al.*, 2004) used a regularization technique, known as Tikhonov regularization (Aster *et al.*, 2005), that penalized large variations in the spatial gradients of the shear modulus parameter. Genovese et al. (Genovese *et al.*, 2004) set a number of upper and lower a priori known bounds on the unknown orthotropic parameters to ensure stability of the optimization, thus solving a constrained optimization problem. As for the weight matrix, Gokhale et al. (Gokhale *et al.*, 2008) chose a weight matrix so that all the measurements contributed equally to the objective function. Without smoothing the displacement residues, the objective function would be more sensitive to a point with a large measured deformation and the model updating would be biased in favor of minimizing that particular error. Other regularization strategies relying on constitutive relation error (Florentin et Lubineau, 2010) and global variance analysis (Lubineau, 2009) have also been studied.
It should also be mentioned that there are other model updating approaches in which the forward problem might have a closed-form solution (Hild et Roux, 2006b) or be performed through alternative numerical methods such as boundary element method (Lee *et al.*, 2000).

2.4.2 Virtual Fields Method (VFM)

As its name implies, the Virtual Fields Method (VFM) (Pierron et Grédiac, 2012) relies on the virtual work principle to determine unknown constitutive parameters. The method was first proposed by Grédiac (Grédiac, 1989) and has been successfully applied to various mechanical characterization problems (Grédiac *et al.*, 1998; Pierron *et al.*, 2000a; Grédiac et Pierron, 2006). The VFM has been theoretically proven to be very similar to the FEMU approach, in the sense that the former provides maximum likelihood solutions and the latter is developed based on displacement gap minimization (Avril et Pierron, 2007). One limitation of the VFM is the need for full-field strain measurements typically obtained from displacement fields differentiation, which might amplify uncertainties in the measurements. Despite this drawback, the VFM has been demonstrated to be more efficient than the other identification methods in terms of both decreasing the computational efforts and reducing the ill-posedness

inherent in the technique (Avril et Pierron, 2007). This method is basically developed through writing the global equilibrium of a body subjected to a given load with the principle of virtual work. In general, the relevant equation is written with the virtual works done by the applied loads on different portions of body as:

$$-\int_V \boldsymbol{\sigma} : \boldsymbol{\varepsilon}[\mathbf{u}^*]\, dV + \int_S \boldsymbol{T} \cdot \mathbf{u}^*\, dS + \int_V \mathbf{f} \cdot \mathbf{u}^*\, dV = \int_V \rho \mathbf{a} \cdot \mathbf{u}^*\, dV \tag{2.11}$$

where $\boldsymbol{\sigma}$ is the stress field, $\boldsymbol{\varepsilon}[\mathbf{u}^*]$ is the virtual strain field obtained by differentiating the virtual displacement field $\mathbf{u}^*$, V is the volume of the solid, $\boldsymbol{T}$ is the external loading acting on surface S, $\mathbf{f}$ is the external body force per unit volume, ρ is the density of material and $\mathbf{a}$ is acceleration. The integrals on the left hand side of Eq. 2.11 represent the virtual work done by internal and external forces and that on the right hand side is associated to the inertial effect caused by the acceleration. The above fundamental equation can be adapted to the type of mechanical problem and constitutive relation of material, which yield to two divisions of the approach, namely linear or nonlinear VFM (Pierron et Grédiac, 2012). Suppose that the deformation field is known over V and the objective is to find the parameters of a constitutive law that has already been fixed. If it is also assumed that the applied load is quasi-static, $\mathbf{a}$ is negligible. For a plane stress condition and in the absence of body forces, substitution of Eq. 2.4 into Eq. 2.11 leads to

$$\int_V \mathbf{C} : \boldsymbol{\varepsilon}[\hat{\mathbf{u}}] : \boldsymbol{\varepsilon}[\mathbf{u}^*]\, dV = \int_S \boldsymbol{T} \cdot \mathbf{u}^*\, dS \tag{2.12}$$

where $\boldsymbol{\varepsilon}[\hat{\mathbf{u}}]$ denotes the strain tensor calculated from the measured displacements $\hat{\mathbf{u}}$. The idea in the VFM is to expand Eq. 2.12 using as many independent virtual displacement fields as unknown parameters, thus building up a system of linearly independent equations consisting of unknown parameters. For a linearly elastic material, this leads to a linear system of equations ($\boldsymbol{A} \cdot \mathbf{q} = \mathbf{b}$) through which the unknown parameters can be directly obtained.

The virtual displacement field functions may be chosen among an infinite number of possibilities and the choice of an appropriate set of test functions is one of the key-factors in this method. The test functions must satisfy some particular conditions: they must be differentiable, have C^0 continuity and be Kinematically Admissible (KA), i.e. they must satisfy the actual displacement boundary conditions. The main difficulty, however, is associated to the strategy for finding sufficiently independent virtual fields, an important aspect that defines the sensitivity of the VFM to noise (Avril *et al.*, 2004). The stability of the technique against

measurements noise increases with a sensible choice of virtual fields. As a mater of fact, a greater independence of virtual fields is proportional to a lower sensitivity of the linear system to noisy data and therefore to more reliable solutions. It has been shown that, by rendering matrix $\boldsymbol{A}$ equal to the identity matrix, a suitable set of virtual fields, so-called special virtual fields (Grédiac *et al.*, 2002a,c), can be attained automatically so that independence of relative equations is ensured. Unlike intuitive choice of virtual fields, special selection requires parameterization of virtual fields for which the unknown coefficients are determined by imposing suitable constraints compatible with the applied boundary conditions. The idea behind the optimal choice of virtual fields was also proposed by Avril et al (Avril *et al.*, 2004) to tackle the VFM ill-posedeness by decreasing its sensitivity to noise. The method requires an optimization process coupled with identification of optimal geometrical and testing configuration suited for a given material (Avril *et al.*, 2004). Moreover, a methodology based on piecewise virtual fields was proposed (Toussaint *et al.*, 2006) for detecting heterogeneities in functionally graded materials and determining local mechanical properties.

Since its development in 1989, the VFM has been mainly dedicated to solve the inverse problem of type 1 (i.e. material parameters identification). It was first exploited to determine linear elastic material parameters (Grédiac, 1989). To date, this methodology has been successfully applied to diverse identification problems from plane stress problems in elasticity (Grédiac *et al.*, 2003, 2002c) and plasticity (Avril *et al.*, 2008c) to viscoelastic constants estimation (Giraudeau *et al.*, 2006). The application of the approach to hyper-elastic materials has also been reported (Promma *et al.*, 2009). Several studies have also been carried out reporting its application on composite materials. Identification of bending (Grédiac, 1996; Grédiac *et al.*, 2003) and in-plane (Grédiac *et al.*, 2002a; Pierron *et al.*, 2007) properties of composites are some examples. Through-thickness characterization of thick or laminated composites, either with a linearly elastic or a nonlinear behavior, has also been studied (Pierron et Grédiac, 2000; Moulart *et al.*, 2006). Other studies, such as those conducted by Chalal et al. (Chalal *et al.*, 2004) and Kim et al. (Kim *et al.*, 2007), dealt with the determination of damage parameters in composites. Furthermore, in the case of 3D problems, the VFM has been applied to elastography applications in order to retrieve heterogenous stiffness distribution from 3D full field measurements (Avril *et al.*, 2008b). Finally, it is worth stating that the VFM has been recently exploited to find solutions for the inverse problems of type 2 (i.e. identification of load/boundary conditions) (Moulart *et al.*, 2011).

2.4.3 Constitutive Equation Gap Method (CEGM)

This method was initially applied for error estimation in the finite element method and then used for the identification of elastic properties (Geymonat et Pagano, 2003). The method aims at minimizing the error in the constitutive Eq. 2.4 through a criterion similar to the following functional:

$$\mathcal{E}(\mathbf{C}, \boldsymbol{\sigma}, \hat{\mathbf{u}}) = \frac{1}{2} \int_{\Omega} (\boldsymbol{\sigma} - \mathbf{C} : \boldsymbol{\varepsilon}[\hat{\mathbf{u}}]) : \mathbf{C}^{-1} : (\boldsymbol{\sigma} - \mathbf{C} : \boldsymbol{\varepsilon}[\hat{\mathbf{u}}])\, dV \tag{2.13}$$

where $\mathbf{C}^{-1}$ is the compliance tensor, which confers the physical dimension of energy to $\mathcal{E}(\mathbf{C}, \boldsymbol{\sigma}, \hat{\mathbf{u}})$. The above error-functional is smoothened by the weight tensor $\mathbf{C}^{-1}$. The CEGM could be interpreted as minimizing the discrepancy between a given stress field $\boldsymbol{\sigma}$ and another stress field resulting from the product of an unknown constitutive matrix and the measured strain data. In fact, the CEGM functional 2.13 is another form of minimizing the sum of strain and stress energy potentials (Bonnet et Constantinescu, 2005). The method does not require necessarily the full-field measured data for its solution, but it incorporates available full-field data to increase the reliability of the acquired results. To identify the elasticity tensor $\boldsymbol{C}$ for instance, based on the experimental availability of displacements and stresses, one can have the following minimization problem:

$$\mathbf{C} = \min \mathbf{Y}(\mathbf{C}^*) \tag{2.14a}$$

$$\mathbf{Y}(\mathbf{C}^*) = \min\, \mathcal{E}(\mathbf{C}^*, \boldsymbol{\sigma}, \hat{\mathbf{u}}) \tag{2.14b}$$

where $\mathbf{C}^*$ is the set of admissible elasticity tensor. A new variant of CEGM has been recently proposed by Lubineau et. al (Florentin et Lubineau, 2010) in which optimized admissible stress fields are constructed in order to minimize experimental observation variance and therefore regularize the problem.

2.4.4 Equilibrium Gap method (EGM)

The Equilibrium Gap method (EGM) consists of identifying the parameters that minimize the residuals in the internal equilibrium equation in a bulk material (Claire *et al.*, 2002). The method aims at minimizing the nodal force residuals obtained from measured displacements and those calculated theoretically. The weak form of the equilibrium equation can be approximated using Finite Element discretization by expressing the displacement field in terms of nodal displacements interpolated by some shape functions. The resulting relation

takes the following form:

$$\mathbf{K}(\mathbf{p})\mathbf{u} = \mathbf{f} \tag{2.15}$$

where $\mathbf{K}(\mathbf{p})$ is the stiffness matrix being a function of known shape functions and unknown elasticity parameters $\mathbf{p}$, and $\mathbf{u}$ and $\mathbf{f}$ are the nodal displacement values and the external force vectors, respectively. Hence, the EGM problem can be solved by minimization of the following residual

$$\mathbf{f_{res}} = \|\mathbf{K}(\mathbf{p})\hat{\mathbf{u}} - \hat{\mathbf{f}}\|^2 \tag{2.16}$$

where $\hat{\mathbf{u}}$ is the measured displacement field. A regular FE mesh must be provided such that its nodes are coincident with measurements grid points. The method is a direct identification approach, very similar to piecewise version of VFM, and does not require to update full-field displacement data iteratively. The EGM has been mostly used to retrieve the spatial distribution of elastic parameters within a domain (Avril *et al.*, 2008a). This can be employed to identify the local reduction of the properties or isotropic damage of materials. For example, Claire et al. (Claire *et al.*, 2002) utilized the EGM to identify the isotropic damage parameter of a homogeneous material.

2.4.5 Reciprocity Gap method (RGM)

The Reciprocity Gap method (RGM) method (Bonnet et Constantinescu, 2005) can be considered as a combination of the VFM and the Maxwell-Betti reciprocal theorem (Salençon, 2001). According to the Maxwell-Betti theorem, the work done by one load on the displacement due to a second load is equal to the work done by the second load on the displacement due to the first. To define a reciprocity gap, consider two elastic bodies occupying the same region and characterized by two distinct distributions of elasticity tensors $\mathbf{C}$ and $\mathbf{C}^*$ and two displacement fields $\hat{\mathbf{u}}$ and $\mathbf{u}^*$ induced by traction distributions $\hat{\boldsymbol{T}}$ and $\boldsymbol{T^*}$ respectively. The auxiliary state ($\mathbf{u}^*$,$\boldsymbol{T^*}$) is referred to as virtual or adjont state. Applying virtual work principle in turn to the experimental ($\hat{\mathbf{u}}$, $\hat{\boldsymbol{T}}$) and to the adjoint states, application of the reciprocity theorem leads to:

$$\int_S (\hat{\boldsymbol{T}} \cdot \mathbf{u}^* - \boldsymbol{T^*} \cdot \hat{\mathbf{u}})\, dS = \int_\Omega \boldsymbol{\varepsilon}[\mathbf{u}^*] : (\mathbf{C}^* - \mathbf{C}) : \boldsymbol{\varepsilon}[\hat{\mathbf{u}}]\, dV = R(\mathbf{C}^* - \mathbf{C}, \mathbf{u}^*, \hat{\mathbf{u}}) \tag{2.17}$$

which defines the reciprocity gap $R(\mathbf{C}^* - \mathbf{C}, \mathbf{u}^*, \hat{\mathbf{u}})$. For any virtual field $\boldsymbol{u}^*$ the left-hand side of equation (1.22) is a known function of experimental data, while the right-hand side depends on unknown elasticity tensor $\mathbf{C}^*$. Based on reciprocity theorem assumption, *reci-*

procity gap can appear if the elasticity tensor of two states are not identical. Hence, if $\mathbf{C}^*$ differs from $\mathbf{C}$ by a small perturbation, i.e. $\mathbf{C}^* = \mathbf{C} + \delta\mathbf{C}$, a linearized form of Eq. 2.17 will be attained, in which the unknown elastic tensor can be retrieved by minimizing the reciprocity gap equation in an inverse problem.

2.5 Summary and comparison of the methods

All of the above mentioned identification techniques benefit from using a large number of experimental data obtained from full-field measurements. The FEMU and CEGM approaches do not necessarily require full-field measurements. The FEMU is the most widespread method, among all aforementioned identification techniques, because of some special features. This method does not require full-field measurement data on the whole domain, and consequently, the computation time can be shortened in the identification process. Moreover, this technique profits from the robustness of the finite element method when specimens with complex geometries and boundary conditions are to be characterized. The main drawback, however, is that the method is computationally expensive because of time-consuming finite element calculations, specially when dealing with 3D models. In contrast, the EGM and the VFM require full-field data within the domain. These two approaches provide direct solutions to the inverse problems since no minimization of residuals is required. The fact that these methods are not iterative, however, immediately brings a limitation: they do not follow any regularization condition. Significant improvements have been made in the VFM during recent years. Strategies that enable optimal choice of virtual fields resulted in increased stability of the matrix inversion, and therefore, its decreased sensitivity to noise. The sensitivity level to different sources of uncertainties in the measurements is the most prominent criterion that can describe the robustness of an identification method. In linear elasticity, both FEMU method and the VFM have been demonstrated to be powerful tools owing to their lower sensitivity to noise than other identification methods (Avril et Pierron, 2007). Relying on the error assessment from a set of noisy data, it was proven that parameters uncertainties resulting from the VFM and FEMU approaches were lower than from other techniques.

2.6 Optimization methods

Numerous optimization techniques have been exploited for solving inverse problems. They can be divided into three main groups: derivative-free optimization (such as evolutionary algorithms and direct search algorithms), gradient-based optimization and hybrid optimization

methods, which benefit from both derivative-free and gradient-based algorithms advantages.

2.6.1 Derivative-free optimization methods

Evolutionary algorithms

Evolutionary algorithms (Kang *et al.*, 2004; Nair *et al.*, 2007), such as Genetic Algorithms (GA), are developed based on genetic definitions and use iterative progress to minimize an objective function and improve initial solutions. In GA, each optimization parameter is represented as a 'chromosome' (individual). The optimization process is initialized by randomly producing a 'population' of m individuals. The objective function is computed for all individuals. Individuals are then sorted according to their objective function values (fitness values), such that individuals with lower fitness values are placed on top (as the algorithm aims at minimizing objective function value). The GA then uses evolutionary mechanism, such as growth or development (crossover and mutation) in the population to improve it and make a new generation. Highest-scoring individuals (elites) pass to the next generation with no change. This generational process is repeated until a termination condition has been reached.

Usually, a larger population size implies more objective function evaluations and a better final solution. However, for parameter identification problems consisting of time consuming blackbox evaluations, a larger population size leads to longer computational time. On the other hand, a small population may lead to premature convergence and a suboptimal solution. The higher the value of crossover rate is, the faster the optimal solution can be achieved. But very high value of this parameter may lead to premature convergence. Too large values of mutation rate may also result in a purely random search algorithm. Conversely, if this parameter is too small, it may cause premature convergence and result in suboptimal solution. Different combinations of mentioned GA variables result in various solutions. The optimal values of GA parameters must be found by numerical experimentation based on algorithm performance comparison. The performance of genetic/inverse identification procedures does not depend on the initial solution. The classical GAs, however, lack local search ability and are computationally expensive for time-consuming blackbox optimizations.

Parallel Genetic Algorithms (PGA) (van Soest et Casius, 2003) are used to speed up the procedure of GA and to enhance their performance. There are two kinds of PGA that are more commonly used in practice: global and coarse-grain methods (Nan *et al.*, 2010). The global PGA holds only one population, in which individuals are distributed into different cores in order to speed up the evaluation of the objective function. Each individual then

performs crossover and mutation operations and a global selection operation is done over the whole population. In the coarse-grain PGA, however, the population is divided into several sub-populations and each holds a serial GA independently. Also, in addition to some basic genetic operators (crossover and mutation), elitist migration is introduced in the coarse-grain PGA. This additional mechanism is associated with the elitists exchanging between different subpopulations and hence shows an increased performance in comparison with the global PGA.

It worth mentioning also that evolutionary algorithms belong to heuristic optimization methods with global convergence properties.

Direct search algorithms

These algorithms do not require the approximation of objective function gradient and rely only on objective function values during iterations. Owing to their simplicity, flexibility and reliability, these algorithms still remain popular. Direct search methods were developed based on sequential examination of trial solutions generated by a certain strategy (Hooke et Jeeves, 1961). One of the commonly exploited nonlinear direct search algorithm is the Nelder-Mead simplex algorithm (Nelder et Mead, 1965) in which the objective function evaluation is performed on a set of points that form a simplex. In each iteration, the worst corner point is identified and is subsequently replaced by introducing a new vertex such that a new simplex is created. The process of replacing the worst point is performed through a number of operations about the centroid of simplex: reflection, expansion, inside and outside contractions. It should be mentioned that convergence of the original Nelder-Mead method is not guaranteed.

An alternative is the Generalized Pattern Search (GPS) algorithm proposed by Torczon (Torczon, 1997) for unconstrained optimization. The algorithm was further expanded to bound constraint optimization and more generally to problems with linear constraints by Lewis and Torczon (Lewis et Torczon, 1999, 2000). This method includes two phases. In the first phase, named Search phase, the objective function value is calculated over a finite number of undefined mesh points. At each iteration, the Search phase attempts to find a new mesh point whose objective function value is lower than the best current solution. The algorithm replaces the best point and starts searching consecutively until it fails in providing an improved mesh point. At this step, the algorithm calls the Poll procedure consisting of objective function evaluation at neighboring mesh points to check if a lower function value can be found. The polling area in the GPS, however, is restricted to a finite set of undefined directions. This drawback has been solved by the Mesh Adaptive Direct Search (MADS)

method (Le Digabel, 2011; Audet et Dennis Jr., 2006; Abramson *et al.*, 2011). The concepts for the Search phase in the MADS method is the same as that of the GPS method, while the Polling procedure is quite different. The key advantage of MADS over GPS is that it performs local exploration of variable space by using an asymptotically dense set of polling directions. MADS is a frame-based local optimization algorithm for nonlinear problems. It can deal with a wide range of nonsmooth objective functions under nonsmooth constraints without having any derivative information. Another attribute of MADS is that infeasible trial points are constrained and discarded with respect to the applied constraints (based on extreme barrier approach) during optimization. Moreover, this optimization method can be executed in parallel mode on multiprocessor machines (Le Digabel *et al.*, 2010). Both attributes are very advantageous for time-consuming blackbox optimizations.

Studies have been carried out which demonstrates MADS outperforms GPS in terms of convergence properties (Abramson et Audet, 2006; Audet et Dennis Jr., 2006). As a matter of fact, in GPS the Poll directions are restricted to a finite set and GPS convergence results are closely tied to these fixed directions. In contrast, in MADS a dense set of Poll direction is generated which allows stronger convergence results. (Audet et Dennis Jr., 2006) presents a number of problems for which GPS stagnates while MADS converges to an optimal solution.

2.6.2 Gradient-based optimization methods

Gradient-based optimization methods (Nocedal et Wright, 1999; Geers *et al.*, 1999a) such as the conjugate gradient method (Claire *et al.*, 2007) and the Gauss-Newton method (Forestier *et al.*, 2002; Meuwissen *et al.*, 1998; Chafra *et al.*, 2010) as well as relevant algorithms like the Levenberg-Marquardt (Springmann et Kuna, 2003) and the Trust-Region (Nocedal et Wright, 1999) have been widely used in the literature. The main attribute of gradient-based optimization methods is their quick convergence in the vicinity of the global minimum. Nevertheless, the performance of a gradient-based method strongly depends on initial values, and it might easily fall to local minima if the initial guess is far from the global minimum.

In a blackbox optimization context, where there is no explicit relationship between the relevant model outputs and the unknown parameters, numerical approximations, such as finite-difference methods, must be exploited for derivative calculations. This obviously induces inevitable errors to the problem solutions. Moreover, regarding the cases where there are large numbers of unknown parameters, e.g. point-wise identification, gradient based optimization methods could be computationally expensive. This is because derivatives and Hessian calculations becomes very time-consuming.

2.6.3 Hybrid optimization method

A hybrid optimization takes the advantages of both derivative-free and gradient-based optimization methods to enhance the accuracy of solutions. The idea is to bring together the global searching capability of derivative-free algorithms and the high convergence rate of gradient-based optimization methods. The hybrid optimization algorithm consists of using at first a derivative-free algorithm in order to obtain solutions close to the global minimum. Results of the first derivative-free algorithm are then exploited as initial guesses of a gradient-based optimization method, as a local search algorithm, to reach more accurate set of sought parameters. Several studies have been carried out to show the superiorities of hybrid algorithms in comparison with derivative-free and gradient-based methods (Chaparro *et al.*, 2008; Bos, 1998).

2.7 Micromechanical homogenization models

Homogenization techniques aim at estimating the overall behavior of heterogenous materials from the mechanical properties of their constituents (Zaoui, 2002). In the case of composite materials with random microstructure, specifications such as geometrical and mechanical properties as well as the morphology of constituent phases (i.e., volume fraction, shape and orientation distribution of reinforcements) must be carefully determined for a successful homogenization. Different homogenization methods, mainly for linear elasticity, have been developed such as the bounds of Hashin-Shtrikman (HSB) (Hashin et Shtrikman, 1963), the self-consistent scheme (SCS) (Budiansky, 1965), the Mori-Tanaka (MT) model (Mori et Tanaka, 1973), the third order approximation (TOA) (Torquato, 1991), the model of Lielens (Lielens *et al.*, 1998), etc. The MT model yields the most accurate predictions for aligned-fiber composites with linearly elastic components, according to the investigations carried out by Tucker III and Liang (Tucker III et Liang, 1999). For 3D microstructures, the Lielens model and the third order approximation (TOA) have been proven to be more reliable for delivering accurate effective properties, particularly for composites having high volume fraction and contrast of properties (Ghossein et Lévesque, 2012).
Homogenization can also be performed numerically through FE and Fast Fourier Transfrom (FFT) techniques. The latter, proposed by Moulinec and Suquet (Moulinec et Suquet, 1998a), benefits from the computational efficiency of FFT and requires a uniform discretization of the microstructure. In contrast, the FE method is more user intensive due to difficulties encountered during meshing. The principal advantage of such methods is that they provide very accurate predictions, provided that they simulate Representative Volume Elements (RVE).

The functionality of different analytical homogenization methods have been compared with numerical methods for fiber reinforced composites in (Tucker III et Liang, 1999) and for 3D microstructures with spherical particles in (Ghossein et Lévesque, 2012). It was found that the Mori-Tanak model for fiber reinforced composites, and the TOA and Lielens models for particle reinforced composites were more accurate than the other models for estimating the effective properties.

CHAPTER 3

RATIONALE AND OBJECTIVES

3.1 Rationale of the thesis

Based on the literature review presented in the previous chapter, the rationale of the project can be summarized as follow:

1. The importance of full-field measurements application for the inverse identification of heterogenous materials mechanical properties has been addressed in several studies such as (Grediac, 2004) and (Avril *et al.*, 2008a). Mechanical characterization of various kinds of planar composites has been previously carried out. However, limited studies have been devoted to the characterization of composites constituent materials. Moreover, the majority of the published works have been conducted to retrieve in-plane properties resorting to planar displacement/strain fields obtained from the surface of material. Simultaneous identification of in-situ properties of constituent phases in bulk composites, using 3D full-field measurements, remains to be investigated.
2. Most of the studies carried out on mechanical characterization have been relying on updating finite element models. The FEMU methodology has been successfully applied to different materials due to its flexibility and high capabilities of simulating complex geometries and boundary conditions. This method, however, suffers from high computational costs specially when dealing with iterative simulation of 3D models. Previous studies have shown that both FEMU and the VFM resulted in lower uncertainties, when compared to other identification methods, due to their lower sensitivity to noise (Avril et Pierron, 2007). Nevertheless, the VFM presents direct (i.e. non-iterative) solution to the inverse problem, and no optimization process is required. In this sense, the VFM, which reconciles higher accuracy of parameters and computational efficiency, is very appealing.
3. The effect of regularization schemes, either using weighting functions or introducing bound constraints, have been assessed (Gokhale *et al.*, 2008; Genovese *et al.*, 2004; Florentin et Lubineau, 2010). Imposing additional mechanically relevant constraints, which link constituents parameters to homogenized properties, can further help to regularize the inversion process. Hence, further studies are required to improve both FEMU and VFM solutions so as to effectively reduce the influence of measurements uncertainties.

3.2 Objectives

The general objective of this research project was to develop inverse identification approaches based on full-field measurements in 2D and 3D, which are both fast and reliable against noise effects. This work was divided into three specific objectives:

1. **Developing a regularized FEMU approach**

   The first objective of this thesis aimed at developing and validating an improved FEMU approach based on the following essential phases:
   - The development of an inverse identification algorithm based on FEMU approach using the derivative-free optimization method (MADS);
   - The improvement of the accuracy of the approach by incorporating a hybrid optimization strategy;
   - The improvement of the developed algorithm further using additional regularization constraints, built up on the basis of an appropriate homogenization model;
   - The validation of the developed identification algorithms using noisy displacement fields of 2D artificial composites with different morphological and mechanical properties and under different boundary conditions;
   - The comparison of the noise sensitivity of the developed identification algorithms based on the accuracy of the obtained mechanical parameters.

2. **Developing a regularized VFM**

   The second specific objective of this thesis was to develop and validate an improved VFM, as an efficient algorithm in terms of both accuracy and computational costs, based on the following steps:
   - The development of an inverse identification algorithm based on the VFM for different loading and boundary conditions;
   - The improvement of the VFM solutions using additional regularization constraints;
   - The validation of the developed identification algorithms using heterogenous strain fields of various 2D artificial composites perturbed with different noise levels;
   - The comparison of the efficiency of the regularized VFM approach with the finite element based identification methods developed in the previous objective;
   - The investigation of the influence of size of Region of Interest (ROI) on the accuracy of the identified parameters using the developed approaches.

3. **Extension of the developed regularized VFM to 3D**

   The third specific objective of this thesis was to extend both the VFM and the regularized VFM to 3D based on the following phases:

- The development of an inverse algorithm based on the VFM for characterizing 3D composites constituents.
- The improvement of the VFM solutions using additional regularization constraints, similar to those employed for 2D composites.
- The assessment of functionality of the developed identification algorithms when dealing with 3D noisy full-field strain data of various artificial particulate composites.
- The investigation on the effect of size of ROI on the accuracy of the identified parameters using the developed approaches.

3.3 Scientific approach

The body of this thesis is divided into three sections. Each section is devoted to a research article prepared during this project so as to achieve the aforementioned objectives. The following describes the contents of each article as well as its context with respect to the three specific objectives.

3.3.1 Article 1: A new approach to inverse identification of mechanical properties of composite materials: Regularized Model Updating

This article presents an improved FEMU approach for in-situ identification of composites constitutive phases parameters from full-field measured displacement data. The improvements consisted first in incorporating a parallelized hybrid optimization algorithm in contrast to conventional FEMU algorithms developed in the literature. Regularization constraints were then added in order to reduce noise effects persistent in the measurements. The developed algorithm was tested by conducting several virtual experiments. The performance of the regularized algorithm was fairly compared to that of the FEMU approach. The acquired results confirmed the superiority of the regularized FEMU approach in delivering much more accurate mechanical parameters.

The main contributions of this paper are:

- An identification approach with a capability of execution in parallel mode, which enables speeding up the computational process;
- An enhanced inverse identification algorithm, which outperforms the previously developed FEMU approaches by its lower uncertainty, thanks to the regularization effects as well as the preventive role of the hybrid optimization in converging toward misleading parameters;
- A strategy that provides a balanced sensitivity in the identification algorithm to the

constitutive phases displacement fields, thanks to the regularization, which leads to similar quality of identified parameters for all phases in composites;
– A robust algorithm for the characterization of composites with large volume fractions and high contrast of properties in which the stiffer phase is usually adversely influenced by measurements uncertainties.

This article was published in the "Journal of Composite Structures" on August 15, 2013. This journal publishes papers that contribute to knowledge and applications of composite materials in engineering structures. This article was written 90% by the author of this thesis.

3.3.2 Article 2: Regularized virtual fields method for mechanical properties identification of composite materials

This article is concerned with developing an improved VFM for in-situ characterization of composites constitutive materials. This approach aimed at presenting a fast and reliable methodology, when compared with finite element based identification techniques. The VFM system of equations was solved in an optimization framework, in which mechanically motivated regularization constraints coming from a homogenization model were included. The method was tested using noisy measured strain fields of several 2D virtual composites with various mechanical and morphological characteristics. Its low sensitivity to noise effects directly characterized the robustness of this new technique. Moreover, the optimum size of region of interest was determined by considering the magnification requirements for DIC and the accuracy of the identified parameters.

The main contributions of this paper are:

– A promising inverse identification technique that reconciles lower uncertainties of identified parameters and higher computational efficiency;
– An investigation on the application of both VFM and regularized VFM for local parameters identification in fiber composites and their comparison with the previously developed finite element based techniques;
– A powerful tool for characterizing composites having higher-order heterogeneity of strain fields, where identification might result in inappropriate solutions for the stiffer phase that undergoes much less deformation;
– An investigation that can be very useful for the experimentalists to estimate, a priori, the required level of resolution in the imaging setup.

The revised manuscript of this article was submitted to the "Journal of Computer Methods in Applied Mechanics and Engineering" on January 17, 2014. This journal publishes original researches dealing with computational methods for simulation of complex physical problems,

such as in solid and structural mechanics. This article was written 90% by the author of this thesis.

3.3.3 Article 3: In-situ mechanical properties identification of 3D particulate composites using virtual fields method

This article presents the extension of the VFM and regularized VFM developed in the second article to 3D. Slight modifications with respect to the 2D approach were first discussed. The performance of both approaches was validated by applying 3D noisy strain fields of several artificial particle reinforced composites with different geometrical properties. This study can be considered as the first application of the VFM to 3D composites microstructure.

The main contributions of this paper are:

- A robust identification method to determine local properties in 3D microstructures form 3D full-field measurements inside material;
- An efficient identification algorithm which enables identifying constitutive parameters of 3D composites in a much lower computational time than finite element based algorithms.
- An investigation that helps proper selection of imaging resolution for accurate capturing of strain heterogeneities, and therefore, accurate retrieving of mechanical properties.

This article was submitted to the "International Journal of Solids and Structures" on March 4, 2014. This journal publishes original research on the mechanics of solid materials and structures in applied science and engineering. This article was written 90% by the author of this thesis.

CHAPTER 4

ARTICLE 1: A new approach to inverse identification of mechanical properties of composite materials: Regularized Model Updating

B. Rahmani, F. Mortazavi, I. Villemure, M. Levesque (2013). Published in the "journal of Composite Structures" in August 15, 2013.

4.1 Abstract

Inverse identification of constitutive parameters of materials might be adversely influenced by noise in the measured data. This study is concerned with an improved Finite Element Model Updating (FEMU) for accurate identification of mechanical properties of composite materials components from full-field measured displacement data. This numerical-analytical approach, namely Regularized Model Updating (RMU), is developed based on a hybrid constrained optimization algorithm. For this purpose, mechanical constraints, consisting of an appropriate homogenization model, are added as regularization factors to the optimization algorithm. The proposed method is validated by conducting several virtual experiments through elastic constitutive parameters identification of 2D composites. The sensitivity of the developed algorithm to different levels of noises of measured displacement fields is investigated. The identification results indicate that the proposed RMU methodology leads to higher accuracy of mechanical properties in comparison with FEMU method, particularly in the presence of random noise.

4.2 Introduction

Methods like Digital Image Correlation (DIC) and Digital Volume Correlation (DVC) provide full-field displacement/strain measurements on the surface, or even inside opaque materials, subjected to external loadings. Experimental availability of such rich information has given rise to different inverse identification methods for the constituents of heterogeneous materials (Avril *et al.*, 2008a). Among these methods, the Finite Element Model Updating (FEMU) technique is widely used due to its numerous advantages (Nair *et al.*, 2007; Springmann et Kuna, 2003; Molimard *et al.*, 2005). In this method, the material parameters input into a Finite Element (FE) model of an experiment are iteratively updated so as to minimize

the discrepancy between numerically predicted and experimentally measured fields (Zhou *et al.*, 2006). The FEMU does not require full-field measured data on the whole domain and, as a result, can be quite computationally-efficient (Genovese *et al.*, 2004). Moreover, since the method relies on finite element modeling, specimens with complex geometries and boundary conditions can be efficiently studied.

Several attempts have already been made by previous researchers to identify the mechanical properties of composites and their constituents, with the FEMU method (Ramault *et al.*, 2009). For example, Genovese et al. (Genovese *et al.*, 2005) identified the in-plane elastic properties of an eight-ply woven composite laminate based on simulated annealing optimization technique. Lecompte et al. (Lecompte *et al.*, 2007) obtained the in-plane elastic parameters of an orthotropic composite that was subjected to a biaxial loading, with FEMU and full field strain data. Magorou and Rouger (Le Magorou *et al.*, 2002) obtained the viscoelastic parameters of wood-based panels with FEMU relying on genetic optimization and optical metrology measurements. In-situ mechanical parameter identification has also been studied recently. For example, Kang et al. (Kang *et al.*, 2004) proposed an inverse method aiming at matching predicted and experimentally observed interfacial failure modes so as to identify fiber-matrix interface elastic properties of a metal matrix composite. A similar strategy was developed by Wang et al (Wang *et al.*, 2010) to identify interfacial viscoelastic properties using a video-recorded data acquisition system. Other important research efforts have dealt with the determination of damage constitutive laws by FEMU (Sztefek et Olsson, 2008, 2009). Geers et al. (Geers *et al.*, 1999b) also identified the parameters of gradient-enhanced damage model for glass-fiber reinforced polypropylene composites based on DIC measurements. Anghileri et al. (Anghileri *et al.*, 2005b) also determined damage parameters of carbon woven fabric fibre-reinforced composite by correlating crushing load obtained from FE simulation and experimental tests. In metallic materials domain, Meuwissen et al. (Meuwissen *et al.*, 1998) obtained isotropic von Mises and orthotropic Hill yield criterion in an elasto-plastic constitutive model of aluminum plates. Chaparro et al. (Chaparro *et al.*, 2008) investigated the hybrid algorithm superiorities in comparison with GA as well as gradient-based optimizations, identifying yield criterion and kinematic hardening parameters of the constitutive model for EN AW-5754 aluminium.

Although these approaches have been successfully applied, they may result in unreliable solutions due to the ill-posed nature of inverse methods. Several unavoidable factors such as image noise, FE approximation, DIC systematic errors and data interpolation will affect the accuracy of the solution in the optimization process. So, when one deals with real noisy measured data, the accuracy of identified parameters will greatly depend on the number of

local minima in the objective function. Nevertheless, local minima can be avoided by adding appropriate constraints, in a mathematical sense, to the related objective function. For instance, Oberai et al. (Oberai *et al.*, 2004) used Tikhonov regularization scheme (Aster *et al.*, 2005) to smooth the solution in the presence of noisy measured data. Adding a regularization term to the optimization led to relatively accurate results. Weber et al. (Weber *et al.*, 2007) developed a structural damage detection procedure based on model updating and a similar regularization method. It was demonstrated that the accuracy of stiffness reduction factors is significantly improved when compared with non-regularized cases. A robust inverse identification algorithm is therefore required to achieve reliable material parameters.
A new regularized model updating methodology for the accurate mechanical parameters identification of composite materials is proposed in this study. The novelty of the approach is that the identification problem is regularized by mechanically relevant constraints. For this purpose, a micromechanical homogenization model is used to create mechanical constraints. The inverse procedure is developed using a hybrid optimization technique i.e. a combination of a derivative-free optimization method followed by a gradient-based method. The new methodology is applied to artificial aligned long fiber composites. In order to evaluate the robustness of the approach, different mechanical properties and noise levels are studied.
This paper is organized as follows. Section 4.3 deals with background information related to this work. The new regularized model updating methodology is described in Section 4.4. Sections 4.5 and 4.6 deal with the application of the new methodology on the virtual composites, and Section 4.7 concludes the study.

4.3 Background

4.3.1 Optimization algorithms

Three categories of optimization techniques have been mainly exploited in previous FEMU applications: evolutionary algorithms, direct search (derivative-free) algorithms and gradient-based algorithms. Evolutionary algorithms, such as Genetic Algorithms (GAs), have successfully been employed in finite element model updating in the past, e.g. for determination of viscoelastic parameters for wood-based panels (Le Magorou *et al.*, 2002), identification of fiber-matrix interfacial elastic parameters for composites (Kang *et al.*, 2004), optimization of hyperelastic cardiac materials parameters (Nair *et al.*, 2007) and damage parameters identification in large-scale structures (Perera et Ruiz, 2008). The solution accuracy depends strongly on evolution parameters, namely population size, crossover and mutation rate, for which the related optimal values must be found by numerical experimentation. If these pa-

rameters are not carefully chosen, the iterative optimization may converge to an undesirable solution. In addition, the performance of GA does not depend on an initial solution, and local minima are generally avoided in this method.

Derivative-free optimization techniques, like the Generalized Pattern Search (GPS) method (Torczon *et al.*, 1997), are typically used for those optimization problems whose objective functions are not continuous or differentiable. GPS has been introduced for unconstrained or bound constrained optimization cases. At each step, the objective function is evaluated at a finite number of specific points. However, the polling area in GPS is restricted to a finite set of directions. This drawback has been solved by the Mesh Adaptive Direct Search (MADS) method (Audet et Dennis Jr., 2006; Le Digabel, 2011; Abramson *et al.*, 2011). MADS is a frame-based optimization algorithm for nonlinear problems. It can deal with a wide range of nonsmooth objective functions under nonsmooth constraints without having any derivative information. The key advantage of MADS over GPS is that it can perform local exploration using an asymptotically dense set of polling directions. Another attribute of MADS is that infeasible trial points are constrained and discarded relying on applied constraints. Moreover, MADS can be executed in parallel mode on multiprocessor machines (Le Digabel *et al.*, 2010). Both attributes are very advantageous for time-consuming blackbox optimizations. Examples presented in (Audet et Dennis Jr., 2006) show how GPS method stagnates, while MADS converges to an optimal solution. The method is known to be quite robust for constrained optimization, especially when dealing with nonsmooth objective functions (Le Digabel, 2011).

In both evolutionary and direct search algorithms however, as for continuous optimization algorithms, global minimum is not guaranteed and they might lead to sub-optimal solutions. Furthermore, these algorithms involve enormous evaluations of trial points, which implies that they are very time-consuming, especially for expensive blackbox optimization problems.

In contrast, the main attribute of gradient-based optimization techniques, such as the Gauss-Newton method (Forestier *et al.*, 2002; Chafra *et al.*, 2010; Nocedal et Wright, 1999) and the relevant algorithms like Levenberg-Marquardt (Springmann et Kuna, 2003; Nocedal et Wright, 1999) and Trust-Region (Nocedal et Wright, 1999), is that their efficiency strongly depends on initial guess for the set of unknown parameters. They have a rapid convergence in the vicinity of global minimum and, conversely, they might easily fall into local minima if the initial guess is far from the global minimum.

In order to improve the performance of gradient-based optimization, the result of a first GA or direct search algorithm can be considered as an initial solution of a subsequent gradient-based optimization. Combination of these two methods is referred to as 'hybrid optimization' (Chaparro *et al.*, 2008; Bos, 1998). The hybrid optimization inherits the benefits of both

evolutionary/direct search and gradient-based optimization methods. It brings together the global searching capability of evolutionary/direct search algorithms and the high convergence rate of gradient-based optimization methods. Moreover, the use of hybrid algorithms leads to an overall lower calculation time than when individually using evolutionary or direct search optimization method.

4.3.2 Mori-Tanaka model

The Mori-Tanaka homogenization model relates the composite constituents properties to its overall properties. According to this model (Mori et Tanaka, 1973), the stiffness tensor $\hat{\mathbf{C}}$ of a two-phase linearly elastic composite can be expressed as:

$$\hat{\mathbf{C}} = \mathbf{C^0} + c(\mathbf{C^1} - \mathbf{C^0}) : \mathbf{D} \tag{4.1}$$

where $\mathbf{C^0}$ and $\mathbf{C^1}$ are the stiffness tensors of the matrix and the fibers, respectively, c denotes the volume fraction of the fibers and $\mathbf{D}$ is the strain localization tensor given by:

$$\mathbf{D} = \mathbf{L^1} : \Big((1-c)\mathbf{L^0} + c\mathbf{L^1}\Big)^{-1} \tag{4.2}$$

where $\mathbf{L^0} = \mathbf{I}$ (identity matrix), and $\mathbf{L^1}$ can be expressed as follows:

$$\mathbf{L^1} = \Big[\mathbf{I} + \mathbf{S^1} : \mathbf{C^0}^{-1} : (\mathbf{C^1} - \mathbf{C^0})\Big]^{-1} \tag{4.3}$$

Note that $\mathbf{S^1}$ is Eshelby's tensor and, for the aligned and continuous fiber composites, is only a function of the matrix Poisson's ratio (Bourgeois, 1994).

4.4 A new regularized model updating method

In the FEMU method, minimization of the second norm of the residuals is typically sought. As a result, the optimization procedure is formulated as a least-square problem that aims at minimizing $r(\mathbf{p})$ defined as:

$$r(\mathbf{p}) = \Big(\hat{\mathbf{u}} - \mathbf{u}(\mathbf{p})\Big)^T \cdot \Big(\hat{\mathbf{u}} - \mathbf{u}(\mathbf{p})\Big) + \Big(\hat{\mathbf{v}} - \mathbf{v}(\mathbf{p})\Big)^T \cdot \Big(\hat{\mathbf{v}} - \mathbf{v}(\mathbf{p})\Big) \tag{4.4}$$

where $\hat{\mathbf{u}}$ and $\hat{\mathbf{v}}$ are measured displacement fields (rearranged in vector form) in x and y directions respectively, $\mathbf{u}$ and $\mathbf{v}$ are corresponding numerical displacement fields calculated by FE analysis, $\mathbf{p} = \{p_1, ..., p_M\}$ is a vector of the M unknown constitutive parameters to be

optimized.

Due to the ill-posedness of the problem, appropriate mechanical constraints were imposed to the objective function. The key idea was to add some constraints to the minimization of $r(\mathbf{p})$ so that the predicted effective properties from an accurate micromechanical model match those from experimental measurements. We postulate that such constraint regularizes the problem and leads to more accurate results than minimizing an unconstrained objective function. Therefore, the new model updating problem aimed at minimizing $r(\mathbf{p})$ subjected to the following equality constraints:

$$\tilde{\lambda}_i(\mathbf{p}) = \hat{\lambda}_i \quad (i = 1, 2, ..., N) \tag{4.5}$$

where $\tilde{\lambda}$ is the predicted effective mechanical property from the micromechanical model, $\hat{\lambda}$ is the corresponding experimentally measured property and N is number of constraints. Considering the above constraints as regularization terms, one may replace the original objective function $r(\boldsymbol{p})$ by the following penalty function:

$$p(\mathbf{p}) = r(\mathbf{p}) + \sum_{i=1}^{N} \alpha_i \left(\tilde{\lambda}_i(\mathbf{p}) - \hat{\lambda}_i \right)^2 \tag{4.6}$$

where α_i are positive penalty parameters. The set of material parameters are then obtained by minimizing $p(\mathbf{p})$, which is an unconstrained optimization problem.

One of the remarkable features of this new methodology is that effective properties not related to the displacement/strain measurements can be used in the identification strategy. For example, consider the case of a long fiber composite like that illustrated in Figure 4.1. Consider further that displacement measurements are only available in the xy plane. Assume further that the composite's stiffness in the z direction is known. This property will also depend on the fiber and matrix properties. Therefore, adding a penalty for the out-of-plane stiffness in $p(\mathbf{p})$ could further improve the accuracy of the identification method since additional physical information is added to the problem.

4.5 Application of the RMU methodology to artificial composites

4.5.1 General methodology

The methodology consisted first in generating finite element meshes of uni-directional long fiber composites, with various mechanical properties contrasts and volume fractions, subjected to two different sets of boundary conditions. The resulting displacement fields

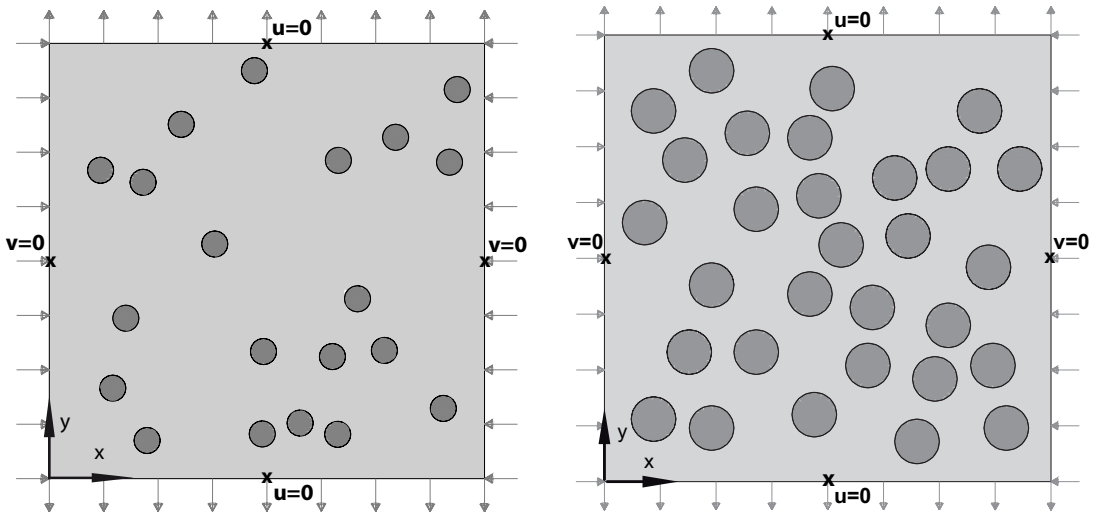

(a) (b)

Figure 4.1: 2D composites subjected to a bi-axial loading: (a) Composite A with fibers volume fraction of 5.5%, (b) Composite B with fibers volume fraction of 23.5%

were used to deform an artificial image and were subsequently perturbed by different levels of noise. These operations led to different sets of deformed and underformed images. A digital image correlation algorithm was then used to measure the displacement fields from the images (Mortazavi *et al.*, 2011b), which were considered as 'measured' displacements. The constraint terms of the penalty function in the RMU method were those predicted by the Mori-Tanaka model. For both FEMU and RMU, the optimization problem was solved with MADS and with an hybrid approach (MADS + Trust-Region).

4.5.2 Artificial composites and finite element model

Two computer-generated composite geometries were considered in this work consisting of an isotropic matrix reinforced with randomly distributed infinite isotropic cylindrical fibers. Figure 4.1 shows the artificial composites in xy plane. The volume fractions of fibers for the two composites were 5.5% (composite A) and 23.5% (composite B), and the overall composites were transversely isotropic. The constituent elastic properties for the virtual composites A and B are presented in Table 4.1. Composites A and B are very similar to E-glass - expoxy composites ($E_f/E_m \simeq 21$) whereas composites A' and B' are similar to carbon-epoxy composites ($E_f/E_m \simeq 100$). The virtual composites were subjected to bi-axial and uniaxial loadings, as shown in Figure 4.1 and Figure 4.2, respectively. The loading

Table 4.1: Reference elastic mechanical properties for the virtual composites

Composite name	$E_f(GPa)^a$	ν_f	$E_m(GPa)^b$	ν_m
volume fraction 5.5%				
Composite A	74	0.2	3.5	0.35
Composite A′	350	0.2	3.5	0.35
volume fraction 23.5%				
Composite B	74	0.2	3.5	0.35
Composite B′	350	0.2	3.5	0.35

a Subscript f refers to the fibers

b Subscript m refers to the matrix

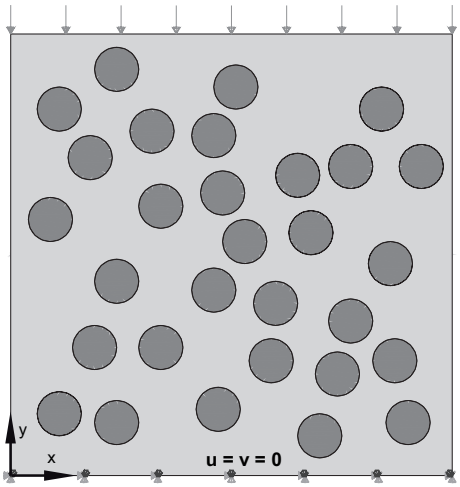

Figure 4.2: Uniaxial compressive loading applied on composite B

was introduced through pressure loads. The applied pressure loads were of 45 and -20 units in x and y directions respectively for the bi-axial loading, and of 45 units for the uniaxial loading. Only the properties in the transverse plane of isotropy (i.e. xy plane shown in Figure 1) were considered. Consequently, the composites were modeled with planar elements under plane stress conditions. `ABAQUS` 8-node reduced integration elements `CPS8R` were used and the element size was fixed after a convergence study. Figure 4.3 illustrates FE mesh of composite A in both x and y directions, and the related displacement field contour after

deformation under bi-axial loading condition.

4.5.3 Simulated full-field measurements

The FE predicted displacements were interpolated into a 512×512 uniform rectangular grid with the `TriScatteredInterp` function of Matlab. This function performs a bi-linear interpolation on a Delaunay triangulation generated from nodal coordinates. The obtained displacement field interpolated at pixel positions was used to artificially deform a computer-generated image. The synthetic image was generated using the Fractals theory, namely, 'Brownian motion' (Barnsley *et al.*, 1988). This random-value signal is generated such that its phase (in the frequency domain) is a random sequence, whereas the spectrum is inversely proportional to the frequency k according to the following relation:

$$\hat{f}_k \propto \frac{1}{|k|^{\frac{\beta}{2}}} \tag{4.7}$$

where β is a measure of texture roughness and $\hat{f}_k$ is the sequence of *correlated* random coefficients of the signal's Fourier transform. For the generated images herein, $\beta = 2$. The Fourier coefficients, once generated, were used to define the image in the spatial domain using the discrete Fourier transform:

$$f(x) = \sum_{k=1}^{N} \hat{f}_k \exp(i\, k \cdot x) \tag{4.8}$$

where $i = \sqrt{-1}$. Thanks to the analytical function definition presented above, the deformed image was generated by calculating the discrete values for $f(x - u(x))$, hence avoiding any interpolations and errors thereof. Figure 4.4 shows an example of a generated pair of undeformed-deformed images. The intensities were discretized into 12 bits to minimize the measurement errors due to quantization. In the second step, the generated images were analyzed using Digital Image Correlation (DIC) method in order to obtain measured displacement fields. The DIC algorithm used herein was based on an Improved Spectral Approach (ISA) (Mortazavi *et al.*, 2013b) that reconstructs continuous displacement fields from their Fourier basis functions. Thanks to the Fourier-based formulation, the algorithm leads to fast and accurate measurements using Fast Fourier Transform (FFT). Furthermore, the continuum-based framework on which the algorithm is developed enables more reliable measurements than those obtained by the subset-based algorithms (Mortazavi *et al.*, 2011a).

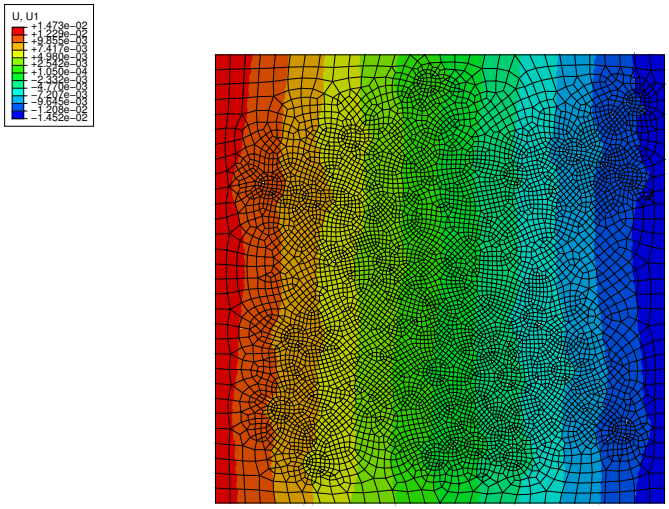

(a)

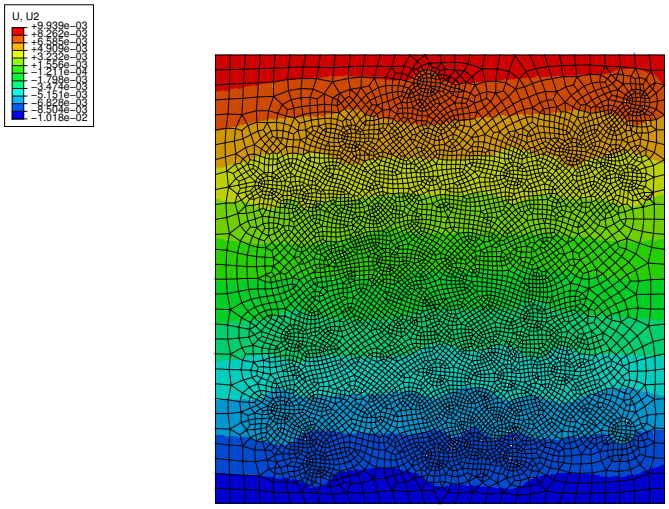

(b)

Figure 4.3: FE mesh and displacement fields contours for composite A, under biaxial loading: (a) x direction, (b) y direction

Measurement error was considered as the difference between the measured and FE displacement fields. The standard deviation of measurement error was used as an estimation of uncertainty between measured and FE data. Although the measured data did not contain noise-induced errors, systematic errors as well as the high spatial heterogeneities of strains disturbed the measured displacements, especially in the vicinity of fiber-matrix interfaces as well as inside fiber areas. Figure 4.5(b)compares the measured and numerical displacements in y direction along the path line illustrated on Figure 4.5(a). The figure shows the mismatch caused by algorithmic errors (with standard deviation of 6×10^{-6}) obtained with the exact mechanical parameters over path P-P.

For the purpose of assessing the stability of the RMU method, a set of measured displacement field representative of real experiment conditions was also simulated. To this end, noisy measured data with two different standard deviations of 10^{-4} and 1.6×10^{-4} were generated. The maximum level of standard deviation (1.6×10^{-4}) was chosen as 10% of the average of the mean displacement values in x and y directions (1.6×10^{-3}). The noisy measured displacement fields were obtained from images that had already been perturbed by noise effects. Gaussian white noise with different noise levels were added to the input images in different runs *prior* to the displacement measurements. Therefore, the resulting displacement fields contained higher variations. This procedure of providing input experimental data was favored over previous approaches (Grediac, 2004) in which the white noise would be added

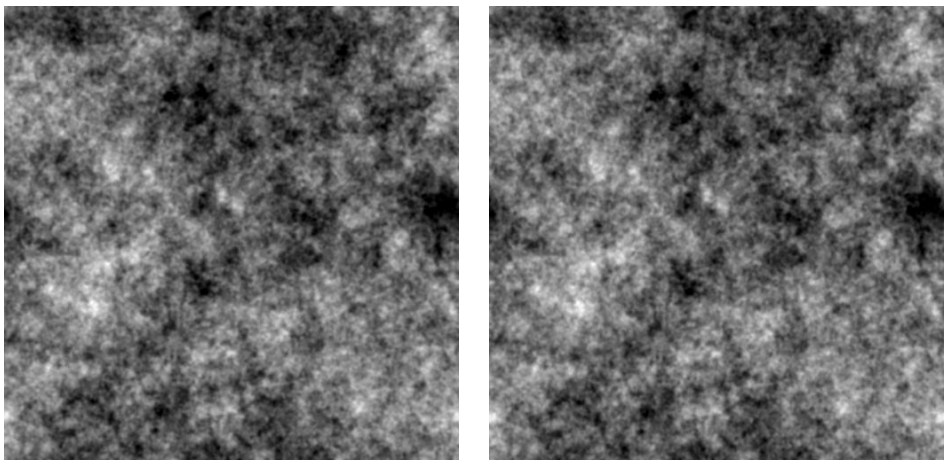

(a) (b)

Figure 4.4: (a) Undeformed and (b) deformed images

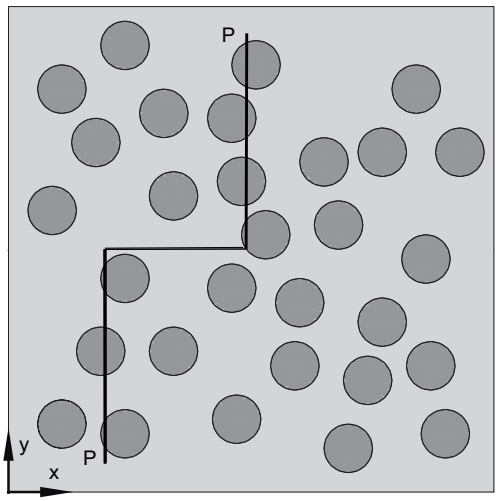

(a)

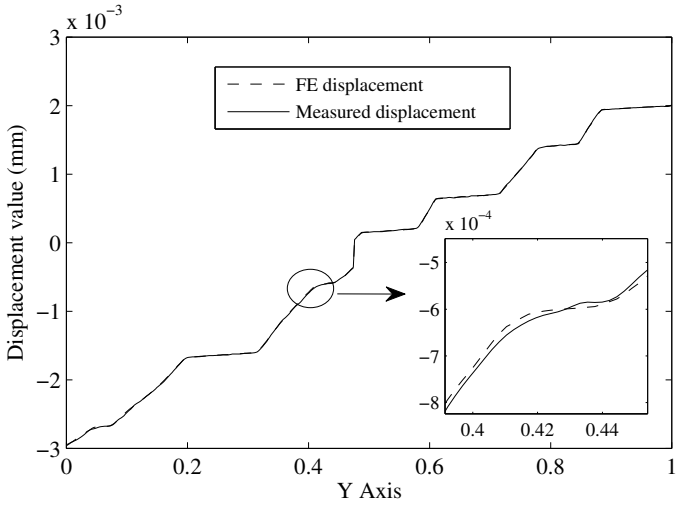

(b)

Figure 4.5: (a) Arbitrary path line over composite, (b) Measured and FE data comparison over path line P-P and mismatching around fibers

directly to perfect data so as to add uncertainties to the input displacement function for the identification algorithm. The current approach, indeed, takes into account the inevitable systematic errors caused by the DIC algorithm, which do not necessarily take the form of a white noise with zero mean value. Figure 4.6 depicts the noisy measured displacement data as well as FE data over path P-P (see Figure 4.5(a)).

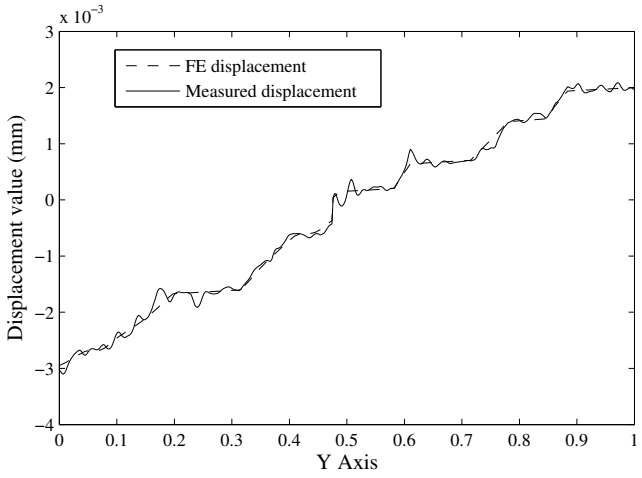

(a)

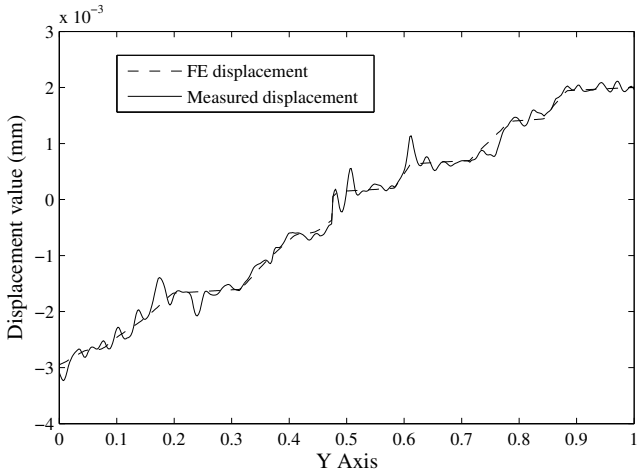

(b)

Figure 4.6: Noisy measured data versus FE data over path line P-P, (a) Standard deviation of 10^{-4} (b) Standard deviation of 1.6×10^{-4}

4.5.4 Inverse algorithm for identifying the unknown parameters

The aim of the inverse identification was to retrieve the reference elastic parameters of the composites constituents that were initially input to generate 'measured' displacement fields. The FEMU and RMU method presented in this paper were applied to minimizing $r(\mathbf{p})$ in Equation 4.4 and $p(\mathbf{p})$ in Equation 4.6, respectively. Displacement data in x and y directions were normalized numerically for the uniaxial loading condition since they had significantly different intensities. To do so, the least square value of each direction in the

objective function was divided by the corresponding mean value of measured data. For both cases, parallel MADS and an hybrid parallel MADS - Trust region strategy were used as optimization methods.

$p(\mathbf{p})$ (for RMU algorithm) requires the composite's effective properties that were computed from FE model. The material was deformed under out-of-plane (i.e. z direction) displacement boundary condition, and the required overall stress and elastic strain (i.e. σ_{zz} and ε_{xx}) were first calculated by the following relations:

$$\langle\sigma\rangle = \frac{1}{V}\sum_{i=1}^{n}\sigma_i\Delta V_i \tag{4.9}$$

$$\langle\varepsilon\rangle = \frac{1}{V}\sum_{i=1}^{n}\varepsilon_i\Delta V_i \tag{4.10}$$

where V denotes overall volume of the composite, σ_i and ε_i are the stress and elastic strains of elements integration points respectively, n is number of integration points and ΔV_i represents volumes associated to the integration points. Having known value of strain component in the longitudinal direction (ε_{zz}), and since σ_{xx}=0 the required effective properties for constraints, i.e. E_l and ν_{lt}, were directly obtained from the following stress-strain relationship (Hook's law):

$$\begin{Bmatrix}\varepsilon_{xx}\\ \varepsilon_{zz}\end{Bmatrix} = \begin{bmatrix}\frac{1}{\hat{E}_t} & -\frac{\hat{\nu_{lt}}}{\hat{E}_l}\\ -\frac{\hat{\nu_{tl}}}{\hat{E}_t} & \frac{1}{\hat{E}_l}\end{bmatrix}\begin{Bmatrix}\sigma_{xx}\\ \sigma_{zz}\end{Bmatrix} \tag{4.11}$$

where subscripts l and t refer to the out-of-plane and in-plane directions, respectively.

Composite samples are usually sufficiently large so as to be considered as Representative Volume Element (RVE) of a larger part. Micromechanical homogenization models are also based on the same hypothesis. It is well known that the effective properties predicted by numerical homogenization methods depend on the number of represented reinforcements (see (Kanit *et al.*, 2003) for example). A RVE study was therefore conducted so that these hypotheses hold. This study consisted in analysing the evolution of the composites effective properties as a function of the number of meshed fibers and for a number of realizations. To this end, the number of fibers were increased from 30 to 70 fibers, while preserving the same volume fraction, and 6 realizations were computed for each number of fibers meshed. Two-tailed 95% confidence intervals on the mean effective properties were calculated (the widths of the confidence intervals were smaller than 1% of the mean value). Figure 4.7 shows, for example, the convergence of E_l for composite B'. It can be seen from the figure that 60 fibers are needed to reach the RVE. The convergence study was only performed for

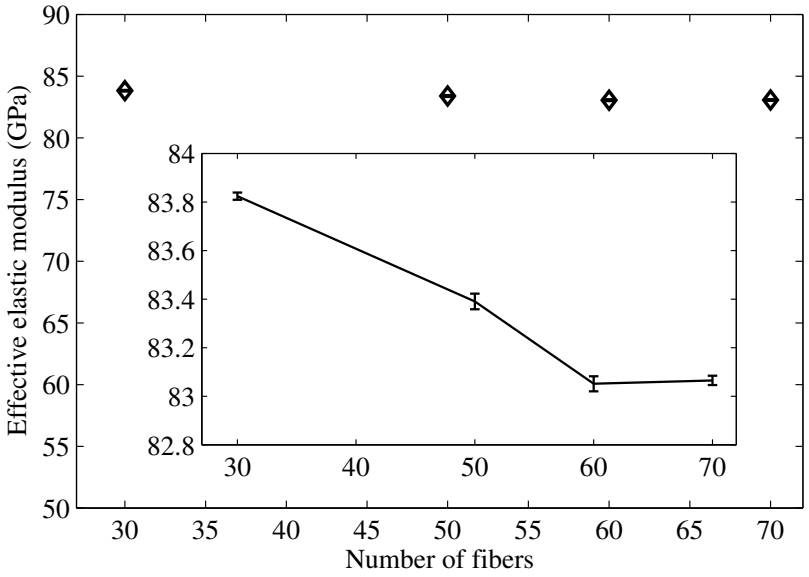

Figure 4.7: Variation of effective elastic modulus of composite B' and the related confidence intervals

the highest volume fraction and contrast (i.e. composite B') and the same size of RVE was considered for the other composites for calculating the corresponding effective properties. The obtained effective properties were used to make the following mechanical constraints of Equation 4.6:

$$\sum_{i=1}^{N} \alpha_i \Big(\tilde{\lambda}_i(\mathbf{p}) - \hat{\lambda}_i \Big)^2 = \alpha_1 \Big(E_l^{MT}(\mathbf{p}) - E_l \Big)^2 + \alpha_2 \Big(\nu_{lt}^{MT}(\mathbf{p}) - \nu_{lt} \Big)^2 \tag{4.12}$$

where superscript MT refers to Mori-Tanaka homogenization model. At each iteration, the numerical values of the constraints were simultaneously updated by substituting new material parameters into the Mori-Tanaka model. The penalty parameters α_1 and α_2 were considered as unity during both parallel MADS and gradient-based optimization processes.

The whole algorithm involved a blackbox that consisted of a main Matlab code and several subroutines. The Matlab file substituted new material parameters into the FE analysis input file and called a Python subroutine that launched FE analysis and extracted the relevant outputs at each iteration. The required field outputs (nodal displacements and coordinates) were extracted from the ODB file after completing FE analysis and were written into a text file. The data were read into a matrix and interpolated (using `TriScatteredInterp` function

in Matlab) onto a mesh grid, corresponding to the measured points. The main routine then evaluated either $r(\mathbf{p})$ or $p(\mathbf{p})$.
Assuming that there is not sufficient knowledge about the exact solution (target mechanical properties), relatively wide optimization upper and lower bounds were considered for the unknown parameters; Table 4.2 shows the specified bounds used at the beginning of identification. It should be noted that the updating parameters were scaled during optimization process.

Iterative evaluation of both $r(\mathbf{p})$ and $p(\mathbf{p})$ consisting of finite element simulations was significantly time consuming. Hence, MADS algorithm was parallelized on 8 processors so as to speed up the computational process. The stopping criterion for the MADS algorithm was reached when a maximum number of 500 objective function evaluations was performed. In the vicinity of global minimum, the Trust-Region algorithm converged much faster than MADS towards global optimum. The Trust-Region algorithm also stopped calculations when relative values of updating parameters or objective function was inferior to 10^{-6}. This stopping criterion was satisfied in all of the gradient-based optimizations within less than 15 iterations.

4.6 Results and discussions

Tables 3a to 3d present the results of the inverse identification associated with different composites under bi-axial loading condition. The acquired results show that MADS solutions are appropriate initial values for gradient-based optimization. Furthermore, much more accurate results are obtained by a subsequent Trust-Region algorithm (hybrid optimization).
For composite A (Table 4.3a) and, when dealing with data containing minimum level of noise, FEMU method results in a solution near to the exact parameters except for the fibers Poisson's ratio. As it can be seen from the table, more accurate values have been obtained for the matrix properties in all situations. This could be explained by the much larger volume fraction of the matrix (94.5%), which results in a predominant weight in the objective function. Moreover, the matrix is more compliant than the fibers, which results in a larger signal. Finally, the fibers are embedded into the matrix and, consequently, follow its deformation. As a result, the objective function becomes much more sensitive to the matrix displacement field and therefore, to the matrix parameters. When using RMU method, however, the mentioned unbalanced sensitivity is compensated and the resulting parameters are close to the exact solution. As the noise level increases to 10^{-4}, it can be seen that the accuracy of FEMU solutions decreases, especially for the fibers mechanical properties. In contrast, the RMU

Table 4.2: Initial bounds at the beginning of MADS optimization

material parameter	lower bound	upper bound
E_m(GPa)	1	200
E_f(GPa) (composite A and B)	10	300
E_f(GPa) (Composite A$'$ and B$'$)	100	500
ν_m and ν_f	0.13	0.49

method is only slightly affected by noise effects, so that much more accurate mechanical parameters are obtained. Increasing the level of noise to 1.6×10^{-4} revealed the same trends. For higher elastic modulus contrast (composite A') and when measurements contains minimum level of noise, identifications with both methodologies result in set of parameters very close to the exact values (Table 4.3b). By increasing the noise level, as for composite A, FEMU delivers poor results and is quite sensitive to the noise level. For the highest level of noise (1.6×10^{-4}), it is even probable that the quality of MADS solution not to be improved by gradient-based algorithm, and instead, be inclined toward farther local minima. The uncertainties for composite A' are higher than those for composite A, especially for fibers parameters. It is most likely because stiffer fibers undergo less deformation and the ratio of matrix to fiber deformation will be greater in composite A' than that in composite A. As a result, the objective function sensitivity to the matrix parameters is intensified when dealing with higher stiffness contrast. It can also be observed that the RMU method is significantly less sensitive to noise effects and also yields solutions with much lower uncertainty when compared with FEMU method.

Table 4.3a: Identified parameters by FEMU and RMU methods for composite A in various standard deviations (Std. dev.) - bi-axial loading

Method	Std. dev.	$E_f(GPa)$ $(error\%)$	ν_f $(error\%)$	$E_m(GPa)$ $(error\%)$	ν_m $(error\%)$	$obj.fun.value$ $(\times 10^{-4})$
Target parameters	–	74	0.2	3.5	0.35	–
FEMU (MADS)	6×10^{-6}	138.25 (86.8%)	0.154 (23%)	3.36 (3.9%)	0.256 (26.8%)	70
FEMU (hybrid)	6×10^{-6}	75.46 (1.98%)	0.162 (19%)	3.49 (0.3%)	0.347 (0.85%)	4
RMU (MADS)	6×10^{-6}	78.71 (6.4%)	0.152 (25%)	3.37 (5%)	0.291 (17%)	209
RMU (hybrid)	6×10^{-6}	74.20 (0.16%)	0.220 (10%)	3.50 (0%)	0.351 (0%)	89
FEMU (MADS)	1.0×10^{-4}	13.57 (81.6%)	0.131 (34.5%)	3.82 (9.1%)	0.448 (28.1%)	85
FEMU (hybrid)	1.0×10^{-4}	83.44 (12.7%)	0.139 (30%)	3.71 (6.1%)	0.358 (2.2%)	68
RMU (MADS)	1.0×10^{-4}	78.05 (5.6%)	0.445 (125%)	3.58 (2.3%)	0.314 (10.2%)	87
RMU (hybrid)	1.0×10^{-4}	72.66 (2.2%)	0.222 (11%)	3.50 (0%)	0.351 (0%)	68
FEMU (MADS)	1.6×10^{-4}	48.00 (35%)	0.147 (26.2%)	3.79 (8.6%)	0.357 (2.1%)	70
FEMU (hybrid)	1.6×10^{-4}	86.08 (16.3%)	0.350 (75%)	3.71 (6%)	0.340 (2.8%)	64
RMU (MADS)	1.6×10^{-4}	71.31 (3.6%)	0.445 (125%)	3.40 (2.8%)	0.315 (10%)	81
RMU (hybrid)	1.6×10^{-4}	75.82 (2.5%)	0.219 (9.5%)	3.49 (0.3%)	0.349 (0.28%)	69

Table 4.3b: Identified parameters by FEMU and RMU methods for composite A' in various standard deviations (Std. dev.) - bi-axial loading

Method	Std. dev.	$E_f(GPa)$ $(error\%)$	ν_f $(error\%)$	$E_m(GPa)$ $(error\%)$	ν_m $(error\%)$	$obj.fun.value$ $(\times 10^{-4})$
Target parameters	–	350	0.2	3.5	0.35	–
FEMU (MADS)	6×10^{-6}	418.20 (19.4%)	0.150 (25%)	3.45 (1.4%)	0.337 (3.7%)	2
FEMU (hybrid)	6×10^{-6}	342.98 (2%)	0.244 (22%)	3.49 (0.3%)	0.351 (0%)	0.4
RMU (MADS)	6×10^{-6}	332.93 (5.2%)	0.292 (46%)	3.34 (4.6%)	0.309 (12%)	262
RMU (hybrid)	6×10^{-6}	347.10 (1%)	0.182 (9%)	3.49 (0.3%)	0.348 (0.57%)	73
FEMU (MADS)	1.0×10^{-4}	187.23 (46.5%)	0.130 (35%)	3.88 (2.85%)	0.389 (11.2%)	43
FEMU (hybrid)	1.0×10^{-4}	263.23 (24.8%)	0.131 (34.5%)	3.80 (8.6%)	0.359 (2.57%)	33
RMU (MADS)	1.0×10^{-4}	332.80 (5%)	0.158 (21%)	3.92 (11.5%)	0.450 (28.5%)	458
RMU (hybrid)	1.0×10^{-4}	344.41 (1.6%)	0.221 (10.5%)	3.51 (0.3%)	0.348 (0.57%)	33
FEMU (MADS)	1.6×10^{-4}	390.93 (11.7%)	0.152 (24%)	3.92 (12%)	0.451 (28.8%)	70
FEMU (hybrid)	1.6×10^{-4}	471.35 (34.66%)	0.451 (125%)	3.87 (10.7%)	0.369 (5.4%)	64
RMU (MADS)	1.6×10^{-4}	361.73 (3.3%)	0.180 (10%)	3.79 (8.5%)	0.260 (25.7%)	644
RMU (hybrid)	1.6×10^{-4}	343.55 (1.8%)	0.221 (10.5%)	3.52 (0.6%)	0.350 (0%)	71

For composites with larger volume fraction (composites B and B'), higher fibers volume fraction implies a larger diameter of fibers and, consequently, much more number of measurement points associated to the fibers. It could have been hypothesized that by augmenting the weight of the fibers data in the objective function the accuracy of the fibers related properties would have been improved. However, the obtained results showed that increasing the fibers volume fraction decreased the accuracy of fibers properties (Table 4.3c) in comparison with similar case in lower volume fraction. This could be associated to the fact that measured displacement field in the vicinity as well as inside fibers area is less accurate than that of lower volume fraction composites. As for composites A and A', FEMU is quite sensitive to the noise level whereas RMU algorithm is quite stable, even against high levels of noise. The identified parameters for higher contrast of 100 (composite B') are given in Table 4.3d. The accuracy of RMU results is lower for composites B and B' than for composites A and A'. This might be due to the fact that the accuracy of Mori-Tanaka homogenization model decreases with an increasing fibers volume fraction.

Tables 4.4a and 4.4b also show the resulting material parameters of composites A and B, obtained under uniaxial loading conditions, from both FEMU and RMU procedures. Table 4 shows that the accuracy of parameters obtained from unconstrained optimization decreased when changing the boundary conditions. Similar to the other boundary conditions, RMU delivered more accurate solutions than FEMU.

Table 4.3c: Identified parameters by FEMU and RMU methods for composite B in various standard deviations (Std. dev.) - bi-axial loading

Method	Std. dev.	$E_f(GPa)$ $(error\%)$	ν_f $(error\%)$	$E_m(GPa)$ $(error\%)$	ν_m $(error\%)$	$obj.fun.value$ $(\times 10^{-4})$
Target parameters	–	74	0.2	3.5	0.35	–
FEMU (MADS)	6×10^{-6}	52.34 (29.3%)	0.411 (105%)	3.65 (4.2%)	0.444 (27%)	46
FEMU (hybrid)	6×10^{-6}	71.55 (3.3%)	0.240 (20%)	3.49 (0.3%)	0.349 (0.28%)	0.1
RMU (MADS)	6×10^{-6}	55.31 (25.3%)	0.448 (124%)	3.43 (2.1%)	0.270 (22%)	33
RMU (hybrid)	6×10^{-6}	75.87 (2.4%)	0.218 (8%)	3.49 (0.3%)	0.353 (0.85%)	4
FEMU (MADS)	1.0×10^{-4}	60.53 (18.2%)	0.237 (18.6%)	3.98 (13.7%)	0.331 (5.3%)	371
FEMU (hybrid)	1.0×10^{-4}	63.59 (14%)	0.152 (24%)	3.71 (6.1%)	0.358 (2.2%)	35
RMU (MADS)	1.0×10^{-4}	76.11 (2.8%)	0.454 (127%)	3.28 (6.2%)	0.280 (20%)	56
RMU (hybrid)	1.0×10^{-4}	71.51 (3.4%)	0.212 (6%)	3.55 (1.5%)	0.356 (1.7%)	35
FEMU (MADS)	1.6×10^{-4}	84.66 (14.4%)	0.477 (138%)	3.24 (7.1%)	0.257 (26.5%)	84
FEMU (hybrid)	1.6×10^{-4}	101.2 (36.7%)	0.450 (125%)	3.26 (6.8%)	0.333 (4.8%)	66
RMU (MADS)	1.6×10^{-4}	71.75 (3%)	0.469 (134%)	3.34 (4.5%)	0.414 (17.7%)	206
RMU (hybrid)	1.6×10^{-4}	71.29 (3.6%)	0.184 (8%)	3.57 (1.8%)	0.344 (1.7%)	69

Table 4.3d: Identified parameters by FEMU and RMU methods for composite B' in various standard deviations (Std. dev.) - bi-axial loading

Method	Std. dev.	$E_f(GPa)$ $(error\%)$	ν_f $(error\%)$	$E_m(GPa)$ $(error\%)$	ν_m $(error\%)$	$obj.fun.value$ $(\times 10^{-4})$
Target parameters	–	350	0.2	3.5	0.35	–
FEMU (MADS)	6×10^{-6}	331.81 (5.2%)	0.450 (125%)	3.50 (0%)	0.359 (2.5%)	802
FEMU (hybrid)	6×10^{-6}	339.79 (2.9%)	0.242 (21%)	3.49 (0.3%)	0.349 (0.28%)	0.4
RMU (MADS)	6×10^{-6}	336.36 (3.8%)	0.210 (5%)	3.85 (10%)	0.390 (11.4%)	840
RMU (hybrid)	6×10^{-6}	347.45 (0.7%)	0.220 (10%)	3.49 (0.3%)	0.350 (0%)	14
FEMU (MADS)	1.0×10^{-4}	150.57 (57%)	0.150 (25%)	3.76 (7.5%)	0.385 (10%)	38
FEMU (hybrid)	1.0×10^{-4}	439.12 (25.4%)	0.291 (45.5%)	3.31 (5.3%)	0.341 (2.57%)	34
RMU (MADS)	1.0×10^{-4}	332.13 (5.1%)	0.418 (108%)	3.69 (6%)	0.376 (8%)	534
RMU (hybrid)	1.0×10^{-4}	338.32 (3.3%)	0.201 (0.5%)	3.57 (2%)	0.343 (2%)	34
FEMU (MADS)	1.6×10^{-4}	151.11 (57%)	0.140 (30%)	3.72 (6.4%)	0.393 (12.3%)	73
FEMU (hybrid)	1.6×10^{-4}	437.23 (24.9%)	0.331 (65.5%)	3.34 (4.4%)	0.338 (3.42%)	64
RMU (MADS)	1.6×10^{-4}	331.30 (5.3%)	0.154 (23%)	4.10 (17%)	0.403 (15%)	191
RMU (hybrid)	1.6×10^{-4}	335.21 (4.2%)	0.183 (8.5%)	3.62 (3.4%)	0.344 (1.7%)	65

Table 4.4a: Identified parameters by FEMU and RMU methods for composite A in various standard deviations (Std. dev.) - uniaxial loading

Method	Std. dev.	$E_f(GPa)$ $(error\%)$	ν_f $(error\%)$	$E_m(GPa)$ $(error\%)$	ν_m $(error\%)$	$obj.fun.value$ $(\times 10^{-4})$
Target parameters	–	74	0.2	3.5	0.35	–
FEMU (MADS)	6×10^{-6}	54.75 (26%)	0.174 (13%)	3.40 (2.8%)	0.297 (15%)	20
FEMU (hybrid)	6×10^{-6}	75.33 (1.8%)	0.192 (4%)	3.49 (0.3%)	0.347 (0.85%)	0.4
RMU (MADS)	6×10^{-6}	76.57 (3.4%)	0.158 (21%)	3.43 (2%)	0.355 (1.4%)	209
RMU (hybrid)	6×10^{-6}	74.30 (0.4%)	0.213 (6.5%)	3.51 (0%)	0.351 (0%)	7
FEMU (MADS)	1.0×10^{-4}	34.44 (40%)	0.130 (35%)	4.02 (14.3%)	0.441 (26%)	120
FEMU (hybrid)	1.0×10^{-4}	89.94 (21.6%)	0.359 (80%)	3.89 (11.4%)	0.341 (2.3%)	77
RMU (MADS)	1.0×10^{-4}	77.35 (4.5%)	0.421 (110%)	3.49 (0.3%)	0.318 (9%)	110
RMU (hybrid)	1.0×10^{-4}	73.45 (0.8%)	0.186 (7%)	3.51 (0%)	0.348 (0.5%)	86
FEMU (MADS)	1.6×10^{-4}	134.8 (80%)	0.130 (35%)	3.22 (8.3%)	0.330 (5.7%)	122
FEMU (hybrid)	1.6×10^{-4}	111.9 (51.3%)	0.335 (67.5%)	3.26 (6.9%)	0.340 (2.6%)	76
RMU (MADS)	1.6×10^{-4}	76.20 (2.9%)	0.440 (120%)	3.44 (1.5%)	0.265 (24%)	230
RMU (hybrid)	1.6×10^{-4}	75.05 (1.3%)	0.182 (9%)	3.49 (0%)	0.353 (0.85%)	94

Table 4.4b: Identified parameters by FEMU and RMU methods for composite B in various standard deviations (Std. dev.) - uniaxial loading

Method	Std. dev.	$E_f(GPa)$ $(error\%)$	ν_f $(error\%)$	$E_m(GPa)$ $(error\%)$	ν_m $(error\%)$	$obj.fun.value$ $(\times 10^{-4})$
Target parameters	–	74	0.2	3.5	0.35	–
FEMU (MADS)	6×10^{-6}	42.33 (42.7%)	0.380 (90%)	3.41 (2.5%)	0.335 (4.3%)	11
FEMU (hybrid)	6×10^{-6}	71.96 (2.6%)	0.229 (14.6%)	3.49 (0.3%)	0.350 (0%)	0.4
RMU (MADS)	6×10^{-6}	68.18 (8%)	0.130 (35%)	3.45 (1.6%)	0.342 (2.2%)	826
RMU (hybrid)	6×10^{-6}	72.27 (2.3%)	0.220 (10%)	3.50 (0%)	0.350 (0%)	7
FEMU (MADS)	1.0×10^{-4}	220.0 (197%)	0.133 (33%)	3.21 (8.3%)	0.371 (6%)	541
FEMU (hybrid)	1.0×10^{-4}	118.4 (60%)	0.130 (35%)	3.38 (3.3%)	0.355 (2.57%)	82
RMU (MADS)	1.0×10^{-4}	75.25 (1.7%)	0.410 (105%)	3.54 (1%)	0.295 (15.7%)	111
RMU (hybrid)	1.0×10^{-4}	72.70 (1.7%)	0.211 (5.5%)	3.44 (1.7%)	0.343 (2%)	88
FEMU (MADS)	1.6×10^{-4}	21.25 (71%)	0.164 (17.7%)	3.84 (9.8%)	0.355 (1.6%)	121
FEMU (hybrid)	1.6×10^{-4}	178.0 (140%)	0.130 (35%)	3.79 (8.3%)	0.358 (2.2%)	58
RMU (MADS)	1.6×10^{-4}	66.98 (10.8%)	0.450 (125%)	4.00 (14%)	0.215 (38%)	111
RMU (hybrid)	1.6×10^{-4}	71.12 (3.9%)	0.185 (7.5%)	3.47 (0.85%)	0.358 (2.2%)	98

To intuitively compare the efficiency of the two identification approaches, the average uncertainty of each of the identified parameters (i.e. relative error of the solutions with respect to the target values) are demonstrated separately in Figure 4.8. The figure shows that the FEMU method is quite sensitive to noise effects, whereas the RMU method is very robust.

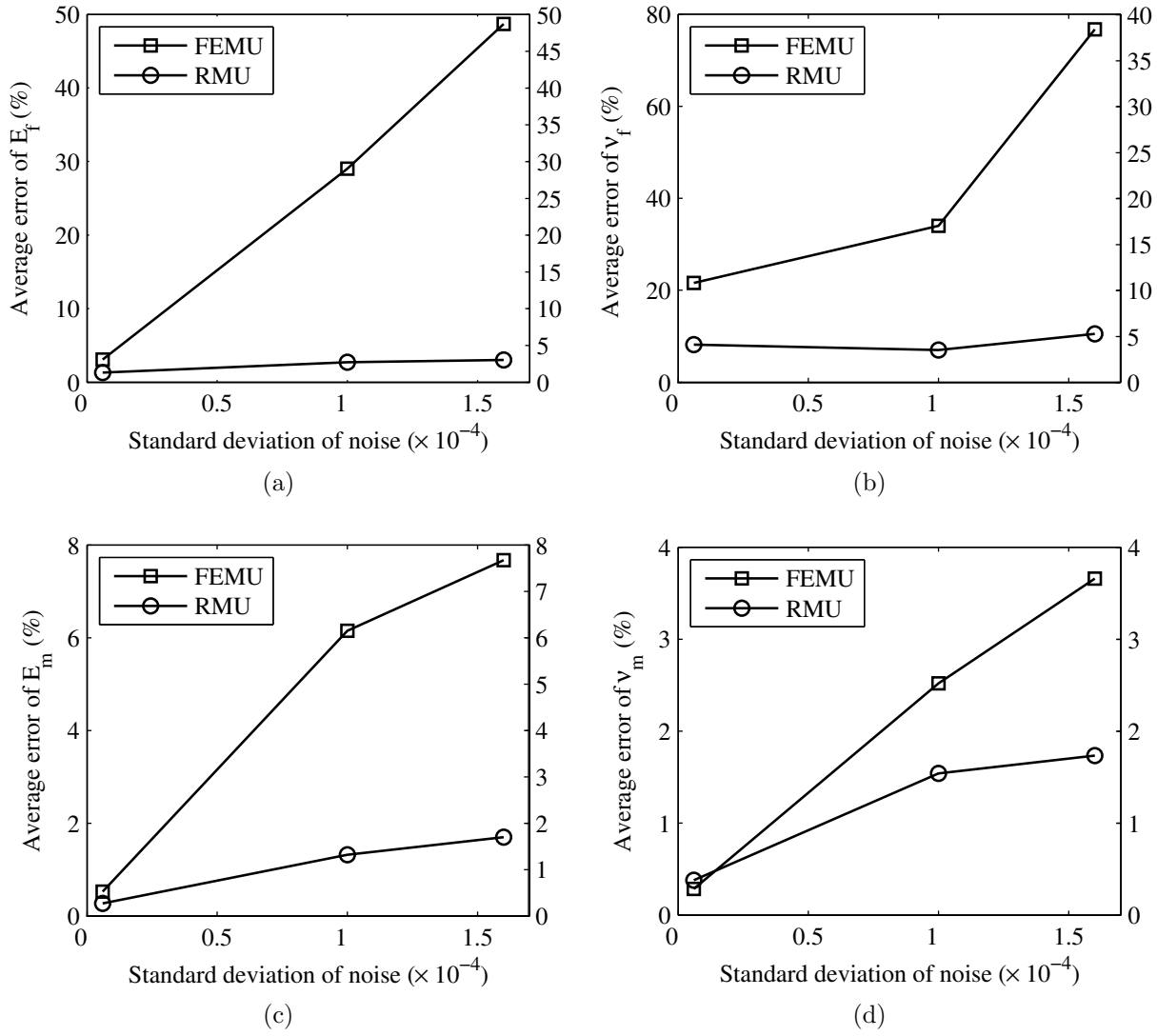

Figure 4.8: Average error of each parameter against various levels of noise: (a) Average error of E_f, (b) Average error of ν_f, (c) Average error of E_m, (d) Average error of ν_m

4.7 Concluding remarks

A new Regularized Model Updating method was developed to enhance the accuracy of composites constituents properties identification. The novelty of the approach is that mechanically motivated regularization constraints coming from a micro-mechanical model were included. In addition, the optimization was carried out very efficiently with a parallelized direct search method and refined with a gradient-based algorithm.

The new identification methodology was applied on noisy measured displacement field of 2D virtual composites so as to evaluate its performance. Results of the study indicates that the average accuracy of the new Regularized Model Updating method is much higher than that of Finite Element Model Updating method. Its low sensitivity to noise effects directly characterizes the robustness of this new identification method. Moreover, considering the solutions of a direct search optimization algorithm as initial guesses for a subsequent gradient-based algorithm led to more accurate final solution. These works relied on artificial images and validation on real images would be of considerable interest. Depending on the reinforcement sizes, experimental validation of the algorithm will be performed in the near future by our research group on samples loaded in a universal tensile testing frame and imaged with a long distance microscope, or for in-situ tensile testing into a Scanning Electron Microscope (SEM).

CHAPTER 5

ARTICLE 2: Regularized virtual fields method for mechanical properties identification of composite materials

B. Rahmani, I. Villemure, M. Levesque (2013). Revised manuscript was submitted to the "journal of Computer Methods in Applied Mechanics and Engineering" on January 17, 2014.

5.1 Abstract

This paper presents a new material parameters identification method based on the Virtual Fields Method (VFM) where a regularization term coming from a micromechanical model has been added. In this Regularized Virtual Fields Method (RVFM), the system of equations associated to the VFM is solved within a constrained optimization framework. The method was applied to virtual Scanning Electron Microscope in-situ tests aiming at determining the local properties of uni-directional composites loaded in the transverse direction and for which the strain fields were obtained through Digital Image Correlation (DIC). The method was tested for composites with various volume fractions and properties contrasts and under different boundary conditions. The potentials and limitations of the algorithm in the presence of noisy images was investigated and compared to that of the VFM and the other finite element based methods. The corresponding results indicate that the proposed RVFM is more efficient than the other identification techniques in terms of both accuracy and computational time. An optimum size of region of interest was also determined by taking into account DIC magnification requirements and based on the accuracy of the identified parameters. This kind of study can be very useful for determining, a priori, the level of resolution in the imaging system required for a favorable accuracy of the identified parameters.

5.2 Introduction

Classical approaches of material characterization, such as standard tensile tests, are capable of determining the effective properties of materials under the assumption of homogeneous stress/strain fields. Full-field measurement techniques, such as Digital Image Correlation (DIC) (Hild et Roux, 2006a) and Digital Volume Correlation (DVC) (Bay *et al.*, 1999a), are increasingly used in the field of mechanical properties identification. These techniques can

provide displacement or strain fields on the surface, or even inside, opaque materials subjected to external loadings. Thanks to the experimental availability of such rich information, several identification techniques, either in the form of an inverse problem or direct methods have been developed. Unlike standard tests, these approaches allow the simultaneous identification of a set of mechanical properties in heterogeneous materials with a single, carefully designed, test. The Finite Element Model Updating (FEMU) (Avril *et al.*, 2008a; Springmann et Kuna, 2003; Genovese *et al.*, 2004) is the most commonly used approach. The Adjoint-Weighted Equation (AWE) method first proposed by Barbone et. al. (Barbone *et al.*, 2007) was used as a direct solution to solve inverse problems of incompressible isotropic plane-stress elasticity (Albocher *et al.*, 2009). Different approaches have also been developed by exploiting the intrinsic constitutive theory formulation for a wide range of materials. Gockenbach et. al. (Gockenbach *et al.*, 2008) proposed an equation error approach based on the minimization of the discrepancy in the equilibrium equation of materials subjected to regularization schemes. Studies have also been conducted to estimate local material properties based on Error in Constitutive Equation (ECE) method. In this regard, Mousawi et. al. (Moussawi *et al.*, 2013) identified linearly elastic isotropic material parameters on the basis of compatibility of the stress field and relying on measured strain fields. Furthermore, in a more recent application an improved version of this methodology, referred to as Modified ECE (MECE) method (Banerjee *et al.*, 2013), has been developed. This method aims at minimizing an ECE functional while treating the discrepancy between measured and computed displacement fields as a penalty term. Several studies have also been carried out for obtaining material parameters by relying on their average response when subjected to applied loads (Zhou *et al.*, 2006; Ghouati et Gelin, 2001). These classical identification techniques, named least squares methods, were deployed with the assumption of homogenous deformation state. The direct problem output is obtained either using FE method (Zhou *et al.*, 2006) or solving the respective boundary-value Partial Differential Equations (PDEs) (Jadamba *et al.*, 2008). The practical advantages of these methods is that they require neither imaging setup nor full-field kinematic quantities measurements and their derivative calculation.

An alternative to these methods is the Virtual Fields Method (VFM) (Pierron et Grédiac, 2012; Grédiac *et al.*, 2006), being known as a direct (i.e., non iterative) identification approach. The VFM was first proposed by Grédiac (Grédiac, 1989) and has been successfully exploited in various applications (Grédiac *et al.*, 1998; Pierron *et al.*, 2000a; Grédiac et Pierron, 2006). The method has been applied to identify bending (Grédiac, 1996; Grédiac *et al.*, 2003) and in-plane (Grédiac *et al.*, 2002c; Pierron *et al.*, 2007) properties of composite materials. Through-thickness characterization of composites, either with a linearly elastic or a

nonlinear behavior, have also been studied. For example, Pierron et al. (Pierron et Grédiac, 2000) and Moltard et al. (Moulart *et al.*, 2006) determined the stiffness constants of orthotropic laminated composites from full-field measurements through different test configurations. Grédiac et al. (Grédiac et Pierron, 2006) used the VFM for simultaneous identification of through-thickness properties governing nonlinear shear behavior of composites during an Iosipescu test. Moreover, a methodology based on piecewise virtual fields was proposed (Toussaint *et al.*, 2006) for detecting heterogeneities in functionally graded materials and determining local mechanical properties. Other studies, such as those conducted by Chalal et al. (Chalal *et al.*, 2004), dealt with the determination of damage parameters in composites. Unlike some of inverse methods, the VFM does not require specimen geometry modeling nor finite element calculations, and delivers materials parameters directly. The VFM is also less sensitive to noise than the other existing techniques, as investigated for instance by Avril et al. (Avril et Pierron, 2007; Avril *et al.*, 2004). Incorporating strain data in the VFM induces further uncertainties and requires more computations when compared with other inverse identification methods, such as FEMU and least squares approaches, that rely on displacement data. However, providing images using new imaging systems delivers lower intrinsinc noises and considerable progresses have been made in obtaining realistic strain fields, in 2D and 3D (Mortazavi *et al.*, 2013b,a). Table 5.1 summarizes the features of the identification strategies presented above.

In-situ mechanical testing consists of observing the local kinematic quantities in the constituents of heterogeneous materials submitted to external loadings. In-situ mechanical testing can be carried out in a dedicated tensile testing machine embedded into a Scanning Electron Microscope (SEM) (Canal *et al.*, 2012) or into a micro Computed Tomography (μCT) scanner (Bay *et al.*, 1999b). Combination of these observations with DIC or DVC and an identification strategy could provide a means to measure local properties such as interface strength, in-situ local properties, etc. However, as shown in Figure 5.1, the Region of Inter-

Table 5.1: Specifications of different identification methods

Identification method	Procedure	Direct problem	Need for full-field data
FEMU	iterative	FE analysis	✓
AWE based	iterative	adjoint weighted equation	✓
ECE	iterative	constitutive equation	–
Least square	iterative	FE analysis / PDEs	–
VFM	non-iterative	—	✓

est (ROI) (i.e., real physical observation zone) in such techniques is much smaller than the sample itself and the load boundary conditions on the boundaries of this area (F'_x and F'_y) are unknown. Assuming homogeneous or any other type of boundary conditions could have an effect on the resulting properties. Finally, current SEM and μCT introduce important noise and artifacts that can affect the quality of the full field measurements.

Additional constrains can be added as regularization scheme to the problem for stabilizing the identification procedure. Different regularization strategies relying on constitutive relation error (Florentin et Lubineau, 2010), global variance analysis (Lubineau, 2009) and Tikhonov regularization (Oberai *et al.*, 2004) have already been studied in the literature. An improved FEMU strategy, named Regularized Model Updating (RMU), was recently introduced by the authors (Rahmani *et al.*, 2013a) in which regularization constraints based on a micromechanical homogenization model were added to the optimization algorithm. It was found that the regularization introduced by the micromechanical model rendered the algorithm quite robust with respect to noise effects. Although this procedure improved significantly the efficiency of the FEMU method, the method remained computationnally demanding due to time consuming finite element simulations.

The principal objective of this work was to introduce a new Regularized Virtual Fields Method (RVFM) for the accurate mechanical parameters identification of composite materials constituents. The regularization stems from a micromechanical model and the definition of an optimization problem within the framework of VFM. The approach was applied to identify the elastic properties of different 2D virtual long fiber composites. The performance of both VFM and RVFM methods was assessed for conditions as representative as possible as those encountered when performing SEM in-situ testing (noise on the images, systematic error induced by the DIC code, indetermination of boundary conditions). These choices were made in order to estimate the potential of the method for real applications.

This paper is organized as follows. Section 5.3 deals with theoretical background regarding the virtual fields method and homogenization. The new regularized virtual fields methodology is described in Section 5.4. Sections 5.5 and 5.6 present the application of the new methodology on the virtual composites and the related results, respectively. Section 5.7 concludes the study.

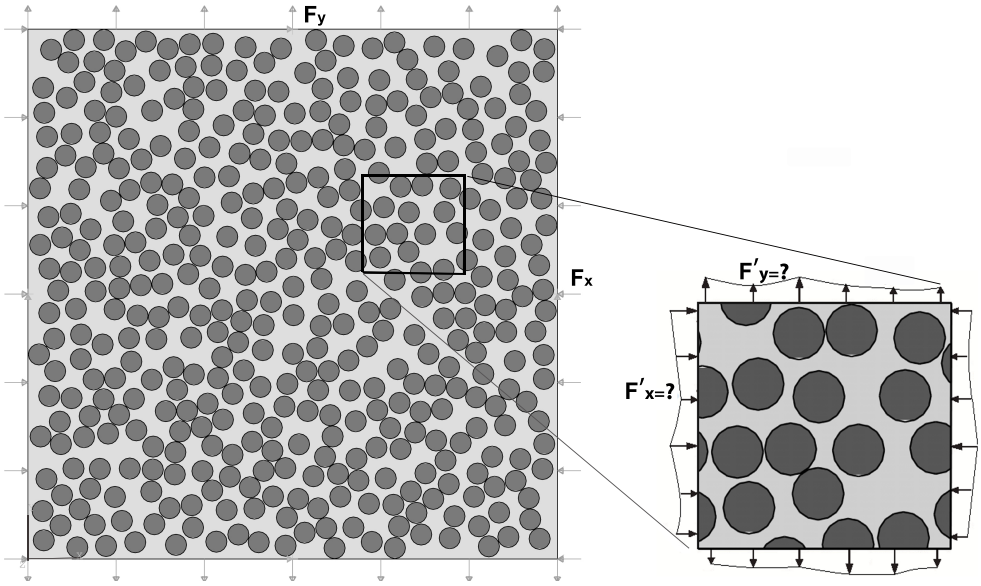

Figure 5.1: A long fiber composite sample and a typical region of interest

5.3 Theoretical background

5.3.1 Virtual fields method

The VFM derives from the Principle of Virtual Work (PVW) (Pierron et Grédiac, 2012) defined as:

$$-\int_V \sigma_{ij}\varepsilon^*_{ij}\,\mathrm{d}V + \int_{\partial V} T_i u^*_i\,\mathrm{d}S = 0 \quad \forall u^* \in \mathcal{K} \tag{5.1}$$

where V is the volume of the test specimen, ∂V is its boundary, σ and ε^* are the stress and the virtual strain tensors respectively, T are the tractions acting on the boundary of specimen (S), u^* is a virtual displacement field and $\mathcal{K}$ symbolizes the set of Kinematically Admissible (KA) virtual displacement fields. In the case of linear elasticity, the constitutive equation reads

$$\sigma_{ij} = C_{ijkl}\,\varepsilon_{kl} \tag{5.2}$$

where ε_{kl} are full-field measured strain components coming from experimental tests and C_{ijkl} are the stiffness components to be identified. The idea is to expand the principle of virtual work with a set of independent KA virtual fields, and to build up a system of linearly independent equations involving the unknown parameters. The chosen virtual field functions must be differentiable and have C^0 continuity. With the usual definition of simplified indices ($xx \rightarrow x$, $yy \rightarrow y$, $xy \rightarrow s$), the matrix form of the in-plane constitutive theory for an

orthotropic material is:

$$\begin{Bmatrix} \sigma_x \\ \sigma_y \\ \sigma_s \end{Bmatrix} = \begin{bmatrix} Q_{xx} & Q_{xy} & 0 \\ Q_{yx} & Q_{yy} & 0 \\ 0 & 0 & Q_{ss} \end{bmatrix} \begin{Bmatrix} \varepsilon_x \\ \varepsilon_y \\ \varepsilon_s \end{Bmatrix} \tag{5.3}$$

For plane stress problems, introducing Eq. 5.3 in Eq. 5.1 leads to:

$$\begin{aligned} Q_{xx} \int_S \varepsilon_x \varepsilon_x^* \, \mathrm{d}S + Q_{yy} \int_S \varepsilon_y \varepsilon_y^* \, \mathrm{d}S + Q_{xy} \int_S (\varepsilon_y \varepsilon_x^* + \varepsilon_x \varepsilon_y^*) \, \mathrm{d}S \\ + Q_{ss} \int_S \varepsilon_s \varepsilon_s^* \, \mathrm{d}S = \int_{L_f} T_i u_i^* \, \mathrm{d}l \quad \forall u^* \in \mathcal{K} \end{aligned} \tag{5.4}$$

where the $Q_{ij}s$ are the components of the in-plane stiffness matrix to be identified, S is the overall surface of the specimen and L_f is a line over which the tractions (T) are imposed. For the case of isotropic linear elasticity, where $Q_{xx} = Q_{yy}$, $Q_{xy} = Q_{yx}$ and $Q_{ss} = (Q_{xx} - Q_{xy})/2$, Eq. 5.4 reduces to:

$$\begin{aligned} Q_{xx} \int_S \left(\varepsilon_x \varepsilon_x^* + \varepsilon_y \varepsilon_y^* + \frac{1}{2} \varepsilon_s \varepsilon_s^* \right) \mathrm{d}S + Q_{xy} \int_S \left(\varepsilon_x \varepsilon_y^* + \varepsilon_y \varepsilon_x^* - \frac{1}{2} \varepsilon_s \varepsilon_s^* \right) \mathrm{d}S \\ = \int_{L_f} T_i u_i^* \, \mathrm{d}l \quad \forall u^* \in \mathcal{K} \end{aligned} \tag{5.5}$$

If as many different virtual fields as unknown parameters are chosen, Eq. 5.5 leads to the following linear system of equations:

$$\boldsymbol{A} \cdot \mathbf{q} = \mathbf{b} \tag{5.6}$$

where $\boldsymbol{A}$ is a square matrix representing the contribution of the internal virtual work and $\mathbf{b}$ is a vector whose components depend on the virtual work of the applied external loading. The vector of sought parameters $\mathbf{q}$ can be identified by solving the linear system of Eq. 5.6. Although solving this system of equation leads to a unique solution, variations in the measured data due to the presence of noise can affect the uniqueness condition and cause changes in the identified parameters.

The virtual field functions may be chosen among an infinite number of possibilities. However, these functions must satisfy some requirements (i.e. be differentiable, have C^0 continuity and be KA). Furthermore, the chosen virtual fields must be all independent from each other, thus making the determinant of $\boldsymbol{A}$ to be different from zero and, therefore, the linear system to be invertible. The stability of the linear system and the identified parameters when dealing with

noisy data depends strongly on the independence of the chosen virtual fields. Independent virtual fields induce a lower sensitivity of the linear system to noise and leads to more reliable identified parameters.
Special virtual fields (Grédiac *et al.*, 2002b) can also be devised so as to guarantee sufficient independence in the equations. Special virtual fields potentially render matrix $\boldsymbol{A}$ equal to the identity matrix $\boldsymbol{I}$, and therefore allows for a direct identification of the unknown parameters.

5.3.2 Mori-Tanaka homogenization model

The Mori-Tanaka homogenization model relates the composite constituents properties to its overall properties. According to this model (Mori et Tanaka, 1973), the stiffness tensor $\hat{\mathbf{C}}$ of a two-phase linearly elastic composite can be expressed as:

$$\hat{\mathbf{C}} = \mathbf{C^0} + c(\mathbf{C^1} - \mathbf{C^0}) : \mathbf{D} \tag{5.7}$$

where $\mathbf{C^0}$ and $\mathbf{C^1}$ are the stiffness tensors of the matrix and the fibers, respectively, c denotes the volume fraction of the fibers and $\mathbf{D}$ is the strain localization tensor given by:

$$\mathbf{D} = \mathbf{L^1} : \Big((1-c)\mathbf{L^0} + c\mathbf{L^1}\Big)^{-1} \tag{5.8}$$

where $\mathbf{L^0} = \mathbf{I}$ (identity matrix), and $\mathbf{L^1}$ can be expressed as follows:

$$\mathbf{L^1} = \Big[\mathbf{I} + \mathbf{S^1} : \mathbf{C^0}^{-1} : (\mathbf{C^1} - \mathbf{C^0})\Big]^{-1} \tag{5.9}$$

Note that $\mathbf{S^1}$ is Eshelby's tensor and, for aligned and continuous fiber composites, is only a function of the matrix Poisson's ratio (Bourgeois, 1994).

5.3.3 Optimization techniques

Numerous optimization techniques have been exploited in inverse identification applications. Gradient-based optimization methods (Forestier *et al.*, 2002; Chafra *et al.*, 2010), known as local search algorithms, may quickly converge in the vicinity of global minimum. However, their efficiency depends strongly on the chosen initial conditions such that they might easily fall into unfavorable local minima if the initial solution is far enough from the global optimum. Evolutionary optimization methods, such as Genetic Algorithms (GA) (Kang *et al.*, 2004), have been demonstrated to be robust optimization tools to solve nonsmooth and nonlinear optimization problems. The classical GAs, however, lack local search

ability and are computationally expensive for time-consuming blackbox optimizations. Alternative derivative-free approaches are those based on direct search algorithms such as Mesh Adaptive Direct Search (MADS) method. MADS is a global direct search optimization method that benefits from its exclusive local search capabilities. A key advantage of MADS over other direct search algorithms, such as the Generalized Pattern Search (GPS) method (Torczon *et al.*, 1997), is that it performs local exploration of a variable space and its local search is not restricted to fixed directions. MADS is a frame-based local optimization algorithm for solving nonlinear problems without having any derivative information. It is known as a robust optimization method for problems with nonsmooth objective functions subjected to nonsmooth constraints. The other attribute of MADS is that infeasible trial points are discarded with respect to the applied constraints, which can be beneficial when dealing with time-consuming objective functions. One drawback of the method is that it still requires more objective function evaluations before convergence, when compared to gradient-based optimization methods.

5.4 A new Regularized Virtual Fields Method (RVFM)

In the VFM, $\mathbf{q}$ is typically identified through the solution of a linear system of equations. An alternative way for solving the related linear system is to make use of an optimization procedure to be formulated as a Constraint Satisfaction Problem (CSP). With this thought, the vector $\mathbf{q}$ can be determined through the minimization of the following least square objective function:

$$r(\mathbf{q}) = (\boldsymbol{A} \cdot \mathbf{q} - \mathbf{b})^T \cdot (\boldsymbol{A} \cdot \mathbf{q} - \mathbf{b}) \tag{5.10}$$

Due to the high contrast between the composite's phases mechanical properties, as well as unavoidable noises in the measured strain fields, several inappropriate solutions may satisfy optimality conditions (Aster *et al.*, 2005). When the number of constraints is insufficient so that there exist infinitely many solutions that all satisfy the constraints, the CSP is said to be under-constrained. In such a situation the optimization process might converge to undesirable local minima that meet the applied constraints. On the other hand, a CSP is said to be over-constrained if no solution meeting all the constraints can be found. In such a case, the goal is to find a good compromise. Hence, appropriate mechanical constraints should be added to regularize the optimization process in Eq. 5.10. The key idea is to add some constraints to the minimization of $r(\mathbf{q})$ so that the predicted effective properties from an accurate micromechanical model match those obtained from experimental measurements.

The imposed constrains define a feasible promising region relying on the effective properties, thus leading to more accurate results than minimizing an unconstrained objective function. Therefore, the new RVFM aims at minimizing $r(\mathbf{q})$ subjected to the following constraints:

$$\mid \tilde{\lambda}_k(\mathbf{q}) - \hat{\lambda}_k \mid \leq \delta_k \quad (k = 1, 2, ..., N) \tag{5.11}$$

where the $\tilde{\lambda}_k$ are the predicted effective mechanical properties from the micromechanical model, $\hat{\lambda}_k$ are the corresponding experimentally measured properties, δ is a very small positive quantity and N is the number of constraints.
By defining the feasible set Ω to be the set of points $\mathbf{q}$ that satisfies the constraints:

$$\Omega = \{Q \mid \mid \tilde{\lambda}_k(\mathbf{q}) - \hat{\lambda}_k \mid \leq \delta_k\}, \tag{5.12}$$

the general formulation of the regularized virtual fields problem can be rewritten as:

$$\min_{Q \in \Omega} r(\mathbf{q}) \tag{5.13}$$

In this procedure, the solutions of a first VFM identification can be considered as an initial guess of a subsequent RVFM identification. One of the remarkable features of this new methodology is that effective properties not related to the measured strain fields can be used in the identification strategy. For example, consider the case of a long fiber composite like that illustrated in Figure 5.1. Consider further that strain measurements are only available in the xy plane. Assuming that the composite's out-of-plane effective stiffness is known and depends on the fiber and matrix properties, the imposed constraints restrict the algorithm to follow some rational search directions during optimization. Indeed, among the infinite number of solutions that might satisfy the optimality conditions, the applied constraints guide the search direction toward those solutions that can perfectly meet the composite's average mechanical response. This regularization can be interpreted as error averaging in the measured data that reduces significantly the noise effects, thus biasing the solution toward points very close to noise-free fields. Therefore, adding mechanical constraints when minimizing $r(\mathbf{q})$ could further improve the accuracy of the identified parameters since additional physical information is added to the problem.
Finally, the regularization would only be meaningful as long as the homogenization model used for imposing the constraints is reasonably accurate.

5.5 Application of the RVFM methodology to virtual composites

5.5.1 General methodology

The methodology first consisted of creating finite element meshes of uni-directional long fiber composites. Various composites with different constituents and fibers volume fractions, along with different sets of boundary conditions were investigated.
The resulting displacement fields from the finite element models were used to deform an artificial image and were subsequently disturbed by different levels of noise. Numerous sets of deformed and underformed images were provided. A digital image correlation algorithm was then used to measure the displacement fields from the images (Mortazavi *et al.*, 2011b). The required strain fields were then obtained by differentiating the displacement data and were considered as "measured" strain fields. The constraints values in the RVFM method were also evaluated by the Mori-Tanaka model. The optimization problem associated to the method was solved by Mesh Adaptive Direct Search (MADS) method (Audet et Dennis Jr., 2006). The following subsections provide methodological details for the above-mentioned steps.

5.5.2 Artificial composites and finite element model

`ABAQUS/Standard` was used for the finite element simulations. The computer-generated composites consisted of an isotropic matrix reinforced with randomly distributed infinite isotropic cylindrical fibers, as illustrated in Figure 5.2. The overall composites were transversely isotropic. Table 5.2 presents the properties of the fibers and matrix, where E stands for the Young's modulus, ν stands for the Poisson's ratio, and subscripts f and m refer to the fibers and matrix, respectively. As it can be seen from the table, three different volume fractions of 5.5%, 23.5% and 53% (for composites A, B and C, respectively) were examined. Two different elastic modulus contrasts were also considered for each volume fraction. Composites A, B and C were designed to be similar to E-glass-expoxy composites ($E_f/E_m \simeq 21$) whereas composites A', B' and C' were similar to carbon-epoxy composites ($E_f/E_m \simeq 100$).

Uniform load boundary conditions

The first analysis was related to the composites submitted to uniform traction on their boundaries. The composites were submitted to bi-axial or uniaxial loadings as shown in Figure 5.2 and Figure 5.3. The loading was introduced through pressure loads such that 45 and -20 units in x and y directions, respectively, were applied for the bi-axial loading,

Table 5.2: Reference elastic mechanical properties of the virtual composites

Composite	$E_f(GPa)$	ν_f	$E_m(GPa)$	ν_m
volume fraction 5.5%				
A	74	0.2	3.5	0.35
A′	350	0.2	3.5	0.35
volume fraction 23.5%				
B	74	0.2	3.5	0.35
B′	350	0.2	3.5	0.35
volume fraction 53%				
C	74	0.2	3.5	0.35
C′	350	0.2	3.5	0.35

and such that 45 units were applied for the uniaxial loading. It should be noted that the boundary conditions illustrated in Figure 5.2 only prevent rigid body motions due to the symmetric way in which they were imposed, and no additional perturbation is induced. Only

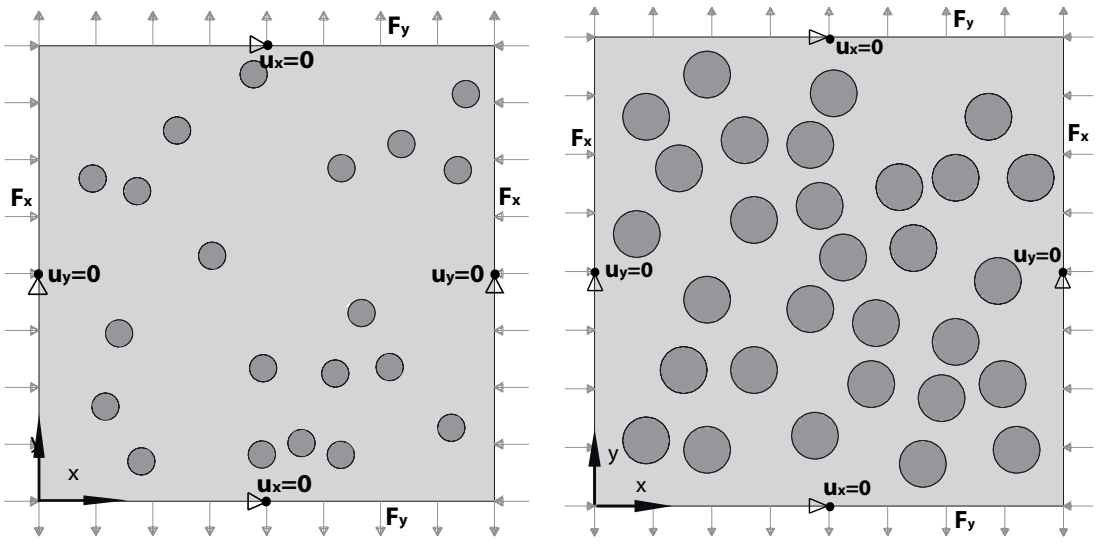

Figure 5.2: 2D composites subjected to a bi-axial loading and the displacement boundary conditions applied at the middle point of all boundaries; (a) Composite A with fibers volume fraction 5.5%, (b) Composite B with fibers volume fraction 23.5%

the properties in the transverse plane of isotropy (i.e. xy plane) were considered. The composites were modeled with planar elements under plane stress conditions. `ABAQUS` 8-node reduced integration elements `CPS8R` were used and the element size was fixed after a convergence study.

Small regions of interest

The load boundary conditions illustrated in Figure 5.2 and Figure 5.3 represents the ideal case where the loads are fully determined. In practice, however, the observation area is much smaller than the specimen and the load boundary conditions are not fully defined. Figure 5.4 illustrates the models used for simulating such composites. A relatively large volume of composite (3×3) was simulated and only a portion of the volume (1×1 central ROI) was used for the identifications.

Smaller sizes of ROIs 0.5×0.5, 0.25×0.25 and 0.1×0.1 were even simulated with the aim of investigating the influence of their size on the overall traction distribution. Figure 5.5 shows typical schematics of the mentioned ROIs. During the identifications, each ROI was considered as an independent continuum model that was in equilibrium through the tractions created on their boundaries, as illustrated in Figure 5.6. For each size of ROI, the parameters were identified from six various regions (consisting of different distribution of fibers in the matrix). The average relative errors with respect to the reference parameters were then obtained. Also note that the displacement boundary conditions illustrated on Figure 5.6 only prevent rigid body motions and do not induce any strains in the specimen.

For carefully chosen virtual fields, the only parameters involved are the overall applied stresses. If the ROI is large enough to be a Representative Volume Element (RVE), then the overall stress over that area should be the same as that applied on the whole sample. For small ROIs, however, such condition might only be approximative and will inherently lead to biased properties. From the DIC point of view, however, images with higher magnifications (that necessitate smaller ROIs) (Canal *et al.*, 2012), are better suited for capturing non-homogeneous strain fields in fiber composites. For this reason, the optimum ROI size should be a compromise between a small region that satisfies image magnification requirements and a large region that is a RVE.

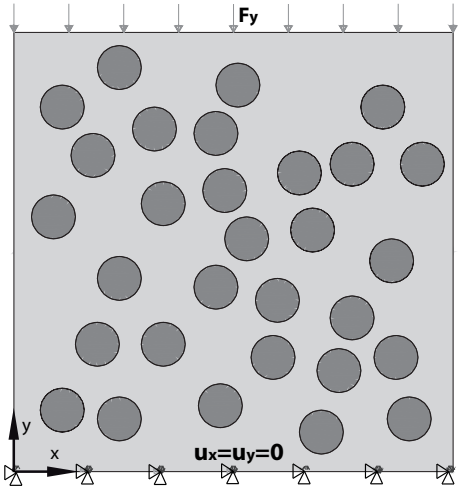

Figure 5.3: Composite B subjected to uniaxial compressive loading and the displacement boundary condition applied throughout the bottom boundary of composite

5.5.3 Simulated full-field measurements and noise effects

The displacement fields obtained from the FE simulations were interpolated onto a uniform rectangular grid. This was done with the `TriScatteredInterp` function of Matlab in

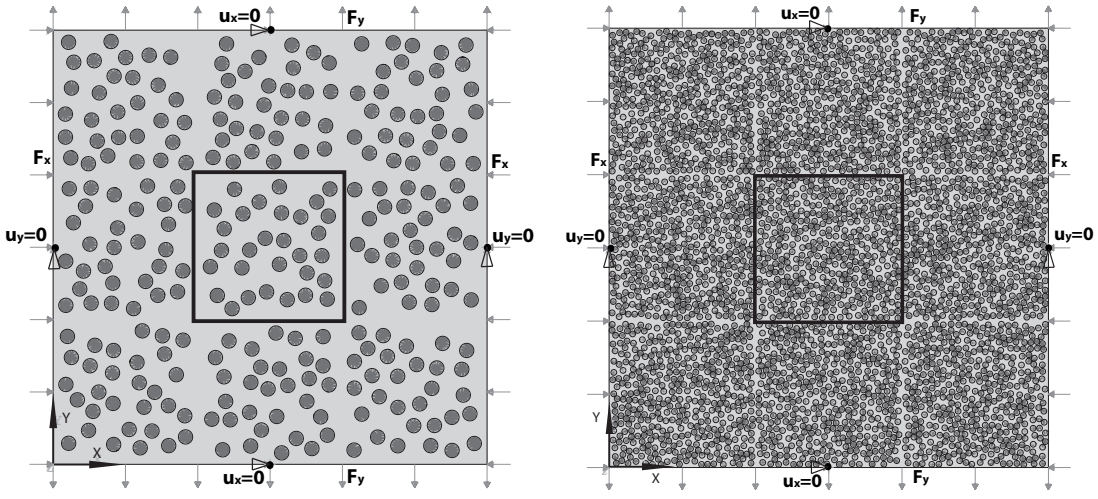

Figure 5.4: Large composites with the central ROI 1×1 specified on them; (a) composite B, (b) composite C

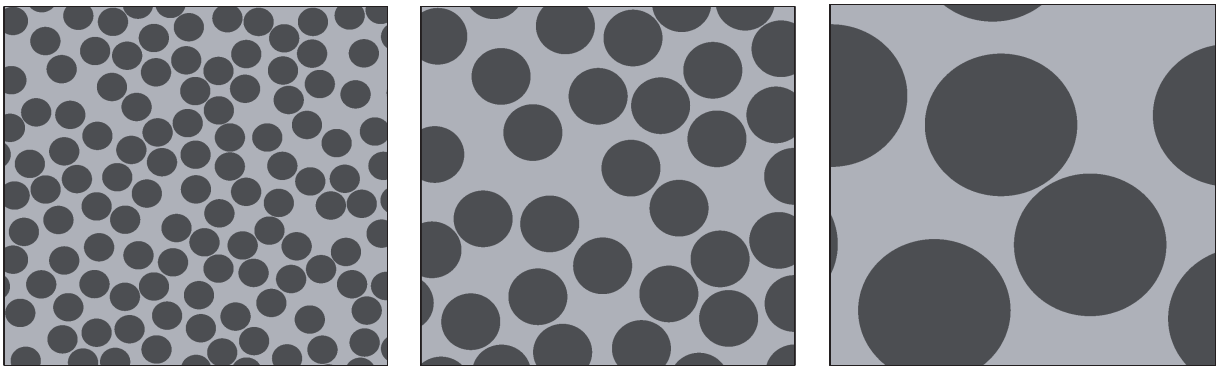

(a) (b) (c)

Figure 5.5: Regions of interest (ROIs) with different sizes; (a) ROI size 0.5×0.5, (b) ROI size 0.25×0.25, (c) ROI size 0.1×0.1

which a bi-linear interpolation is performed on a Delaunay triangulation generated from nodal coordinates. The resulting displacement fields were used to artificially deform a computer-generated image. Figure 5.7 shows an example of generated undeformed image. The procedure of generating the images is detailed in (Rahmani *et al.*, 2013a).

A DIC method was used to compute the displacement fields from the artificially generated images. The DIC algorithm used herein was based on an Improved Spectral Approach (ISA) Mortazavi *et al.* (2013b) that reconstructs continuous displacement fields from their

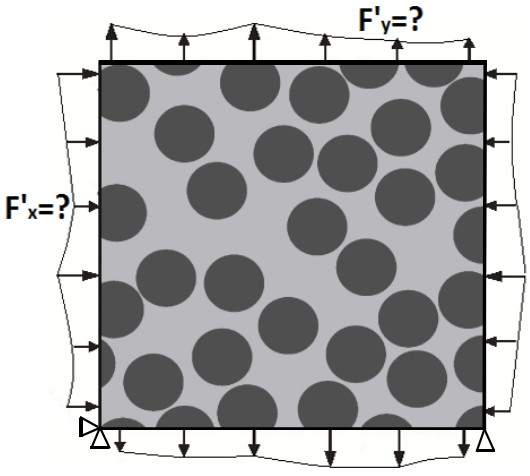

Figure 5.6: Free body diagram of a sample ROI

Fourier basis functions. This algorithm relies on a continuum-based framework that delivers more reliable measurements than subset-based algorithms Mortazavi *et al.* (2011a). The difference between the measured and exact (i.e. that obtained from finite element simulations) strain fields was considered as measurement error. The uncertainty between measured and exact strain fields components was characterized by the standard deviation of measurement error.

For evaluating the performance of the identification methods Gaussian white noise with two different noise levels were added to the input images in different runs *prior* to the displacement measurements. The additive noises were chosen so that two standard deviations of measurement error corresponded to approximately 2% and 10% of the mean strain values. These values corresponded to almost 0.8% and 4%, respectively, in terms of gray levels intensity variations. This procedure of providing input experimental data was favored over previous approaches in which the white noise would be added directly to perfect data so as to add uncertainties to the input displacement function for the identification algorithm. The current approach, indeed, takes into account the inevitable systematic errors caused by the DIC algorithm, which do not necessarily take the form of a white noise with zero mean value. The measured strain fields were subsequently obtained through partial differentiation of the measured displacement data. Figure 5.8 depicts typical exact and measured strain fields ε_1 (perturbed with the noise level of 2%) for composites A and B under biaxial loading. Figure 5.9 also compares the measured and exact strains (ε_1) of an arbitrary path obtained under biaxial loading.

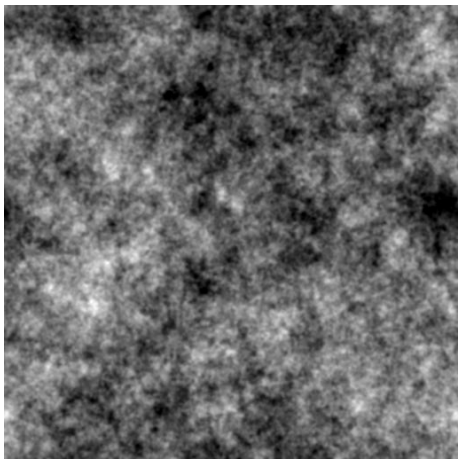

Figure 5.7: Undeformed image generated for full-field measurement

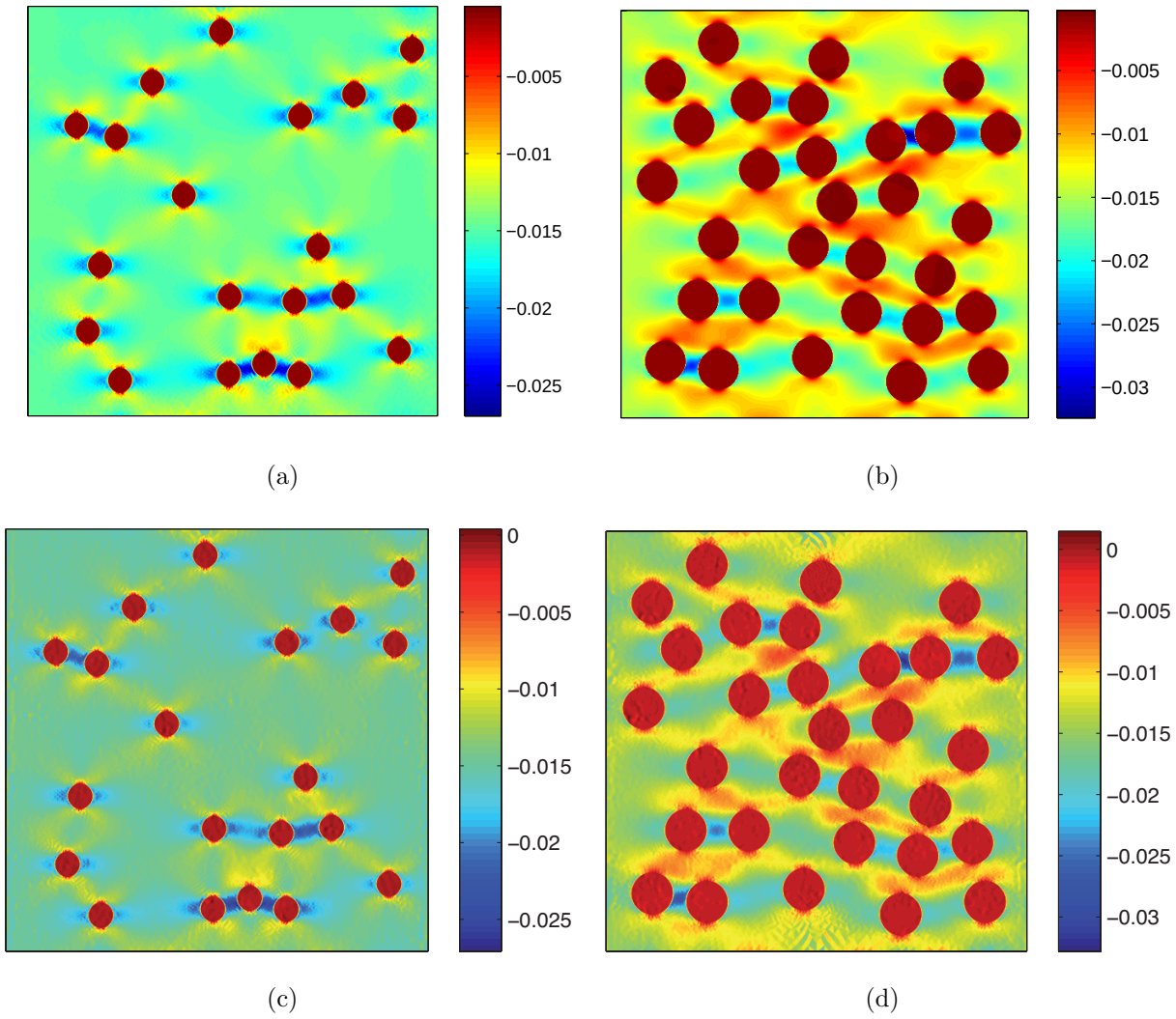

Figure 5.8: Exact (FE) and measured strain fields with noise level 2% obtained under biaxial loading; (a) exact ε_1 in composite A, (b) exact ε_1 in composite B, (c) measured ε_1 in composite A, (d) measured ε_1 in composite B

5.5.4 Parameters identification with VFM and RVFM

Both VFM and RVFM identification methods were applied herein with the aim of retrieving the reference elastic parameters of the composites constituents initially inputted to generate the ”measured” strain fields.

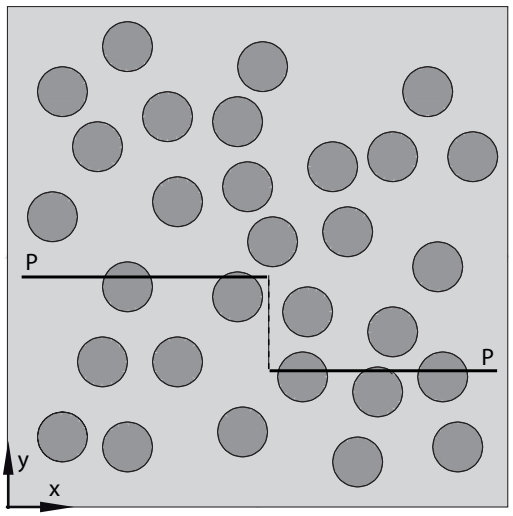

(a)

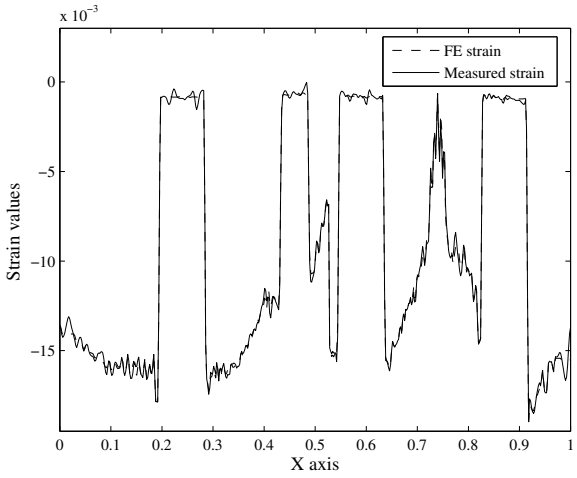

(b)

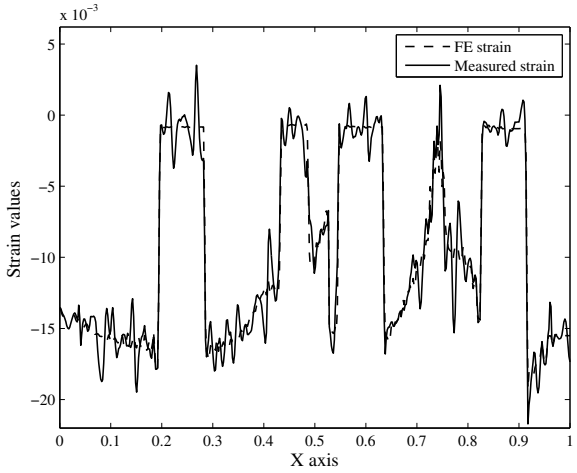

(c)

Figure 5.9: (a) Arbitrary path line over composite B. FE strain data versus measured strains with (b) standard deviation 2% and (c) standard deviation 10% over path line P-P

Developing the VFM algorithms

The constitutive materials associated to the matrix and fibers were assumed to be isotropic. Since the whole material was not homogeneous, the overall surface of composite S was split into $S - S'$ and S', i.e. matrix and fibers subregions, respectively, so as to factorize the unknown parameters. Denoting Q_{xx}, Q_{xy} and Q'_{xx}, Q'_{xy} the stiffness components over $S - S'$ and S', respectively, Eq. 5.5 can be rewritten as:

$$\begin{aligned} Q_{xx} \int\limits_{S-S'} \left(\varepsilon_x\varepsilon_x^* + \varepsilon_y\varepsilon_y^* + \frac{1}{2}\varepsilon_s\varepsilon_s^*\right) \mathrm{d}S + Q_{xy} \int\limits_{S-S'} \left(\varepsilon_x\varepsilon_y^* + \varepsilon_y\varepsilon_x^* - \frac{1}{2}\varepsilon_s\varepsilon_s^*\right) \mathrm{d}S \\ + Q'_{xx} \int\limits_{S'} \left(\varepsilon_x\varepsilon_x^* + \varepsilon_y\varepsilon_y^* + \frac{1}{2}\varepsilon_s\varepsilon_s^*\right) \mathrm{d}S + Q'_{xy} \int\limits_{S'} \left(\varepsilon_x\varepsilon_y^* + \varepsilon_y\varepsilon_x^* - \frac{1}{2}\varepsilon_s\varepsilon_s^*\right) \mathrm{d}S \\ = \int\limits_{L_f} T_i u_i^* \, \mathrm{d}l \quad \forall u^* \in \mathcal{K} \end{aligned} \tag{5.14}$$

Four KA virtual fields independent from each other and compatible with each of the presented boundary conditions had to be chosen. For the biaxial loading condition, where the distribution of loading is known throughout the boundary of the material, the virtual displacements $u^{*(i)}$ (Set 1) and the corresponding strain fields $\varepsilon^{*(i)}$ were defined by:

$$\begin{cases} u_x^{*(1)} = x \\ u_y^{*(1)} = 0 \end{cases} \qquad \begin{cases} \varepsilon_x^{*(1)} = 1 \\ \varepsilon_y^{*(1)} = 0 \\ \varepsilon_s^{*(1)} = 0 \end{cases} \tag{5.15a}$$

$$\begin{cases} u_x^{*(2)} = 0 \\ u_y^{*(2)} = y \end{cases} \qquad \begin{cases} \varepsilon_x^{*(2)} = 0 \\ \varepsilon_y^{*(2)} = 1 \\ \varepsilon_s^{*(2)} = 0 \end{cases} \tag{5.15b}$$

$$\begin{cases} u_x^{*(3)} = \frac{x^2}{2} \\ u_y^{*(3)} = 0 \end{cases} \qquad \begin{cases} \varepsilon_x^{*(3)} = x \\ \varepsilon_y^{*(3)} = 0 \\ \varepsilon_s^{*(3)} = 0 \end{cases} \tag{5.15c}$$

$$\begin{cases} u_x^{*(4)} = 0 \\ u_y^{*(4)} = \frac{y^2}{2} \end{cases} \qquad \begin{cases} \varepsilon_x^{*(4)} = 0 \\ \varepsilon_y^{*(4)} = y \\ \varepsilon_s^{*(4)} = 0 \end{cases} \tag{5.15d}$$

It is clear that all of the virtual displacements above are differentiable and C^0 continuous. From the presented virtual fields, the right-hand part of Eq. 5.14, i.e. the virtual work of the external loading, can be easily determined. As an example, the first component of vector B is obtained with the first virtual displacement fields as

$$\int_{L_f} T_i u_i^* \, \mathrm{d}l = I_r + I_l + I_t + I_b \tag{5.16}$$

where I_r, I_l, I_u and I_d are the virtual work of the applied loads on the right, left, top and bottom border of the composites, respectively (see Figure 5.2). Assuming identical dimensions for the edges in x and y directions ($L_x = L_y = L$) they lead to

$$I_r = \int_0^L (T_x(L,y)\, u_x^* + T_y(L,y)\, u_y^*)\, \mathrm{d}y = \int_0^L F_x L \, \mathrm{d}y = F_x L^2 \tag{5.17a}$$

$$I_l = \int_0^L (T_x(0,y)\, u_x^* + T_y(0,y)\, u_y^*)\, \mathrm{d}y = 0 \tag{5.17b}$$

$$I_t = \int_0^L (T_x(x,L)\, u_x^* + T_y(x,L)\, u_y^*)\, \mathrm{d}x = 0 \tag{5.17c}$$

$$I_b = \int_0^L (T_x(x,0)\, u_x^* + T_y(x,0)\, u_y^*)\, \mathrm{d}x = 0 \tag{5.17d}$$

The following linear system of equations results from Eq. 5.14

$$\begin{bmatrix} \int\limits_{S-S'} \varepsilon_x dS & \int\limits_{S-S'} \varepsilon_y dS & \int\limits_{S'} \varepsilon_x dS & \int\limits_{S'} \varepsilon_y dS \\ \int\limits_{S-S'} \varepsilon_y dS & \int\limits_{S-S'} \varepsilon_x dS & \int\limits_{S'} \varepsilon_y dS & \int\limits_{S'} \varepsilon_x dS \\ \int\limits_{S-S'} x\varepsilon_x dS & \int\limits_{S-S'} x\varepsilon_y dS & \int\limits_{S'} x\varepsilon_x dS & \int\limits_{S'} x\varepsilon_y dS \\ \int\limits_{S-S'} y\varepsilon_y dS & \int\limits_{S-S'} y\varepsilon_x dS & \int\limits_{S'} y\varepsilon_y dS & \int\limits_{S'} y\varepsilon_x dS \end{bmatrix} \begin{Bmatrix} Q_{xx} \\ Q_{xy} \\ Q'_{xx} \\ Q'_{xy} \end{Bmatrix} = \begin{Bmatrix} F_x L^2 \\ F_y L^2 \\ \frac{F_x L^3}{2} \\ \frac{F_y L^3}{2} \end{Bmatrix} \tag{5.18}$$

The integrals were approximated by discrete sums over the available data points (the

strain data over grid points). For instance

$$\int_{S-S'} \varepsilon_x dS \simeq \sum_{i=1}^{p} \varepsilon_x^i s^i \tag{5.19}$$

where p is the number of data points over $(S - S')$ and s^i are their areas.
The effect of virtual fields definition on the identification results was investigated by using different sets of virtual fields:
Set 2:

$$\begin{cases} u_x^{*(1)} = \sin(x) \\ u_y^{*(1)} = 0 \end{cases} \tag{5.20a}$$

$$\begin{cases} u_x^{*(2)} = 0 \\ u_y^{*(2)} = \sin(y) \end{cases} \tag{5.20b}$$

$$\begin{cases} u_x^{*(3)} = \frac{x^2}{2} \\ u_y^{*(3)} = 0 \end{cases} \tag{5.20c}$$

$$\begin{cases} u_x^{*(4)} = 0 \\ u_y^{*(4)} = \frac{y^2}{2} \end{cases} \tag{5.20d}$$

Set 3:

$$\begin{cases} u_x^{*(1)} = \exp(x) \\ u_y^{*(1)} = 0 \end{cases} \tag{5.21a}$$

$$\begin{cases} u_x^{*(2)} = 0 \\ u_y^{*(2)} = \exp(y) \end{cases} \tag{5.21b}$$

$$\begin{cases} u_x^{*(3)} = \frac{x^2}{2} \\ u_y^{*(3)} = 0 \end{cases} \tag{5.21c}$$

$$\begin{cases} u_x^{*(4)} = 0 \\ u_y^{*(4)} = \frac{y^2}{2} \end{cases} \tag{5.21d}$$

Set 4:

$$\begin{cases} u_x^{*(1)} = \sin(x) \\ u_y^{*(1)} = 0 \end{cases} \tag{5.22a}$$

$$\begin{cases} u_x^{*(2)} = 0 \\ u_y^{*(2)} = \sin(y) \end{cases} \tag{5.22b}$$

$$\begin{cases} u_x^{*(3)} = \exp(x) \\ u_y^{*(3)} = 0 \end{cases} \tag{5.22c}$$

$$\begin{cases} u_x^{*(4)} = 0 \\ u_y^{*(4)} = \exp(y) \end{cases} \tag{5.22d}$$

The following set of virtual fields were defined for the uniaxial loading

$$\begin{cases} u_x^{*(1)} = 0 \\ u_y^{*(1)} = y \end{cases} \qquad \begin{cases} \varepsilon_x^{*(1)} = 0 \\ \varepsilon_y^{*(1)} = 1 \\ \varepsilon_s^{*(1)} = 0 \end{cases} \tag{5.23a}$$

$$\begin{cases} u_x^{*(2)} = 0 \\ u_y^{*(2)} = \frac{y^2}{2} \end{cases} \qquad \begin{cases} \varepsilon_x^{*(2)} = 0 \\ \varepsilon_y^{*(2)} = y \\ \varepsilon_s^{*(2)} = 0 \end{cases} \tag{5.23b}$$

$$\begin{cases} u_x^{*(3)} = 0 \\ u_y^{*(3)} = \frac{y^3}{3} \end{cases} \qquad \begin{cases} \varepsilon_x^{*(3)} = 0 \\ \varepsilon_y^{*(3)} = y^2 \\ \varepsilon_s^{*(3)} = 0 \end{cases} \tag{5.23c}$$

$$\begin{cases} u_x^{*(4)} = 0 \\ u_y^{*(4)} = \frac{y^4}{4} \end{cases} \qquad \begin{cases} \varepsilon_x^{*(4)} = 0 \\ \varepsilon_y^{*(4)} = y^3 \\ \varepsilon_s^{*(4)} = 0 \end{cases} \tag{5.23d}$$

In addition to their C^0 continuity, it can be easily checked that the selected virtual displacements are KA. Similar to the previous case, Eq. 5.14 leads to the following linear system

$$\begin{bmatrix} \int\limits_{S-S'} \varepsilon_y dS & \int\limits_{S-S'} \varepsilon_x dS & \int\limits_{S'} \varepsilon_y dS & \int\limits_{S'} \varepsilon_x dS \\ \int\limits_{S-S'} y\varepsilon_y dS & \int\limits_{S-S'} y\varepsilon_x dS & \int\limits_{S'} y\varepsilon_y dS & \int\limits_{S'} y\varepsilon_x dS \\ \int\limits_{S-S'} y^2\varepsilon_y dS & \int\limits_{S-S'} y^2\varepsilon_x dS & \int\limits_{S'} y^2\varepsilon_y dS & \int\limits_{S'} y^2\varepsilon_x dS \\ \int\limits_{S-S'} y^3\varepsilon_y dS & \int\limits_{S-S'} y^3\varepsilon_x dS & \int\limits_{S'} y^3\varepsilon_y dS & \int\limits_{S'} y^3\varepsilon_x dS \end{bmatrix} \begin{Bmatrix} Q_{xx} \\ Q_{xy} \\ Q'_{xx} \\ Q'_{xy} \end{Bmatrix} = \begin{Bmatrix} F_y L^2 \\ \frac{F_y L^3}{2} \\ \frac{F_y L^4}{3} \\ \frac{F_y L^5}{4} \end{Bmatrix} \tag{5.24}$$

The linear systems indicated in Eq. 5.18 and Eq. 5.24 were solved through matrix inversion (i.e. classical form of VFM, not requiring an initial guess for the stiffness components) as well as using a constrained optimization procedures (RVFM) in order to determine the stiffness components.

The same virtual displacement fields as those defined in Eq. 5.15 were used for small ROIs. It can be deduced that the chosen virtual fields are KA with respect to the imposed boundary conditions.

The elastic mechanical properties of the constitutive phases are directly related to the sought stiffness components by the following relations

$$\begin{aligned} \nu_m &= \frac{Q_{xy}}{Q_{xx}}, \quad E_m = Q_{xx}(1-\nu_m^2) \\ \nu_f &= \frac{Q'_{xy}}{Q'_{xx}}, \quad E_f = Q'_{xx}(1-\nu_f^2) \end{aligned} \tag{5.25}$$

Effective properties calculation from the RVE

The regularization constraints presented in Eq. 5.11 require the composite's effective properties. The effective properties were computed with 3D finite element models of composites, where the fibers were aligned with z. Uniform compressive displacements were applied to the surfaces having their normals aligned with z and all the other surfaces were free of stresses. The RVE was computed according to the methodology of Kanit et al. (Kanit *et al.*, 2003). The methodology consists first of generating numerous random volume elements containing fixed numbers of represented reinforcements (e.g., 10 different realizations containing 5 fibers, 8 realizations containing 10 fibers, etc.). Then, the effective properties are computed for each realization and averaged for the realizations containing the same number of represented reinforcements. The RVE is reached when the averaged properties do not vary, according to a prescribed threshold, when the number of represented reinforcement is increased. The following lines detail the specific criteria and procedures used in this study.
The effective properties for each realization were computed according to the following procedure. First, define $\langle f \rangle$ as:

$$\begin{aligned} \langle f \rangle &= \frac{1}{V} \int_V f(\boldsymbol{x}) \mathrm{d}V \\ &\approx \frac{1}{V} \sum_{i=1}^{q} f^{(i)} \Delta V_i \end{aligned} \tag{5.26}$$

where $\langle \cdot \rangle$ represents volume averaging, $\boldsymbol{x}$ is a point in 3D space, $f^{(i)}$ and ΔV_i are the value of f at a given integration point (i) and the volume of that integration point, respectively, q is the total number of integration points in the model. At each realization, $\langle \sigma_{xx} \rangle \approx \langle \sigma_{yy} \rangle \approx 0$ and the values of $\langle \sigma_{zz} \rangle$ and $\langle \varepsilon_{xx} \rangle$ were obtained from Eq. 5.26. Therefore, the effective properties can be deduced from:

$$\begin{Bmatrix} \langle \varepsilon_{xx} \rangle \\ \langle \varepsilon_{zz} \rangle \end{Bmatrix} = \begin{bmatrix} \frac{1}{\hat{E}_t} & -\frac{\hat{\nu_{lt}}}{\hat{E}_l} \\ -\frac{\hat{\nu_{tl}}}{\hat{E}_t} & \frac{1}{\hat{E}_l} \end{bmatrix} \begin{Bmatrix} \langle \sigma_{xx} \rangle \\ \langle \sigma_{zz} \rangle \end{Bmatrix} \tag{5.27}$$

where $\hat{E}$ and $\hat{\nu}$ are the effective elastic modulus and Poisson's ratio of the composite, respectively, and subscripts l and t indicate the out-of-plane (i.e. z direction) and in-plane (i.e xy plane), respectively. Since $\langle \sigma_{xx} \rangle = 0$, $\hat{E_l}$ and $\hat{\nu_{lt}}$, were directly obtained from Eq. 5.27.
The size of RVE was determined by gradually increasing of the number of fibers in the volume, while preserving their volume fraction. For a given number of represented fibers, 6

realizations were performed and two-tailed 95% confidence intervals were computed for the average property. The same procedure was repeated for increasing numbers of represented fibers, that ranged from 90 to 170. The RVE was reached when the average effective property did not vary with the number of represented fibres, within a tolerance. For all simulations, 6 realizations led to confidence intervals whose widths were smaller than 1% of the average value. The convergence study was accomplished only for the composite containing the largest volume fraction and the highest contrast of properties (i.e. composite C'). The same size of RVE was then considered for the other composites with lower volume fractions and contrast of properties. Figure 5.10 shows, for example, the convergence trend for the values of elastic modulus ($\hat{E}_l$) in composite C'. As it can be seen, a simulated model consisting of 150 fibers can be considered as a RVE.

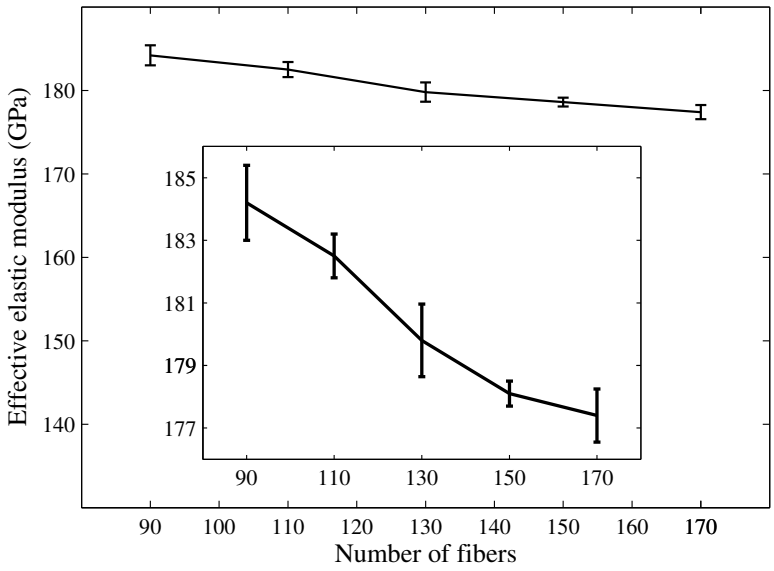

Figure 5.10: Variation of effective elastic modulus of composite C' and the related confidence intervals

RVFM optimization problem

The least square objective functions for each problem was developed based on Eq. 5.10 using the four equations of linear systems (Eq. 5.18 and Eq. 5.24). Hence, the RVFM

consisted of solving the following optimization problem

$$\min \;\; r(\mathbf{q}) = (\boldsymbol{A} \cdot \mathbf{q} - \mathbf{b})^T \cdot (\boldsymbol{A} \cdot \mathbf{q} - \mathbf{b}) \tag{5.28}$$

subjected to

$$\mid \widetilde{E_l^{MT}}(\mathbf{q}) - \hat{E}_l \mid \leq \delta_1 \tag{5.29a}$$

$$\mid \widetilde{\nu_{lt}^{MT}}(\mathbf{q}) - \hat{\nu_{lt}} \mid \leq \delta_2 \tag{5.29b}$$

where the terms with superscript MT refers to the properties predicted from the Mori-Tanaka homogenization model and δ_1 and δ_2 were set to 1% of the corresponding effective properties i.e. $\hat{E}_l$ and $\hat{\nu_{lt}}$, respectively.

In this study, the MADS optimization method (Audet et Dennis Jr., 2006) was used to solve the above mentioned constrained optimization problem. For each RVFM identification, the stiffness components obtained from VFM were considered as initial solution at the beginning of the optimization process [1]. At each iteration, the numerical values of the constraints were evaluated by substituting new material parameters into the Mori-Tanaka model, and the feasibility of trial points was assessed by the regularization constraints.

The whole algorithm involved a blackbox that consisted of a main Matlab code and several subroutines associated to the Mori-Tanaka homogenization model. The stopping criterion for the MADS algorithm was reached when a maximum number of 300 objective function evaluations were performed.

5.5.5 Parameters identification with VFM/Mori-Tanaka algorithm

It was found that the matrix properties obtained from the VFM were more accurate than the fiber properties. This comes from the fact that the fibers deform significantly less than the matrix and the signal/noise ratio in the fibers is much less than that in the matrix. Therefore, an alternative identification technique was to keep constant the matrix parameters obtained by the VFM and determine only the fibers parameters directly from Mori-Tanaka homogenization model. The performance of this VFM/Mori-Tanaka technique is also discussed in the following section.

1. In the MADS optimization method, the initial solution does not need to satisfy the constraints. In fact, the applied constraints controls the feasibility of the solutions within the variables space (see (Le Digabel, 2011) for more information)

5.6 Results and discussions

5.6.1 Identified parameters from uniform boundary conditions

Table 5.3 shows The identification results for composite A using different sets of virtual fields for a noise level of 2%. The results show that the accuracy of the method is quite sensitive to the choice of virtual fields. This is in agreement with the experience of Pierron et. al. (Pierron et Grédiac, 2012) who observed that simple low order virtual fields are usually suitable choices for linearly isotropic behavior of materials.

Tables 5.4a to 5.4d present the mechanical properties of different composites identified

Table 5.3: The identification results for composite A using different sets of virtual fields in noise level 2%

Virtual fields	$E_f(GPa)$	ν_f	$E_m(GPa)$	ν_m
Target values	74	0.2	3.5	0.35
Set 1	69.00	0.219	3.45	0.350
Set 2	63.82	0.242	3.39	0.336
Set 3	238.8	1.00	18.6	0.992
Set 4	98.12	0.676	1.13	0.614

from the bi-axial loading condition. The results of VFM and RVFM were compared to those of the RMU and FEMU methodologies obtained in (Rahmani *et al.*, 2013a). The relative error for each parameter for different noise levels are also presented in the tables. The VFM results in a relatively accurate set of parameters except for the Poisson's ratio of the fibers, in some cases. It can also be seen that the matrix parameters obtained from the VFM are only slightly affected by the noise level. The fibers properties are more sensitive to noise and by increasing the noise level the corresponding relative errors of the identified fibers parameters increase. This phenomenon is more pronounced for the cases with higher contrast of elastic modulus, i.e. composites A' and B' (Table 5.4b and Table 5.4d). This is mostly due to the accuracy loss in the DIC algorithm when trying to capture important displacement gradients typically encountered in highly contrasted materials. In addition, the strain data in the fiber phase possess much less signal/noise ratio. The signal/noise ratios (i.e. the ratio of mean strain value to the standard deviation of noise) for the constituent phases of different composites are presented in Table 5.5. In contrast, thanks to the regularization effects, the RVFM did not suffer from such problems and the obtained parameters are much more accurate.

Table 5.4a: The identified parameters for composite A in various noise levels (bi-axial loading)

Method	Noise level	$E_f(GPa)$ $(error\%)$	ν_f $(error\%)$	$E_m(GPa)$ $(error\%)$	ν_m $(error\%)$	App. calc. time (min)
Target properties	–	74	0.2	3.5	0.35	–
VFM	FE data	75.90 (2.6%)	0.223 (11.5%)	3.49 (0.3%)	0.350 (0%)	-
RVFM	FE data	71.62 (3.2%)	0.185 (7.5%)	3.47 (0.9%)	0.352 (0.6%)	25
VFM	2%	69.00 (6.7%)	0.219 (9.5%)	3.45 (1.4%)	0.350 (0%)	-
RVFM	2%	72.01 (2.7%)	0.193 (3.5%)	3.43 (2%)	0.351 (0.3%)	25
VFM	10%	82.30 (11.2%)	0.125 (38%)	3.40 (2.8%)	0.360 (2.8%)	-
RVFM	10%	72.18 (2.4%)	0.208 (4%)	3.43 (2%)	0.350 (0%)	25
FEMU	10%	86.08 (16.3%)	0.350 (75%)	3.71 (6%)	0.340 (2.8%)	280
RMU	10%	75.82 (2.5%)	0.219 (9.5%)	3.49 (0.3%)	0.349 (0.28%)	280

Table 5.4b: The identified parameters for composite A' in various noise levels (bi-axial loading)

Method	Noise level	$E_f(GPa)$ $(error\%)$	ν_f $(error\%)$	$E_m(GPa)$ $(error\%)$	ν_m $(error\%)$	App. calc. time (min)
Target properties	–	350	0.2	3.5	0.35	–
VFM	FE data	332.1 (5%)	0.197 (1.5%)	3.47 (0.9%)	0.351 (0.3%)	-
RVFM	FE data	342.9 (2%)	0.173 (13.5%)	3.56 (1.7%)	0.353 (0.9%)	25
VFM	2%	310.0 (11.5%)	0.165 (17.5%)	3.48 (0.6%)	0.349 (0.3%)	-
RVFM	2%	350.1 (0%)	0.235 (17.5%)	3.55 (1.4%)	0.347 (0.85%)	25
VFM	10%	221.6 (36.7%)	0.342 (71%)	3.40 (2.8%)	0.336 (4%)	-
RVFM	10%	347.5 (0.7%)	0.255 (27.5%)	3.45 (1.4%)	0.343 (2%)	25
FEMU	10%	471.3 (34.66%)	0.451 (125%)	3.87 (10.7%)	0.369 (5.4%)	280
RMU	10%	343.5 (1.8%)	0.221 (10.5%)	3.52 (0.6%)	0.350 (0%)	280

Table 5.4c: The identified parameters for composite B in various noise levels (bi-axial loading)

Method	Noise level	$E_f(GPa)$ $(error\%)$	ν_f $(error\%)$	$E_m(GPa)$ $(error\%)$	ν_m $(error\%)$	App. calc. time (min)
Target properties	–	74	0.2	3.5	0.35	–
VFM	FE data	73.60 (0.5%)	0.198 (1%)	3.50 (0%)	0.351 (0.3%)	-
RVFM	FE data	73.89 (0.17%)	0.223 (11.5%)	3.50 (0%)	0.343 (2%)	25
VFM	2%	66.20 (10.5%)	0.193 (3.5%)	3.54 (1.1%)	0.356 (1.7%)	-
RVFM	2%	72.11 (2.5%)	0.212 (6%)	3.41 (2.6%)	0.342 (2.2%)	25
VFM	10%	61.82 (16.5%)	0.238 (19%)	3.55 (1.4%)	0.340 (2.9%)	-
RVFM	10%	71.90 (2.8%)	0.220 (10%)	3.55 (1.4%)	0.340 (2.9%)	25
FEMU	10%	101.2 (36.7%)	0.450 (125%)	3.26 (6.8%)	0.333 (4.8%)	280
RMU	10%	71.29 (3.6%)	0.184 (8%)	3.57 (1.8%)	0.344 (1.7%)	280

Table 5.4d: The identified parameters for composite B' in various noise levels (bi-axial loading)

Method	Noise level	$E_f(GPa)$ $(error\%)$	ν_f $(error\%)$	$E_m(GPa)$ $(error\%)$	ν_m $(error\%)$	App. calc. time (min)
Target properties	–	350	0.2	3.5	0.35	–
VFM	FE data	334.2 (4.5%)	0.225 (12.5%)	3.44 (1.7%)	0.344 (1.7%)	-
RVFM	FE data	338.3 (3.4%)	0.224 (12%)	3.39 (3.1%)	0.345 (1.4%)	25
VFM	2%	300.0 (14.2%)	0.235 (17.5%)	3.24 (7.5%)	0.346 (1.1%)	-
RVFM	2%	337.4 (3.5%)	0.226 (13%)	3.27 (6.5%)	0.343 (2%)	25
VFM	10%	224.8 (35.7%)	0.176 (12%)	3.43 (2%)	0.370 (6%)	-
RVFM	10%	341.2 (2.5%)	0.167 (16.5%)	3.42 (2.2%)	0.362 (3.4%)	25
FEMU	10%	437.2 (24.9%)	0.331 (65.5%)	3.34 (4.4%)	0.338 (3.42%)	280
RMU	10%	335.2 (4.2%)	0.183 (8.5%)	3.62 (3.4%)	0.344 (1.7%)	280

It should be noted that in some cases the RVFM may not enhance the accuracy of the matrix parameters meaningfully, or even degrade them slightly. This degradation is however negligible. This phenomena is most certainly attributed to the fact that the accuracy of the MT model decreases with increasing volume fractions and contrasts (Ghossein et Lévesque, 2012). Moreover, in spite of very good enhancements in the accuracy of the identified Poisson's ratio of fibers, this parameter might not to be as accurate as the other parameters. The first reason for this higher uncertainty is lower signal/noise ratio in the fiber phase, mentioned above. The second might be associated to lower sensitivity of the effective properties predicted by Mori-Tanaka model to the variations in this parameter than the other parameters. Figure 5.11 compares the sensitivity of the effective properties to the variation of different parameters of constituent phases for composite B. As it can be observed, the Poisson's ratio of fibers has very slight effect (approximately no effect) on the effective elastic modulus and its influence on the effective Poisson's ratio is much less than that of the Poisson's ratio of matrix.

For the noise level of 10%, the resulting parameters from both procedures were compared with those obtained from the FEMU and the RMU methods. Their approximate calculation time are also compared in the tables. It can be seen that the VFM is generally less sensitive to noise effects than the FEMU method and leads to more accurate solutions. Also, the RMU method is only slightly affected by noise effects and yields solutions with much lower uncertainties when compared with the FEMU method. It can also be observed that the RVFM and RMU methodologies lead to approximately the same accuracies. However, the most significant advantage of the RVFM is that it delivers results in a tenth of the computational time of the RMU method. The RVFM is therefore a robust, as well as time-efficient identification method.

Tables 5.6a and 5.6b show the identified parameters for composites B and B' resulting from various identification methods under the uniaxial loading condition. Conclusions similar to

Table 5.5: Signal/noise ratio for constituent phases of different composites (noise level 10%)

Composite	fibers	matrix
A	1.21	12.6
A'	0.25	11.8
B	1.16	15.4
B'	0.36	15.5

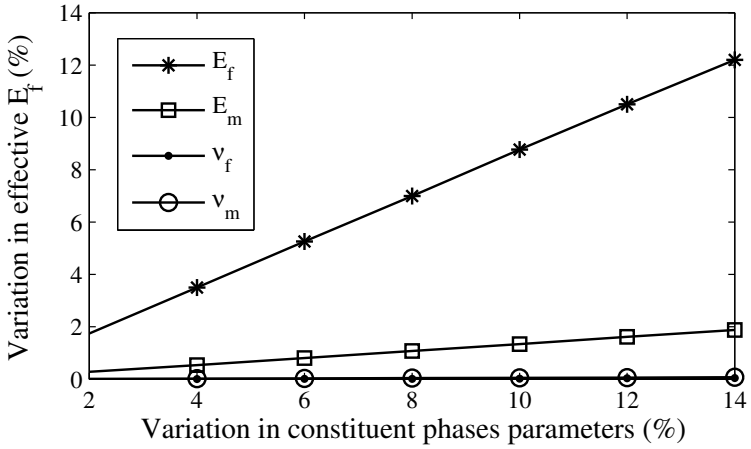

(a)

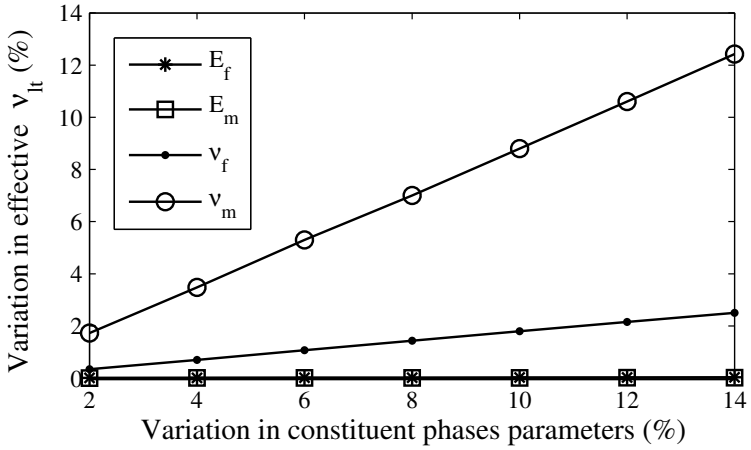

(b)

Figure 5.11: Sensitivity of effective parameters predicted by the Mori-Tanaka model to the variations in different parameters of constituent phases; (a) effective elastic modulus (b) effective Poisson's ratio

those obtained from the bi-axial loading can be drawn.

Table 5.6a: The identified parameters for composite B in various noise levels (uniaxial loading)

Method	Noise level	$E_f(GPa)$ $(error\%)$	ν_f $(error\%)$	$E_m(GPa)$ $(error\%)$	ν_m $(error\%)$	App. calc. time (min)
Target properties	–	74	0.2	3.5	0.35	–
VFM	FE data	73.15 (1.1%)	0.200 (0%)	3.50 (0%)	0.351 (0.3%)	-
RVFM	FE data	73.90 (0.1%)	0.180 (10%)	3.48 (0.6%)	0.352 (0.6%)	25
VFM	2%	68.28 (5.8%)	0.179 (10.5%)	3.46 (1.1%)	0.357 (2%)	-
RVFM	2%	71.86 (2.9%)	0.214 (7%)	3.43 (2%)	0.345 (1.4%)	25
VFM	10%	58.83 (21.8%)	0.272 (36%)	3.51 (0.3%)	0.338 (3.5%)	-
RVFM	10%	71.74 (3%)	0.227 (13.5%)	3.45 (1.4%)	0.340 (2.8%)	25
FEMU	10%	111.9 (51.3%)	0.335 (67.5%)	3.26 (6.9%)	0.340 (2.6%)	280
RMU	10%	75.05 (1.3%)	0.182 (9%)	3.49 (0%)	0.353 (0.85%)	280

Table 5.6b: The identified parameters for composite B' in various noise levels (uniaxial loading)

Method	Noise level	$E_f(GPa)$ $(error\%)$	ν_f $(error\%)$	$E_m(GPa)$ $(error\%)$	ν_m $(error\%)$	App. calc. time (min)
Target properties	–	350	0.2	3.5	0.35	–
VFM	FE data	338.8 (3.2%)	0.205 (2.5%)	3.48 (0.6%)	0.351 (0.3%)	-
RVFM	FE data	337.4 (3.5%)	0.206 (3%)	3.43 (2%)	0.349 (0.28%)	25
VFM	2%	222.7 (36.5%)	0.219 (9.5%)	3.61 (3%)	0.345 (1.4%)	-
RVFM	2%	340.5 (2.7%)	0.210 (5%)	3.43 (2%)	0.346 (1.1%)	25
VFM	10%	216 (38.3%)	0.248 (24%)	3.65 (4.3%)	0.358 (2.2%)	-
RVFM	10%	338.6 (3.2%)	0.180 (10%)	3.41 (2.5%)	0.354 (1.1%)	25
FEMU	10%	231.4 (34%)	0.140 (30%)	3.68 (5.1%)	0.357 (2%)	280
RMU	10%	341.3 (2.5%)	0.216 (8%)	3.47 (0.85%)	0.356 (1.7%)	280

Figure 5.12 also compares the overall relative error of the identified parameters resulting from all tested composites, using four identification methods in the maximum level of noise. It can be observed that the FEMU is the less accurate method for both contrasts of elastic modulus ($C = 21$ and $C = 100$). The error values associated to the constrained identification methods are significantly lower than those of the unconstrained methods.

5.6.2 Influence of the small regions of interest

The mechanical parameters for the composites having the highest volume fraction of fibers were obtained with ROI size of 1×1 (see Figure 5.4(b)), under biaxial loading. Three different ROIs, including various distributions of fibers in the matrix were investigated and the average relative error of identified parameters were calculated. Table 5.7a presents the obtained results for composites C using both VFM and RVFM.

Strains directly obtained from the FE data and those computed from the DIC algorithm with 10% noise were studied. The average error of estimated overall stresses on the boundary of ROIs (used for both identification methods) has also been reported in the table. It can be seen that the average overall stress is very close to that of the whole sample. This comes

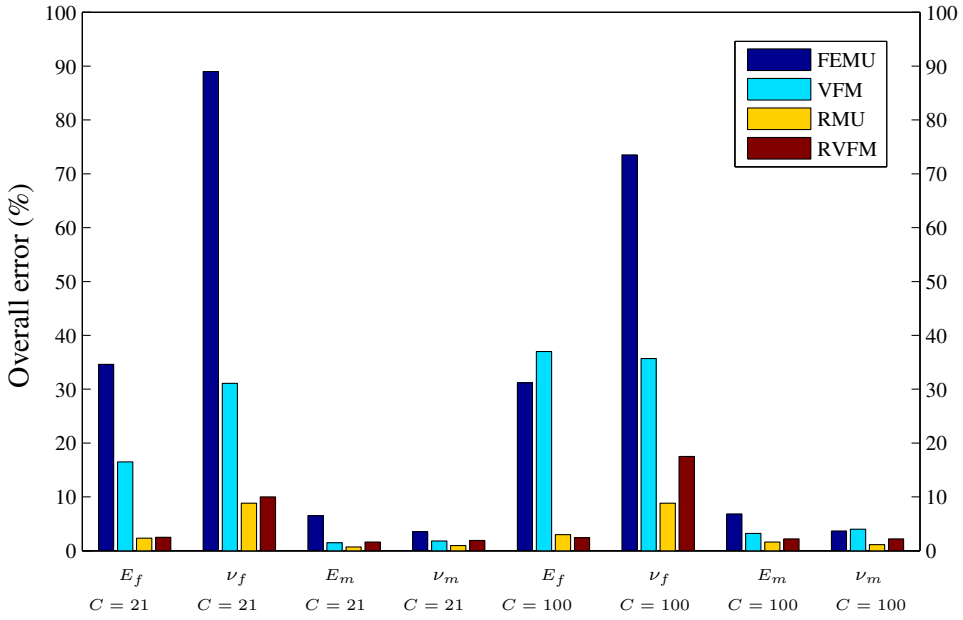

Figure 5.12: Overall errors of the identified parameters for all tested composites, resulting from different identification methods in the maximum noise level

Table 5.7a: Average relative error of the identified parameters of composite C (ROI 1×1)

Method	Noise level	E_f *error*	ν_f *error*	E_m *error*	ν_m *error*	Average stress error
VFM	FE data	2.6%	4.8%	5.5%	3.5%	σ_x : 1%
VFM	10%	10.4%	27%	12.7%	19.2%	σ_y : 1.4%
RVFM	10%	1.1%	12.8%	3.8%	6.6%	

from the fact that this size of ROI was large enough and the approximate number of fibers represented in this model was larger than that of the RVE size. In contrast to the cases with lower volume fractions, the VFM identification results in lower accuracy for the matrix properties. This might be due the strain concentrations found in the matrix phase between neighboring fibers. For both methods, the accuracy of all parameters was degraded in the presence of noise. Despite its superiority with respect to the other identification strategies, the accuracy of the RVFM was lower in comparison with cases of lower volume fractions. Again, this is mostly due to the accuracy deterioration of the Mori-Tanaka model for higher volume fractions and properties contrasts.

Table 5.7b shows the average relative error of the identified parameters of composite C related to ROI size 0.5×0.5 obtained from six various regions (different distribution of fibers in the matrix). The corresponding average error of the overall stresses with respect to the exact applied stresses are also provided. The average stresses over this size of ROI are very close to those applied on the boundary of the composite itself. The accuracy of the identified parameters through both VFM and RVFM methods are almost the same as those acquired in ROI 1×1.

The results are considerably different for smaller ROIs (i.e. 0.25x0.25 and 0.1x0.1). This is because they are not large enough to be a RVE and therefore the estimated overall stresses are less accurate, as indicated in Tables 5.7c and 5.7d.

As a matter of fact, the effective tractions on the small ROIs are significantly different

Table 5.7b: Average relative error of the identified parameters of composite C (ROI 0.5×0.5)

Method	Noise level	E_f *error*	ν_f *error*	E_m *error*	ν_m *error*	Average stress error
VFM	FE data	1.6%	14.7%	4.5%	3.9%	σ_x : 1.7%
VFM	10%	7.6%	21.6%	10%	20.4%	σ_y : 1.6%
RVFM	10%	1.6%	13.3%	3.1%	5.6%	

Table 5.7c: Average relative error of the identified parameters of composite C (ROI 0.25×0.25)

Method	Noise level	E_f *error*	ν_f *error*	E_m *error*	ν_m *error*	Average stress error
VFM	FE data	5.6%	9.9%	6.1%	31.9%	σ_x : 2.2%
VFM	10%	11.6%	43.7%	11.6%	21.9%	σ_y : 7.3%
RVFM	10%	2.3%	25.9%	14.3%	12.1%	

Table 5.7d: Average relative error of the identified parameters of composite C (ROI 0.1×0.1)

Method	Noise level	E_f *error*	ν_f *error*	E_m *error*	ν_m *error*	Average stress error
VFM	FE data	19.4%	17.6%	13.1%	35.6%	σ_x : 10%
VFM	10%	20.6%	37.3%	21%	33.1%	σ_y : 9.7%
RVFM	10%	1.8%	35.9%	14%	19.2%	

from those supposed and this is clearly the only source of error when comparing with the larger ROIs. Hence, since the accuracy of VFM depends directly on the accuracy of traction on the boundaries, the accuracy of the parameters identified by smaller ROIs are degraded. Although the RVFM provides results of better accuracy than the other methods, they are not as accurate as those of larger ROIs. This is most likely a direct consequence of the fact that the overall stress on these smaller ROIs are different than that applied on the overall material.

Considering the fact that images with higher magnifications (smaller ROI) enable better discrimination of constitutive phases in DIC methods, and taking into account the VFM limitations shown above, it can be deduced that ROI 0.5×0.5 is the optimum ROI size.

A RVE study was conducted for composite C, through the same procedure presented in section 5.5.4. Table 5.8 shows the number of represented fibers for different ROI sizes, as well as that for reaching the minimum RVE. It can be seen that the ROI 0.5×0.5

Table 5.8: Number of fibers in different ROIs

ROI size	0.1×0.1	0.25×0.25	0.5×0.5	1×1	RVE
Number of fibers	5	28	115	410	110

corresponds to the minimum RVE size and was also the smallest ROI studied that delivered acceptable results. Although the ROI 1×1 is a RVE, it might not be of optimal size for DIC applications due to the important strain gradients encountered in in-situ testing and the limited number of pixels to capture them. It is interesting to recall that the minimum size of the RVE for a given composite can be numerically determined by performing sufficient number of realizations (Kanit *et al.*, 2003). With that mind, the optimum size of the ROI can be estimated, a priori, from the following relation

$$L_{opt} = \left(\frac{N_{RVE} \pi {d_f}^2}{4c} \right)^{\frac{1}{2}} \tag{5.30}$$

where L_{opt} is the edge length of an optimum square ROI, N_{RVE} is the size of RVE (i.e. number of fibers in RVE), d_f is fibers diameter and c denotes fibers volume fraction. This relationship could be useful for guiding the experimentalists in defining the optimum size of their ROIs for accurate properties identification of composites with any mechanical or morphological characteristics.

5.6.3 Identified parameters from VFM/Mori-Tanaka strategy

Table 5.9 list the acquired parameters of composite C with VFM/Mori-Tanaka technique from noisy measured strain fields. The obtained results were compared to RVFM identification solutions. In this strategy, since the matrix parameters were not updated, the accuracy of these parameters were not expected to be improved. Furthermore, since these parameters had previously been affected by noisy data, they created undesirable biases when identifying the fibers parameters from Mori-Tanaka model, and finally leads to inaccurate fibers parameters (especially the Poisson's ratio).

Table 5.9: The identified parameters for composite C by VFM/Mori-Tanaka technique

Method	Noise level	$E_f(GPa)$ ($\epsilon\%$)	ν_f ($\epsilon\%$)	$E_m(GPa)$ ($\epsilon\%$)	ν_m ($\epsilon\%$)
Target properties	–	74	0.2	3.5	0.35
VFM	10%	65.28 (12%)	0.120 (40%)	3.96 (13%)	0.420 (20%)
VFM/Mori-Tanaka	10%	70.95 (4.1%)	0.136 (32%)	3.96 (13%)	0.420 (20%)
RVFM	10%	73.71 (0.4%)	0.193 (3.5%)	3.39 (3.1%)	0.363 (3.7%)

5.7 Conclusions

A new Regularized Virtual Field Method (RVFM) has been developed with the aim of improving constitutive parameters identification for composites in terms of accuracy and computation time. The novelty of the approach is that the VFM system of equations is solved in an optimization framework so that a set of mechanical constraints consisting of a micro-mechanical model are included as regularization scheme.

The efficiency of the method was compared to that of VFM as well as finite element based methods in the presence of noisy measured data and for composites with different volume fractions and mechanical properties contrasts. The results show that the RVFM is the most accurate method tested in this paper and runs in a much shorter time than finite element based methods. Matrix properties were accurately captured whereas fibers properties were generally less accurate, especially for the Poisson's ratio. This is mostly due to the fact that fibers, being much stiffer than the matrix, exhibit much lower strains and hence have a lower signal/noise ratio than the matrix for the sake of the strain measurements.

The effect of ROI size on the corresponding overall stresses was also investigated. For cases smaller than RVE, the error of the overall stresses on the boundary of ROI increases by decreasing the ROI size and leads to less accurate identified parameters. Due to the biases created by inaccurate overall stresses, the RVFM might also result in inappropriate parameters. An optimum ROI size was determined by taking into account the magnification requirements for DIC and the accuracy of the estimated overall stresses over ROIs. This kind of study could be very helpful for estimating, a priori, the required resolution for SEM cameras, as well as the acceptable noise level, for obtaining properties within a certain range of accuracy.

The study also revealed that using the VFM for obtaining the matrix properties and then the Mori-Tanaka model for computing the fibers properties can lead to erroneous results. This demonstrates the need for adding regularization terms in the identification procedure. Future work will deal with the application of the method to 3D particulate composites.

CHAPTER 6

ARTICLE 3: In-situ Mechanical Properties Identification of 3D Particulate Composites using the Virtual Fields Method

B. Rahmani, E. Ghossein, I. Villemure, M. Levesque (2014). The manuscript was submitted to the "International Journal of solid and Structures" on March 4, 2014.

6.1 Abstract

This paper presents an identification procedure based on the Virtual Fields Method (VFM) for identifying in-situ mechanical properties of composite materials constitutive phases from 3D full-field measurements. The new procedure, called the Regularized Virtual Fields Method (RVFM), improves the accuracy of the VFM thanks to the imposition of mechanical constraints derived from an appropriate homogenization model. The developed algorithms were validated through virtual experiments on particulate composites. The robustness of both the VFM and the RVFM was assessed in the presence of noisy strain data for various microstructures. A study was also carried out to investigate the influence of the size of region of interests on the reliability of the identified parameters. Accordingly, the optimum size of region of interest was determined based on full-field measurement requirements and accuracy of the identified parameters. This study enables determining, a priori, the required magnification level of 3D images for composites of any mechanical and morphological characteristics.

6.2 Introduction

Recent studies reveal that in-situ mechanical properties of composites constituting phases can be significantly different than those obtained from conventional testing on bulk samples (Gregory et Spearing, 2005; Hardiman *et al.*, 2012). Such differences can be attributed to different curing kinetics, different chemical reactions, etc. Reliable in-situ mechanical properties are the key for accurate predictions of damage evolution from micromechanical modelling (Koyanagi *et al.*, 2009; Wright *et al.*, 2010).

Recent advances in imaging technologies, like micro-computed tomography (μCT) (Bay *et al.*, 1999a; Martyniuk *et al.*, 2013), enable the non-destructive observation of internal deformation mechanisms in composites and metals. When coupled with a loading system and efficient

Digital Volume Correlation (DVC) algorithms (Mortazavi *et al.*, 2014; Bay *et al.*, 1999a; Franck *et al.*, 2007), such technologies pave the way for the accurate in-situ characterization of local constituents through inverse identification methods.

Several inverse mechanical properties identification methods can be found in the literature (Avril *et al.*, 2008a). Albocher et. al. (Albocher *et al.*, 2009) exploited the Adjoint-Weighted Equation (AWE) method as a direct solution of inverse methods to reconstruct the distribution of unknown properties from full-field displacement data. Different procedures relying on constitutive theories formulations have also been developed for local properties identification. For instance, the Equilibrium Gap Method (EGM) (Claire *et al.*, 2002) and the equation error method (Gockenbach *et al.*, 2008) minimize discrepancies in the equilibrium equation, while the Constitutive Equation Gap Method (CEGM) (Moussawi *et al.*, 2013) minimizes the difference between a given stress distribution and its counterpart computed through a constitutive model. Although these methods allow local characterization of materials, inverse identification methods based on updating finite element models have been the most extensively exploited, owing to their simplicity and flexibility (Okada *et al.*, 1999; Kajberg et Lindkvist, 2004; Gras *et al.*, 2013). These methods, known as Finite Element Model Updating (FEMU), update iteratively the material parameters input into a representative finite element model to achieve the best possible match between numerically predicted fields and their experimentally measured counterparts. The main drawback of these methods is their potentially prohibitive computational cost, especially when dealing with three-dimensional (3D) problems (Kajberg et Lindkvist, 2004).

As an alternative strategy, the Virtual Fields Method (VFM) (Pierron et Grédiac, 2012) enables the direct (i.e. non-iterative) identification of parameters. In this approach, the global equilibrium of a body is expressed through the principle of virtual work in which stress fields are derived as a function of unknown parameters and full-field strains. Mechanical parameters are obtained by solving a linear system of equations once virtual fields (i.e. test functions) have been appropriately defined. The VFM, introduced first by Grédiac (Grédiac, 1989), was originally developed to identify the elastic properties of materials. It has been successfully applied to identify bending and in-plane properties of composites (Grédiac *et al.*, 2002a; Avril et Pierron, 2007; Grédiac, 1996; Grédiac *et al.*, 2003; Pierron *et al.*, 2007; Grédiac *et al.*, 2002c). Efforts have also been made to identify the orthotropic stiffness of laminated composites (Pierron *et al.*, 2000b). The method is known to be less sensitive to measurement uncertainties and noise, when compared to other identification techniques such as FEMU, EGM and CEGM (Avril et Pierron, 2007).

Regularization constraints can be added for stabilizing the identification problem. Different

regularization strategies such as those relying on constitutive relation error (Florentin et Lubineau, 2010) and Tikhonov regularization (Oberai *et al.*, 2004) have already been studied in the literature. The former introduced a statistically admissible stress space in order to restrict the solution space when minimizing constitutive relation error. In the latter, regularization constraints were defined to penalize large variations in the spatial gradient of updating parameters. An improved VFM strategy, the Regularized Virtual Fields Method (RVFM), has been recently proposed by the authors (Rahmani *et al.*, 2013b) to determine the in-situ properties of fiber composites from bi-dimensional (2D) full-field measurements. In this approach, regularization constraints based on a micromechanical homogenization model were exploited so as to regularize solving the related system of equations. The RVFM demonstrated to be quite robust against noise effects, particularly for characterizing the stiffer phase (particles), which had a much lower signal to noise ratio than the more compliant phase (matrix). Most of the studies devoted to VFM relied on 2D kinematic fields. Considering the recent advances in 3D imaging techniques and the need for local characterization of 3D composites, it would be of interest to evaluate, at least theoretically, the robustness of such an approach for 3D problems.

In DVC measurements, only a small Region of Interest (ROI) from the whole material is typically processed for the sake of image magnification requirements (as depicted in Figure 6.1). Under such circumstances, internal stresses on the ROI's boundaries are likely to be different than those applied on the whole sample. This represents an important challenge since the local mechanical properties must link the internal strains (known) and the stresses (unknown). Moreover, other sources of errors such as important noise and artifact created by current μCT scanners, as well as the systematic errors related to DVC can induce uncertainties to the full field measurements and, consequently, to the identified parameters.

The main objective of this research work was to extend the VFM and RVFM to 3D and to apply it to particulate composites applications. Virtual experiments were conducted in which 3D composites reinforced by particles of different aspect ratios and volume fractions were simulated. The virtual composites were artificially deformed and 3D strain fields were obtained over the voxels of the microstructures. The performance of both 3D VFM and RVFM was assessed against noisy strain fields and for ROI of different sizes.

This paper is organized as follows. Section 6.3 deals with the theoretical aspects of the virtual fields method and its extension to 3D. Section 6.3.2 introduces the RVFM identification methodology developed for particulate composites. Sections 6.4 and 6.5 are related to the application of both VFM and RVFM identification methodologies to the virtual composites and the related results, respectively. The paper ends up with the concluding remarks of the

study in section 6.6.

6.3 Theoretical background

6.3.1 The Virtual Fields Method

The VFM relies on writing the global equilibrium of a body subjected to a given load through the principle of virtual work (Pierron et Grédiac, 2012) as

$$-\int_V \boldsymbol{\sigma} : \boldsymbol{\varepsilon}^* \, \mathrm{d}V + \int_{\partial V} \boldsymbol{T} \cdot \mathbf{u}^* \, \mathrm{d}S = 0 \quad \forall \mathbf{u}^* \in \mathcal{KA} \tag{6.1}$$

where V is the volume and ∂V is the boundary of the body, $\boldsymbol{\sigma}$ is the stress tensor, $\mathbf{u}^*$ and $\boldsymbol{\varepsilon}^*$ are the virtual displacement and the corresponding strain fields, respectively, $\mathbf{T}$ are the tractions acting on the boundaries and $\mathcal{KA}$ stands for Kinematically Admissible conditions. For linear homogeneous materials, the constitutive equation can be expressed as:

$$\sigma_i = Q_{ij} \, \varepsilon_j \tag{6.2}$$

where Q_{ij} are the stiffness components to be identified and ε_j are full-field measured strain components coming from experimental tests. Accordingly, the principle of virtual work stated

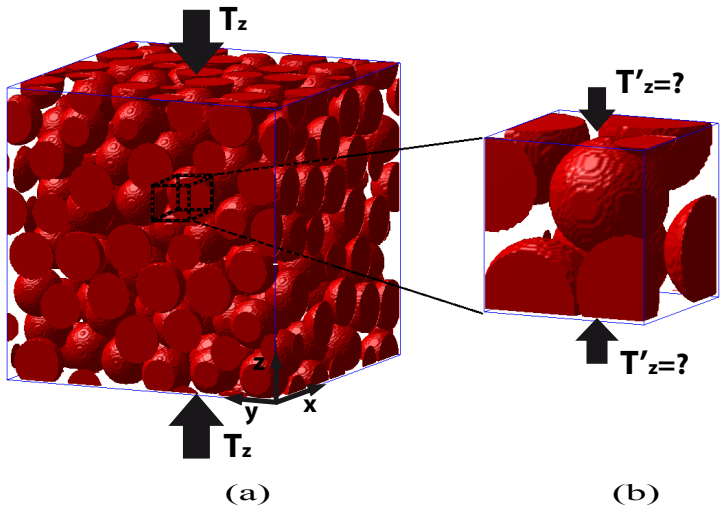

Figure 6.1: (a) Schematic representation of a complete sample being submitted to an external load, (b) Schematic region of interest for which strains would be computed from a DVC algorithm applied on images obtained from μCT.

in Eq. 6.1 can be written as:

$$-\int_V Q_{ij}\,\varepsilon_j\varepsilon_i^*\,\mathrm{d}V+\int_{\partial V} T_i u_i^*\,\mathrm{d}S=0\quad\forall\mathbf{u^*}\in\mathcal{KA} \tag{6.3}$$

The matrix form of the constitutive equation (6.2) is represented as:

$$\begin{Bmatrix}\sigma_1\\ \sigma_2\\ \sigma_3\\ \sigma_4\\ \sigma_5\\ \sigma_6\end{Bmatrix}=\begin{bmatrix}Q_{11}&Q_{12}&Q_{13}&0&0&0\\ Q_{21}&Q_{22}&Q_{23}&0&0&0\\ Q_{31}&Q_{32}&Q_{33}&0&0&0\\ 0&0&0&Q_{44}&0&0\\ 0&0&0&0&Q_{55}&0\\ 0&0&0&0&0&Q_{66}\end{bmatrix}\begin{Bmatrix}\varepsilon_1\\ \varepsilon_2\\ \varepsilon_3\\ \varepsilon_4\\ \varepsilon_5\\ \varepsilon_6\end{Bmatrix} \tag{6.4}$$

In the case of isotropy, the principle of virtual work (Eq. 6.3) can be written as:

$$\begin{aligned}Q_{11}\int_V\Big(\varepsilon_1\varepsilon_1^*+\varepsilon_2\varepsilon_2^*+\varepsilon_3\varepsilon_3^*+\frac{1}{2}\varepsilon_4\varepsilon_4^*+\frac{1}{2}\varepsilon_5\varepsilon_5^*+\frac{1}{2}\varepsilon_6\varepsilon_6^*\Big)\,\mathrm{d}V+\\ Q_{12}\int_V\Big(\varepsilon_2\varepsilon_1^*+\varepsilon_3\varepsilon_1^*+\varepsilon_1\varepsilon_2^*+\varepsilon_3\varepsilon_2^*+\varepsilon_1\varepsilon_3^*+\varepsilon_2\varepsilon_3^*-\frac{1}{2}\varepsilon_4\varepsilon_4^*-\frac{1}{2}\varepsilon_5\varepsilon_5^*-\frac{1}{2}\varepsilon_6\varepsilon_6^*\Big)\,\mathrm{d}V\\ =\int_{S_f}T_i u_i^*\,\mathrm{d}S\quad\forall\mathbf{u^*}\in\mathcal{KA}\end{aligned} \tag{6.5}$$

where

$$\begin{cases}Q_{11}=Q_{22}=Q_{33}=\dfrac{E\,(1-\nu)}{(1-2\nu)(1+\nu)}\\ Q_{12}=Q_{21}=Q_{13}=Q_{31}=Q_{23}=Q_{32}=\dfrac{E\,\nu}{(1-2\nu)(1+\nu)}\\ Q_{44}=Q_{55}=Q_{66}=\dfrac{E}{2(1+\nu)}=\dfrac{Q_{11}-Q_{12}}{2}\end{cases} \tag{6.6}$$

where E and ν are Young's modulus and Poisson's ratio, respectively. The principle of virtual work is then extended based on a set of independent $\mathcal{KA}$ virtual fields (test functions). If as many independent virtual fields as there are unknown parameters are chosen, Eq. 6.5 leads to the following linear system of equations:

$$\mathbf{A}\cdot\mathbf{q}=\mathbf{b} \tag{6.7}$$

where $\mathbf{A}$ is a square matrix, $\mathbf{b}$ is a vector whose components are the virtual work of the applied forces corresponding to each virtual field and $\mathbf{q}$ is a vector containing the unknown parameters of $\mathbf{Q}$. The solution of this linear system delivers the sought parameters. The perturbations induced in the measured strain data, however, might affect the uniqueness of the solution and lead to variations in the identified parameters.
The choice of an appropriate set of virtual displacement functions is one of the key aspects for obtaining satisfactory parameters. Depending on the actual boundary conditions, these test functions may be chosen among an infinite number of possibilities meeting two conditions: *i*) they must be differentiable and have C^0 continuity; *ii*) they must be chosen such that the resulting equations are linearly independent in order for the linear system to be invertible. The stability of the linear system against noisy measured data depends strongly on the level of independence of the chosen virtual fields.

6.3.2 The Regularized Virtual Fields Method

The linear system presented in Eq. 6.7 is solved directly (i.e. by matrix inversion method) in the VFM. In the RVFM (Rahmani *et al.*, 2013b), however, the idea is to solve Eq. 6.7 in an optimization framework where, for the purpose of regularization, a set of mechanically relevant constraints are added. To this end, a least square objective function is defined as

$$r(\mathbf{q}) = \Big(\mathbf{A}\cdot\mathbf{q}-\mathbf{b}\Big)^T\cdot\Big(\mathbf{A}\cdot\mathbf{q}-\mathbf{b}\Big) \tag{6.8}$$

The regularization constraints are defined as the discrepancy between the effective properties predicted by an appropriate homogenization model and those obtained from experimental tests. Hence, the RVFM aims at minimizing $r(\mathbf{q})$ subjected to the following constraints:

$$\mid(\tilde{\Lambda}_l(\mathbf{q})-\hat{\Lambda}_l)\mid\leq\gamma\quad(l=1,2,...,M) \tag{6.9}$$

where $\tilde{\Lambda}$ and $\hat{\Lambda}$ represent the effective mechanical properties obtained from a homogenization model and from experimental data, respectively; M is the number of constraints and γ is a very small positive definite quantity. The constraints are evaluated at each iteration by updating the sought parameters. Assuming that the composite effective shear and bulk modulii are known, and also depend on the matrix and particles properties, the imposed constraints restrict the optimization algorithm to follow rational search directions relying on the effective properties. This regularization can be interpreted as error averaging of the measured data that reduces significantly the noise effects, thus biasing the solution towards

points very close to those of noise-free fields. Indeed, adding appropriate physical information when minimizing $r(\mathbf{q})$ can improve the accuracy of the identified parameters. It should be noted that this regularization can be efficient as long as an accurate homogenization model is employed in the constraints.

6.3.3 Homogenization models

Homogenization methods deliver estimates for the effective properties of composites using information related to their constitutive phases mechanical properties and geometry. The Mori-Tanaka model (Mori et Tanaka, 1973), the Lielens' model (Lielens *et al.*, 1998) and the third order approximation (TOA) (Torquato, 1991) are examples of analytical homogenization models that have been widely used in the literature. The two latter have been proven to be more reliable for delivering accurate effective properties, particularly for composites having high volume fractions and contrasts of properties between phases (Ghossein et Lévesque, 2012).

6.4 Application of the VFM and RVFM to particulate composites

This section details the application of both the VFM and the RVFM to particulate composites. The methodology followed three steps: *i*) The generation of virtual particulate composites 3D microstructures of various volume fractions and particles shapes; *ii*) The computation of a 3D strain fields resulting from imposed boundary conditions. The strain fields were perturbed by additive Gaussian white noise prior to composite properties characterization. These modified fields were considered as "measured" strain fields; *iii*) The identification of the virtual composites constitutive phases properties using the resulting "measured" strain fields. The RVFM optimization problem was solved by a gradient free optimization method and the relative constraints values were evaluated by an appropriate homogenization model. The following subsections provide methodological details for the above-mentioned steps.

6.4.1 3D microstructure of the composites and mechanical properties

The two types of composites studied in this work were composed of an isotropic matrix reinforced by randomly distributed spherical or ellipsoidal particles, as shown in Figure 6.2. The 3D microstructures were generated using the Molecular Dynamic (MD) method implemented by Ghossein and Levesque (Ghossein et Lévesque, 2012; Ghossein et Levesque, 2013). Table 6.1 shows the reference mechanical properties considered for the constitutive

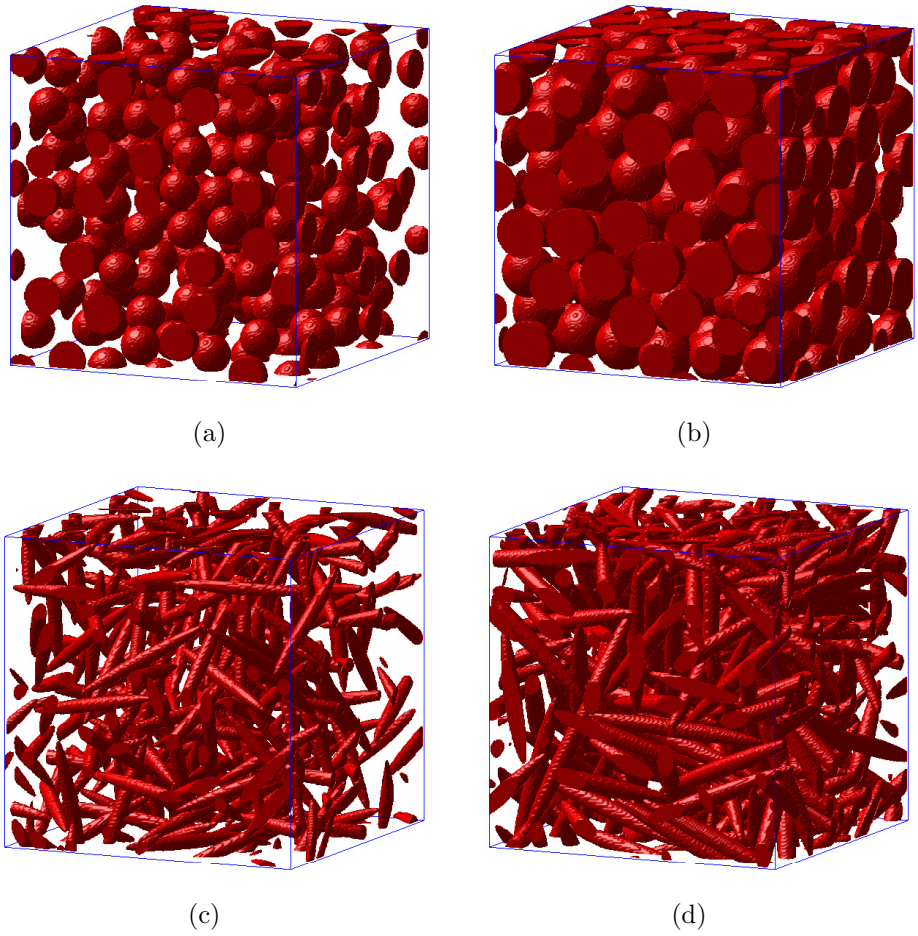

Figure 6.2: 3D microstructures of the particulate composites: (a) composite A with spherical particles at a volume fraction of 20%; (b) composite A′ with spherical particles at a volume fraction of 50%, (c) composite B with ellipsoidal particles of aspect ratio 10 at a volume fraction of 10% and (d) composite B′ with ellipsoidal particles of aspect ratio 10 at a volume fraction of 20%.

phases, where subscripts p and m refer to the particles and matrix, respectively. The chosen mechanical properties are typical of E-glass-epoxy composites.

6.4.2 Stress and strain fields computation

The composites were deformed through applying overall strains in different directions in order to generate 3D strain fields. Stress and strain fields were computed using a technique based on Fast Fourier Transforms (FFT) that was initially proposed by Moulinec et Suquet (Moulinec et Suquet, 1998b). The advantage of this method stems from its rate of convergence

and the fact that it does not require meshing. The method was implemented in detail in (Ghossein et Lévesque, 2012) and only specific details related to the current study are provided in the following sub-sections.

Discretization of the microstructures

Microstructures were discretized into $256 \times 256 \times 256$ voxels. For each voxel, the position of 9 points was verified. The stiffness tensor of the voxel, denoted by $\mathbf{C}(\boldsymbol{x})$, was obtained as follows:

$$\begin{cases} \mathbf{C}(\boldsymbol{x}) = \mathbf{C}_p & \text{if 5 points or more belonged to a particle} \\ \mathbf{C}(\boldsymbol{x}) = \mathbf{C}_m & \text{Otherwise} \end{cases} \tag{6.10}$$

Computation of the stress and strain fields using FFT

The stress and strain fields were obtained by solving the Lippman-Schwinger equation (Moulinec et Suquet, 1998b) in Fourier space:

$$\boldsymbol{\varepsilon}^{n+1}(\boldsymbol{x}) = \mathcal{F}^{-1}\left[\mathcal{F}\Big(\boldsymbol{\varepsilon}^{n}(\boldsymbol{x})\Big) - \boldsymbol{\Gamma}_0(\boldsymbol{\xi}) : \mathcal{F}\Big(\mathbf{C}(\boldsymbol{x}) : \boldsymbol{\varepsilon}^{n}(\boldsymbol{x})\Big)\right] \tag{6.11}$$

where $\mathcal{F}$ and $\mathcal{F}^{-1}$ refer respectively to the Fast Fourier Transform and its inverse. $\boldsymbol{\Gamma}^0(\boldsymbol{\xi})$ denotes the Green operator and is expressed as follow:

$$\boldsymbol{\Gamma}_0(\boldsymbol{\xi}) = \frac{1}{4\mu_0\|\boldsymbol{\xi}\|^2}\left(\delta_{ki}\xi_l\xi_j + \delta_{li}\xi_k\xi_j + \delta_{kj}\xi_l\xi_i + \delta_{lj}\xi_k\xi_i\right) - \frac{\lambda_0 + \mu_0}{\mu_0\left(\lambda_0 + 2\mu_0\right)}\frac{\xi_i\xi_j\xi_k\xi_l}{\|\boldsymbol{\xi}\|^4} \tag{6.12}$$

where $\boldsymbol{\xi}$ denotes the frequencies in Fourier space. μ_0 and λ_0 represent respectively the shear and Lamé modulus of the reference material. These moduli were given by:

Table 6.1: Reference elastic mechanical properties for the virtual composites

Composite	volume fraction	particles	E_p(GPa)	ν_p	E_m(GPa)	ν_m
A	20	Spherical	74	0.2	3.5	0.35
A′	50					
B	10	Ellipsoidal	74	0.2	3.5	0.35
B′	20					

$$\mu_0 = -\sqrt{\mu_m \mu_f} \tag{6.13a}$$

$$\lambda_0 = -\sqrt{\kappa_m \kappa_f} - \frac{2}{3}\mu_0 \tag{6.13b}$$

Equation (6.11) was solved iteratively until the strain field convergence was achieved. The algorithm was initialized with uniform strains applied in different directions:

$$\boldsymbol{\varepsilon}^0(\boldsymbol{x}) = \begin{bmatrix} -\widetilde{\nu}e & 0 & 0 \\ 0 & -\widetilde{\nu}e & 0 \\ 0 & 0 & e \end{bmatrix} \tag{6.14}$$

where $\widetilde{\nu}$ is the effective Poisson's ratio of the composite and was computed using the methodology presented in Section 6.4.3. In this study, e was set to -0.02. This led to effective stresses σ_x and $\sigma_y \approx 0$ ($\approx 10^{-7}$ in practice) and an effective stress $\sigma_z = -T_z$, where T_z depended on the composites microstructure. Finally, Gaussian white noise was added to the resulting strain fields. The standard deviation of the additive noise was approximately 10% of the mean strain values. Figure 6.3 depicts typical simulated ε_z fields, perturbed with that noise level.

6.4.3 Determination of effective properties

Effective properties of a single microstructure

The regularization constraints presented in Eq. 6.9 require the composites effective properties. The effective stiffness tensor of a single microstructure $\widehat{\mathbf{C}}$ was deduced from the relation between the volume averaged stresses and strains:

$$\left\langle \boldsymbol{\sigma}(\boldsymbol{x}) \right\rangle = \widehat{\mathbf{C}} : \left\langle \boldsymbol{\varepsilon}(\boldsymbol{x}) \right\rangle \tag{6.15}$$

where $\langle \cdot \rangle$ represents volume averaging. Six orthogonal deformation states were applied to obtain all the terms of $\widehat{\mathbf{C}}$. For example, the first column was obtained by applying a unit strain field in the first principal direction ($\varepsilon^0_{11}(\boldsymbol{x}) = 1$ and ε_{jj}, for j = 2 to 6, =0). The five other columns were computed similarly.

The effective elastic bulk and shear moduli $\widehat{\kappa}$ and $\widehat{\mu}$, respectively, were then calculated as:

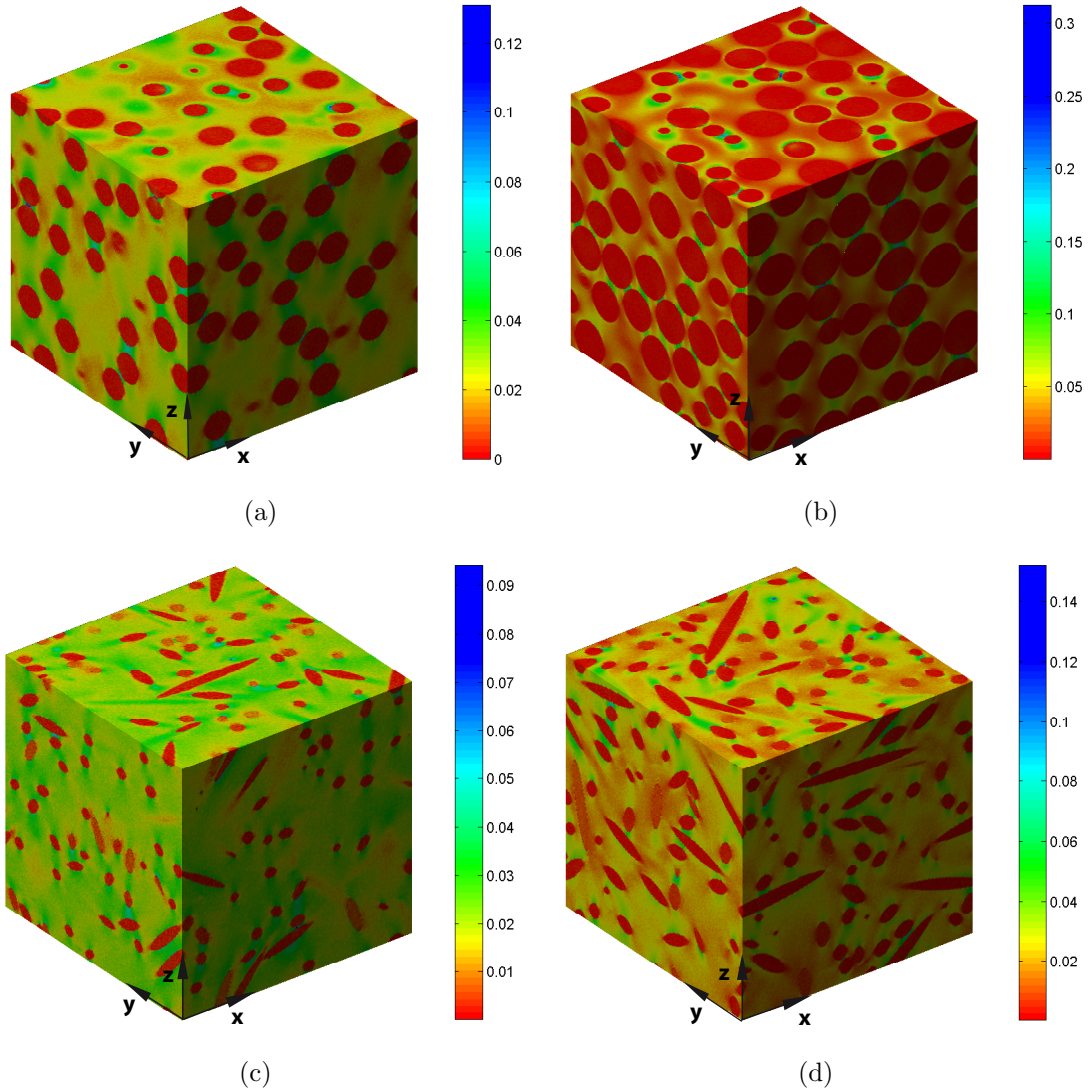

Figure 6.3: Noisy ε_z for (a) composite A, (b) composite A′, (c) composite B and (d) composite B′, subjected to an overall uni-axial compressive stress in z

$$\widehat{\kappa} = \frac{1}{3}\,\widehat{\mathbf{C}} :: \mathbf{J} \tag{6.16a}$$

$$\widehat{\mu} = \frac{1}{10}\,\widehat{\mathbf{C}} :: \mathbf{K} \tag{6.16b}$$

where $\mathbf{J}$ and $\mathbf{K}$ are the isotropic projector tensors.

Representive Volume Element determination

For each combination of contrasts and volume fractions, the size of the Representative Volume Element (RVE) was determined using the methodology of Kanit et al. (Kanit *et al.*, 2003). For each number of particles, several random realizations were performed and the effective properties were obtained for each generated microstructure. The number of realizations was increased until the width of a 95% level confidence interval on the mean effective property was smaller than a prescribed value (see (Ghossein et Lévesque, 2012) for more detail). The procedure was then repeated for an increasing number of particles until the arithmetic mean of both effective moduli converged.
After determining RVE size, 3D microstructure of all composites with 200 particles, which was larger than the RVE, were generated and the corresponding strain/stress fields were simulated. These largest sizes (as shown in Figure 6.2) were considered as ROI of dimension $1 \times 1 \times 1$.

6.4.4 Parameters identification with VFM and RVFM

Both VFM and RVFM identification methods were applied with the aim of retrieving the reference elastic parameters of the composites constituents initially used to generate the artificially "measured" strain fields.

Identification using the VFM

Considering that the whole material was not homogeneous, the VFM relation presented in Eq. 6.5 was developed for a two-phase material. For factorizing the sought parameters out of the volume integrals, the overall volume of the composite (V) was split into $V - V'$ and V', i.e. the matrix and particles sub-volumes, respectively. Hence, after defining Q_{11}, Q_{12} and Q'_{11}, Q'_{12} as the stiffness components over $V - V'$ and V', respectively, Eq. 6.5 becomes:

$$Q_{11}\int\limits_{V-V'}\left(\varepsilon_1\varepsilon_1^*+\varepsilon_2\varepsilon_2^*+\varepsilon_3\varepsilon_3^*+\frac{1}{2}\varepsilon_4\varepsilon_4^*+\frac{1}{2}\varepsilon_5\varepsilon_5^*+\frac{1}{2}\varepsilon_6\varepsilon_6^*\right)\mathrm{d}V+$$
$$Q_{12}\int\limits_{V-V'}\left(\varepsilon_2\varepsilon_1^*+\varepsilon_3\varepsilon_1^*+\varepsilon_1\varepsilon_2^*+\varepsilon_3\varepsilon_2^*+\varepsilon_1\varepsilon_3^*+\varepsilon_2\varepsilon_3^*-\frac{1}{2}\varepsilon_4\varepsilon_4^*-\frac{1}{2}\varepsilon_5\varepsilon_5^*-\frac{1}{2}\varepsilon_6\varepsilon_6^*\right)\mathrm{d}V+$$
$$Q'_{11}\int\limits_{V'}\left(\varepsilon_1\varepsilon_1^*+\varepsilon_2\varepsilon_2^*+\varepsilon_3\varepsilon_3^*+\frac{1}{2}\varepsilon_4\varepsilon_4^*+\frac{1}{2}\varepsilon_5\varepsilon_5^*+\frac{1}{2}\varepsilon_6\varepsilon_6^*\right)\mathrm{d}V+$$
$$Q'_{12}\int\limits_{V'}\left(\varepsilon_2\varepsilon_1^*+\varepsilon_3\varepsilon_1^*+\varepsilon_1\varepsilon_2^*+\varepsilon_3\varepsilon_2^*+\varepsilon_1\varepsilon_3^*+\varepsilon_2\varepsilon_3^*-\frac{1}{2}\varepsilon_4\varepsilon_4^*-\frac{1}{2}\varepsilon_5\varepsilon_5^*-\frac{1}{2}\varepsilon_6\varepsilon_6^*\right)\mathrm{d}V$$
$$=\int\limits_{S_f}T_iu_i^*\,\mathrm{d}S\quad\forall\mathbf{u^*}\in\mathcal{KA}\quad(6.17)$$

Four $\mathcal{KA}$ independent virtual fields had to be chosen for each microstructure. The virtual fields were chosen so as to prevent any rigid body motion, while not perturbing the stress and strain fields generated at Section 6.4.2. Figure 6.4 shows the values these fields took on the boundaries of the studied ROIs.

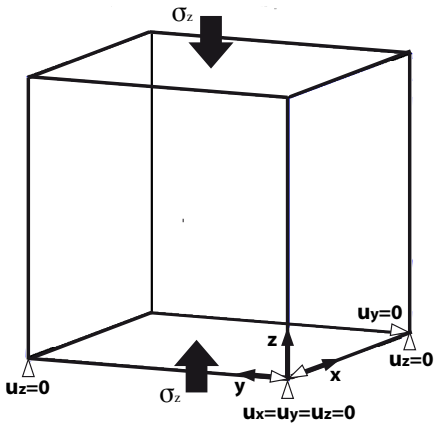

Figure 6.4: Free body diagram of a sample ROI

The following different sets of virtual fields were tested for all microstructures:

Set 1:

$$\begin{cases} u_1^{*(1)} = x \\ u_2^{*(1)} = 0 \\ u_3^{*(1)} = 0 \end{cases} \quad (6.18a) \qquad \begin{cases} u_1^{*(2)} = 0 \\ u_2^{*(2)} = y \\ u_3^{*(2)} = 0 \end{cases} \quad (6.18b)$$

$$\begin{cases} u_1^{*(3)} = 0 \\ u_2^{*(3)} = 0 \\ u_3^{*(3)} = z \end{cases} \quad (6.18c) \qquad \begin{cases} u_1^{*(4)} = 0 \\ u_2^{*(4)} = 0 \\ u_3^{*(4)} = \dfrac{z^3}{3} \end{cases} \quad (6.18d)$$

Set 2:

$$\begin{cases} u_1^{*(1)} = \dfrac{x^2}{2} \\ u_2^{*(1)} = 0 \\ u_3^{*(1)} = 0 \end{cases} \quad (6.19a) \qquad \begin{cases} u_1^{*(2)} = 0 \\ u_2^{*(2)} = \dfrac{y^3}{3} \\ u_3^{*(2)} = 0 \end{cases} \quad (6.19b)$$

$$\begin{cases} u_1^{*(3)} = 0 \\ u_2^{*(3)} = 0 \\ u_3^{*(3)} = z \end{cases} \quad (6.19c) \qquad \begin{cases} u_1^{*(4)} = 0 \\ u_2^{*(4)} = 0 \\ u_3^{*(4)} = \dfrac{z^3}{3} \end{cases} \quad (6.19d)$$

Set 3:

$$\begin{cases} u_1^{*(1)} = \sin(\dfrac{\pi x}{4}) \\ u_2^{*(1)} = 0 \\ u_3^{*(1)} = 0 \end{cases} \quad (6.20a) \qquad \begin{cases} u_1^{*(2)} = 0 \\ u_2^{*(2)} = \sin(\dfrac{\pi y}{4}) \\ u_3^{*(2)} = 0 \end{cases} \quad (6.20b)$$

$$\begin{cases} u_1^{*(3)} = 0 \\ u_2^{*(3)} = 0 \\ u_3^{*(3)} = z \end{cases} \quad (6.20c) \qquad \begin{cases} u_1^{*(4)} = 0 \\ u_2^{*(4)} = 0 \\ u_3^{*(4)} = \dfrac{z^3}{3} \end{cases} \quad (6.20d)$$

Set 4:

$$\begin{cases} u_1^{*(1)} = \exp(x) \\ u_2^{*(1)} = 0 \\ u_3^{*(1)} = 0 \end{cases} \quad (6.21a) \qquad \begin{cases} u_1^{*(2)} = 0 \\ u_2^{*(2)} = \exp(y) \\ u_3^{*(2)} = 0 \end{cases} \quad (6.21b)$$

$$\begin{cases} u_1^{*(3)} = 0 \\ u_2^{*(3)} = 0 \\ u_3^{*(3)} = z \end{cases} \quad (6.21c) \qquad \begin{cases} u_1^{*(4)} = 0 \\ u_2^{*(4)} = 0 \\ u_3^{*(4)} = \dfrac{z^3}{3} \end{cases} \quad (6.21d)$$

The virtual fields of Set 2 and Set 3 shown to be sufficiently independent when employed for the microstructures with ellipsoidal and spherical particles, respectively. The effects of virtual fields definition on the identified parameters is presented in section 6.5.
Consider, for example, the virtual fields of Set 1. Since the tractions in x and y directions were null, the first two components of vector $\mathbf{b}$ were zero. Assuming identical dimensions of the ROI in all directions ($L_x = L_y = L_z = L$), the other components of vector $\mathbf{b}$ were determined using the corresponding virtual displacements

$$b_3 = \int_0^L \int_0^L T_3(x,y,0)\, u_3^{*(3)}\, \mathrm{d}x\, \mathrm{d}y + \int_0^L \int_0^L T_3(x,y,L)\, u_3^{*(3)}\, \mathrm{d}x\, \mathrm{d}y = 0 + \int_0^L \int_0^L F_3\, z\, \mathrm{d}x\, \mathrm{d}y = F_3 L^3 \quad (6.22a)$$

$$b_4 = \int_0^L \int_0^L F_3\, \frac{z^3}{3}\, \mathrm{d}x\, \mathrm{d}y = \frac{F_3 L^5}{3} \quad (6.22b)$$

Hence, the following linear system of equations was built up from Eq. 6.17 and the virtual fields presented above:

$$\begin{bmatrix} \int_{V-V'} \varepsilon_1 dV & \int_{V-V'} (\varepsilon_2+\varepsilon_3) dV & \int_{V'} \varepsilon_1 dV & \int_{V'} (\varepsilon_2+\varepsilon_3) dV \\ \int_{V-V'} \varepsilon_2 dV & \int_{V-V'} (\varepsilon_1+\varepsilon_3) dV & \int_{V'} \varepsilon_2 dV & \int_{V'} (\varepsilon_1+\varepsilon_3) dV \\ \int_{V-V'} \varepsilon_3 dV & \int_{V-V'} (\varepsilon_1+\varepsilon_2) dV & \int_{V'} \varepsilon_3 dV & \int_{V'} (\varepsilon_1+\varepsilon_2) dV \\ \int_{V-V'} \varepsilon_3 z^2 dV & \int_{V-V'} (\varepsilon_1 z^2+\varepsilon_2 z^2) dV & \int_{V'} \varepsilon_3 z^2 dV & \int_{V'} (\varepsilon_1 z^2+\varepsilon_2 z^2) dV \end{bmatrix} \begin{Bmatrix} Q_{11} \\ Q_{12} \\ Q'_{11} \\ Q'_{12} \end{Bmatrix} = \begin{Bmatrix} 0 \\ 0 \\ F_3 L^3 \\ \frac{F_3 L^5}{3} \end{Bmatrix} \quad (6.23)$$

The integrals were approximated by discrete sums over the voxel points. For instance:

$$\int_{V-V'} \varepsilon_3 dV \simeq \sum_{i=1}^{p} \varepsilon_3^i v^i \tag{6.24}$$

where p is the number of data points over $(V - V')$ and v^i are their volumes. Appendix A presents the system of equations derived from Sets 1, 2 and 4.

The linear system in Eq. 6.23 was solved through matrix inversion method (for the VFM) as well as by using a constrained optimization procedure (for the RVFM) in order to determine the stiffness components.

The elastic parameters of the constitutive phases were directly related to the sought stiffness components by the following relations:

$$\begin{aligned} \nu_m &= \frac{Q_{12}}{Q_{11}+Q_{12}}, \quad E_m = \frac{Q_{11}(1-2\nu_m)(1+\nu_m)}{(1-\nu_m)} \\ \nu_p &= \frac{Q'_{12}}{Q'_{11}+Q'_{12}}, \quad E_p = \frac{Q'_{11}(1-2\nu_p)(1+\nu_p)}{(1-\nu_p)} \end{aligned} \tag{6.25}$$

RVFM optimization problem

The relevant equations for each system were used to create a least square objective functions based on Eq.(8). Hence, the RVFM consisted of solving the following optimization problem

$$\begin{aligned} &\min\ r(\mathbf{q}) = \Big(\mathbf{A}\cdot\mathbf{q}-\mathbf{b}\Big)^T \cdot \Big(\mathbf{A}\cdot\mathbf{q}-\mathbf{b}\Big) \\ &\text{Subjected to} \\ &\quad \mid \widetilde{\kappa}^H(\mathbf{q}) - \widehat{\kappa}^{FFT} \mid \leq \gamma_1 \\ &\quad \mid \widetilde{\mu}^H(\mathbf{q}) - \widehat{\mu}^{FFT} \mid \leq \gamma_2 \end{aligned} \tag{6.26}$$

where superscript H refers to homogenization model, FFT to the properties computed by the FFT method, and γ_1 and γ_2 were set to 1% of the corresponding effective properties. Lielens and TOA homogenization models were used for predicting the effective shear and bulk modulii, respectively, for the microstructures with spherical particles. Lielens homogenization model was also exploited for the microstructures with ellipsoidal particles.

The optimization problem of the RVFM was solved with the Mesh Adaptive Direct Search (MADS) optimization method (Audet et Dennis Jr., 2006), which demonstrated to be quite successful in a previous study by the current authors (Rahmani *et al.*, 2013b). MADS is a frame-based global optimization algorithm for solving nonlinear problems without requiring

derivative information. The method is known to be quite robust for optimization problems with nonsmooth objective functions subjected to nonsmooth constraints. The VFM solutions were considered as initial guesses for the RVFM algorithm. The constraints values were evaluated at each iteration by substituting the trial parameters into the related homogenization model, and their feasibility was checked by the constraints. The stopping criterion considered for all optimizations was 300 objective function evaluation.

6.4.5 Parameters identification from small ROIs

In practice, strain information of a small region, as a representative of whole microstructure (as illustrated in Figure 6.1), is processed for identification purposes. The load distribution on the boundaries of such small volumes is not fully determined. Indeed, if the ROI is not large enough to be a Representative Volume Element (RVE), then the overall stresses over its boundaries will differ from those applied on the whole sample.
Assuming that virtual fields in the VFM are carefully chosen, inaccurate values of tractions might affect the accuracy of the identified mechanical parameters. On the other hand, strain fields measured with DVC at higher magnifications (smaller ROIs) can better capture heterogenous deformation patterns and discontinuities created due to phases contrast of properties. Therefore, an optimum size of ROI which satisfies the requirements of both RVE size and image magnification must be determined. In this study, the influence of ROI size on the identification procedure for both spheres and ellipsoids microstructures was investigated. To this end, smaller sub regions with different sizes of $0.65 \times 0.65 \times 0.65$, $0.5 \times 0.5 \times 0.5$, $0.3 \times 0.3 \times 0.3$ and $0.1 \times 0.1 \times 0.1$ were considered for the identifications. Each ROI was considered as an independent continuum model (as illustrated in Figure 6.4) that was in equilibrium through the tractions created on its boundaries.

6.5 Results and discussions

6.5.1 Identified parameters from the whole microstructure

Table 6.2 shows the obtained parameters resulting from different sets of virtual fields in the VFM for the composites A and B. As it can be seen, Set 3 and Set 2 led to much more accurate results than the other sets for composites A and B, respectively. This is because they constitute sufficiently independent equations in the related systems. The same two sets were demonstrated to be accurate for the composites with larger volume fractions (i.e., composites A' and B', respectively) and were used for the parameters identifications.

Tables 6.3a and 6.3b compare the elastic properties identified using the VFM and RVFM for composites A and A', respectively. The corresponding relative errors of the identified parameters resulting from both methodologies are also reported. The first identification was carried out using exact strain fields (i.e., without any additive noise to the strain data). In this case, the VFM leads to relatively accurate parameters, except for the particles Poisson's ratio. It can be seen that the relative error of the particles parameters identified by the VFM increases in the presence of noise, while the matrix parameters are only slightly influenced by noise effects. This is most probably due to the fact that the signal/noise ratio in the stiffer phase, i.e., the particles, is much lower than that in the matrix phase. Table 6.4 shows the signal/noise ratio (i.e., the ratio of mean strain value to the standard deviation of noise) for the constitutive phases of the two composites. For the composite with larger volume fraction of particles (composite A$'$), however, the identified matrix parameters are less accurate than those of composite A. This might arise from strain concentrations occuring in the matrix phase embedded between close particles aligned in the loading directions.

The corresponding results of the RVFM for both volume fractions, which show low relative errors for both phases in the presence of noise, confirm the robustness of this method. Thanks to the regularization effects imposed by the homogenization models, the RVFM results in more accurate parameters than the VFM in the presence of noise. The lower accuracies for the particles Poisson's ratio identified by the RVFM can be associated to lower sensitivity of the effective properties to the variations in this parameter than the other parameters. This is shown in Figure 6.5, which presents variations in the effective parameters with respect to the

Table 6.2: Identification results for composite A using different sets of virtual fields in the VFM for a noise level of 2% (ROI $1 \times 1 \times 1$)

Virtual fields	$E_p(GPa)$	ν_p	$E_m(GPa)$	ν_m
Reference values	74	0.2	3.5	0.35
		Composite A		
Set 1	3.88	0.499	6.22	0.531
Set 2	79.70	0.350	3.32	0.250
Set 3	74.75	0.227	3.51	0.343
Set 4	79.76	0.362	3.25	0.219
		Composite B		
Set 1	5.54	0.487	4.57	0.247
Set 2	72.10	0.212	3.57	0.343
Set 3	20.80	0.446	4.4	0.269
Set 4	1210	3.19	2.38	0.555

Table 6.3a: Identified parameters and corresponding relative errors (ϵ) for composite A (ROI $1 \times 1 \times 1$)

Method	Noise level	$E_p(GPa)$ (ϵ%)	ν_p (ϵ%)	$E_m(GPa)$ (ϵ%)	ν_m (ϵ%)
Reference values	–	74	0.2	3.5	0.35
VFM	Exact data	73.71 (0.4%)	0.217 (8.5%)	3.53 (0.85%)	0.344 (1.7%)
VFM	10%	70.55 (4.7%)	0.124 (38%)	3.54 (1.1%)	0.360 (2.8%)
RVFM	10%	73.40 (0.8%)	0.213 (7.5%)	3.53 (0.85%)	0.345 (1.4%)

Table 6.3b: Identified parameters and corresponding relative errors (ϵ) for composite A' (ROI $1 \times 1 \times 1$)

Method	Noise level	$E_p(GPa)$ (ϵ%)	ν_p (ϵ%)	$E_m(GPa)$ (ϵ%)	ν_m (ϵ%)
Reference values	–	74	0.2	3.5	0.35
VFM	Exact data	73.49 (0.7%)	0.194 (3%)	3.65 (4.3%)	0.339 (3.1%)
VFM	10%	71.61 (3.2%)	0.224 (12%)	3.82 (9.1%)	0.318 (9.1%)
RVFM	10%	74.01 (0%)	0.182 (9%)	3.47 (0.85%)	0.362 (3.3%)

variations of constituent phases parameters for composite A. Similar trends were observed for composite A' that are not reported here.

Tables 6.5a and 6.5b present the identified parameters for the composites with ellipsoidal particles (composites B and B'), with and without noise. For the noise-free cases, the VFM results in solutions very close to the target values. However, the presence of noise degrades the accuracy of the method, especially regarding the particles properties.

The acquired results indicate that the RVFM is less sensitive to noise effects and leads to more accurate solutions. Trends similar to those shown in Figure 6.5 were observed for the

Table 6.4: Signal/noise ratio for the constituent phases of different composites

Composite	particles	matrix
A	2.27	22.18
A'	4.36	34.45
B	3.30	18.95
B'	3.63	21.81

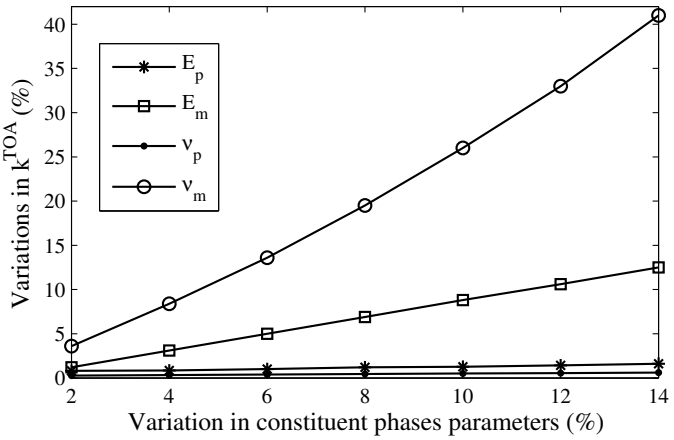

(a)

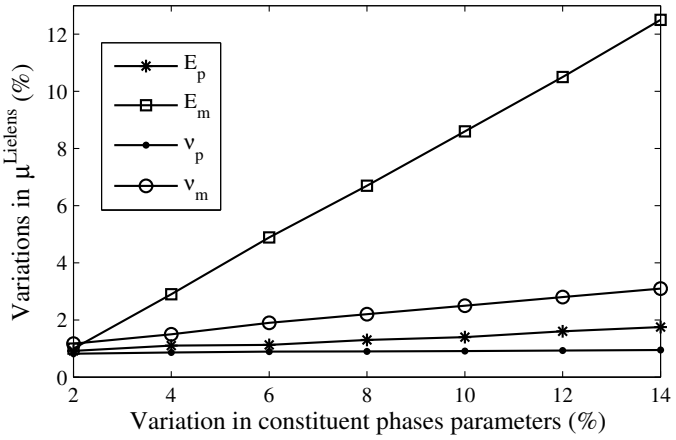

(b)

Figure 6.5: Sensitivity of the effective parameters with respect to variations in the constituent phases properties for composite A; (a) effective bulk modulus predicted by TOA method (b) effective shear modulus predicted by Lielens model

sensitivity of the effective properties to the variations in the constituent phases of composites B and B' (not reported here).

6.5.2 Influence of ROI sizes on the accuracy of identified parameters

The mechanical parameters were identified using both VFM and RVFM from noisy strain data of smaller ROIs. For each ROI size, the constituent properties were obtained from 6 different realizations. These realizations were in fact 'windows' extracted from ROI $1 \times 1 \times 1$

Table 6.5a: Identified parameters and corresponding relative errors (ϵ) for composite B (ROI $1 \times 1 \times 1$)

Method	Noise level	$E_p(GPa)$ ($\epsilon\%$)	ν_p ($\epsilon\%$)	$E_m(GPa)$ ($\epsilon\%$)	ν_m ($\epsilon\%$)
Reference values	–	74	0.2	3.5	0.35
VFM	Exact data	72.27 (2.4%)	0.212 (6%)	3.56 (1.7%)	0.343 (2%)
VFM	10%	70.83 (4.3%)	0.221 (10.5%)	3.60 (2.8%)	0.341 (2.6%)
RVFM	10%	73.20 (1%)	0.207 (3.5%)	3.53 (0.85%)	0.346 (1.1%)

Table 6.5b: Identified parameters and corresponding relative errors (ϵ) for composite B' (ROI $1 \times 1 \times 1$)

Method	Noise level	$E_p(GPa)$ ($\epsilon\%$)	ν_p ($\epsilon\%$)	$E_m(GPa)$ ($\epsilon\%$)	ν_m ($\epsilon\%$)
Reference values	–	74	0.2	3.5	0.35
VFM	Exact data	76.10 (2.8%)	0.189 (5.5%)	3.51 (0.3%)	0.339 (3.1%)
VFM	10%	78.95 (6.7%)	0.190 (5%)	3.39 (3.1%)	0.338 (3.4%)
RVFM	10%	75.81 (2.4%)	0.205 (2.5%)	3.52 (0.6%)	0.344 (1.7%)

described in the previous sections. It should be noted that realizations extracted from larger ROIs ($0.65 \times 0.65 \times 0.65$) overlapped and as a result, were not fully independent. Table 6.6 lists the typical number of represented particles in each ROIs, for composites A' and B', along with the RVE size. Corresponding average relative errors with respect to the exact values were subsequently derived. Table 6.7 presents the obtained results along with two-tailed 95% confidence interval (CI) on the average values for composite A$'$. The average relative errors for the overall stress on the boundary of ROIs with respect to that of the whole composite have also been reported in the table. For the largest ROI (i.e., $0.65 \times 0.65 \times 0.65$), the overall stress is very close to that of the whole sample. This is due to the fact that the chosen size of ROI is very close to that of the RVE. For this reason, the average parameters are also relatively close to those resulting from the ideal condition (Table 3b). Identification using

Table 6.6: Number of particles in different ROIs

ROI size	0.1	0.3	0.5	0.65	1	RVE
Number of particles	1	6	25	55	200	60

ROI $0.5 \times 0.5 \times 0.5$ leads to satisfactory results, although the overall stress is slightly less accurate than the largest ROI. For the smaller ROIs (i.e., $0.3 \times 0.3 \times 0.3$ and $0.1 \times 0.1 \times 0.1$), however, the average error in the overall stresses increases as the size of the ROI decreases. This is obviously associated with the fact that the chosen volumes are not large enough to be a RVE and, therefore, the estimated stresses are considerably different from those of the whole model. This could be considered as a source of error in the small ROIs that induces more uncertainties to the identifications, when compared with larger ROIs. This observation can be explained by the fact that the VFM depends directly on the accuracy of the applied stresses. Moreover, the RVFM does not improve the accuracy of the parameters, when compared to the similar case in the larger ROI. In some cases, the RVFM even degraded the accuracy of the particles parameters, which was due to the biases created in optimization as a consequence of error in the overall applied stress.

Table 6.8 lists the average relative errors of the identified parameters as well as the overall stresses resulting from different sizes of ROIs for composite B′. Similarly to the previous case, identification using the two larger ROIs resulted in satisfactory parameters, whereas the smaller ROIs led to inaccurate mechanical parameters, especially regarding the particles phase. It is worth mentioning that a similar trend, in terms of the accuracy of identified parameters with respect to ROI sizes, was observed for 2D composites in (Rahmani *et al.*, 2013b).

According to the quality of the resulting parameters, the ROI $0.65 \times 0.65 \times 0.65$ could be considered as the smallest size for both microstructures.

Hence, the optimum size of ROI for a given composite with spherical particles can be estimated, a priori, using the following relation

$$L_{opt} = \left(\frac{N_{RVE} \pi {d_s}^3}{6c} \right)^{\frac{1}{3}} \tag{6.27}$$

where L_{opt} is the edge length of the optimum ROI, N_{RVE} is the size of RVE (number of particles in the RVE), d_s is the diameter of spheres and c denotes particles volume fraction. The following relation can also be defined for the composites including ellipsoidal particles

$$L_{opt} = \left(\frac{N_{RVE} \pi d_{e1} d_{e2} d_{e3}}{6c} \right)^{\frac{1}{3}} \tag{6.28}$$

Table 6.7: Average relative error of the identified parameters for composite A′ from different ROIs (noise level=10%)

Method	E_p *error* (CI)	ν_p *error* (CI)	E_m *error* (CI)	ν_m *error* (CI)	Stress error
		ROI $0.65 \times 0.65 \times 0.65$			
VFM	1.7% (0.7 , 2.8)	12.9% (9.7 , 16)	8.1% (5.8 , 9.9)	8.7% (6.1 , 10)	1%
RVFM	1.9% (1 , 2.8)	8.5 % (6.8 , 10)	1.8% (1.3 , 2.2)	2.5% (1.7 , 3.4)	
		ROI $0.5 \times 0.5 \times 0.5$			
VFM	1.6% (0.6 , 2.6)	15.9% (6.3 , 25)	7.7% (5.3 , 10)	8.9% (7.1 , 10.8)	2.1%
RVFM	2.0% (0.9 , 3.1)	10.0% (7.5 , 12)	1.7% (1.1 , 2.2)	2.8% (2.1 , 3.6)	
		ROI $0.3 \times 0.3 \times 0.3$			
VFM	9.4% (4.1 , 14.8)	6.9% (4.1 , 9.6)	12.9% (2.6 , 23)	9.4% (5.8 , 12.9)	8.83%
RVFM	11.1% (4.2 , 17.8)	10.2% (8.8 , 11.4)	3.4% (1.1 , 5.8)	2.8% (1.2 , 4.2)	
		ROI $0.1 \times 0.1 \times 0.1$			
VFM	19.4% (13.9 , 24.7)	7.0% (5.6 , 8.3)	16.1% (5.6 , 26)	9.0% (6.7 , 11.4)	18.7%
RVFM	20.2% (15.6 , 24.7)	8.9% (4.2 , 13.6)	5.2% (3.6 , 6.7)	4.2% (1.4 , 6.9)	

Table 6.8: Average relative error of the identified parameters for composite B′ from different ROIs (noise level=10%)

Method	E_p *error* (CI)	ν_p *error* (CI)	E_m *error* (CI)	ν_m *error* (CI)	Stress error
		ROI $0.65 \times 0.65 \times 0.65$			
VFM	3.9% (2.4 , 5.5)	6.5% (4.4 , 8.7)	3.3% (1.7 , 5.3)	2.9% (2.1 , 3.7)	1.8%
RVFM	3.2% (0.8 , 5.7)	9.5% (8.0 , 11.1)	0.6% (0.2 , 1.0)	1.8% (1.3 , 2.2)	
		ROI $0.5 \times 0.5 \times 0.5$			
VFM	3.7% (2.1 , 5.1)	6.2% (4.8 , 7.6)	3.9% (2.3 , 5.4)	3.2% (2.9 , 3.5)	2.3%
RVFM	3.1% (1.9 , 4.2)	7.7% (6.3 , 9.0)	1.7% (0.7 , 2.7)	2.3% (1.6 , 2.9)	
		ROI $0.3 \times 0.3 \times 0.3$			
VFM	5.5% (1.1 , 10)	7.3% (4.9 , 9.5)	6.8% (4.3 , 9.3)	3.6% (3.2 , 3.9)	6.5%
RVFM	5.8% (1.4 , 10)	10.3% (6.9 , 14)	1.4% (0.6 , 2.1)	1.2% (0.3 , 2.1)	
		ROI $0.1 \times 0.1 \times 0.1$			
VFM	25% (21 , 29)	6.3% (3.8 , 8.9)	25.5% (19 , 32)	3.1% (2.4 , 3.8)	25.3%
RVFM	26% (21 , 30)	13.5% (7.6 , 16)	17.6% (12 , 31)	2.7% (2.2 , 3.1)	

where d_{e1}, d_{e2} and d_{e3} are the ellipsoids diameters in different directions.
The above defined relationships could be useful for guiding the experimentalists in defining the optimum size of their ROIs for accurate properties identification of composites with any mechanical or morphological properties.

6.6 Conclusions

An identification approach based on the Virtual Fields Method (VFM) has been proposed to determine in-situ mechanical properties of composites constitutive phases in 3D. Moreover, a Regularized Virtual Fields Method (RVFM) consisting of homogenization-based constraints was developed so as to regularize the identification procedure and therefore enhance the accuracy of the identified parameters. For performance evaluation, the algorithms were applied to 3D noisy full field strain fields of artificial particulate composites including different volume fractions and particles geometries. The obtained results demonstrate the capabilities of the VFM to determine appropriate parameters of 3D composites in the presence of noisy strain fields. The RVFM, however, by taking advantage of regularization effects, leads to more accurate results. Depending on the type of microstructure in terms of the particles geometry, appropriate homogenization models were employed so as to enhance the accuracy of the identified parameters.

Different ROIs were tested to investigate the influence of their size on the corresponding overall tractions and consequently on the accuracy of the identified parameters. It was found that for ROIs smaller than RVE, neither of the VFM and the RVFM resulted in appropriate mechanical parameters due to the inadequacy of the overall tractions on the boundaries. A helpful comprehensive relationship has also been developed, by which the experimentalists can efficiently determine the optimum ROI size to obtain properties within an adequate range of accuracy. This study could also be very useful for estimating, a priori, the required magnification of 3D images for composites of any mechanical and morphological characteristics.

Appendix A

The linear system made from the virtual fields of Set 2:

$$\begin{bmatrix} \int\limits_{V-V'} \varepsilon_1 x dV & \int\limits_{V-V'} (\varepsilon_2 x + \varepsilon_3 x) dV & \int\limits_{V'} \varepsilon_1 x dV & \int\limits_{V'} (\varepsilon_2 x + \varepsilon_3 x) dV \\ \int\limits_{V-V'} \varepsilon_2 y^2 dV & \int\limits_{V-V'} (\varepsilon_1 y^2 + \varepsilon_3 y^2) dV & \int\limits_{V'} \varepsilon_2 y^2 dV & \int\limits_{V'} (\varepsilon_1 y^2 + \varepsilon_3 y^2) dV \\ \int\limits_{V-V'} \varepsilon_3 dV & \int\limits_{V-V'} (\varepsilon_1 + \varepsilon_2) dV & \int\limits_{V'} \varepsilon_3 dV & \int\limits_{V'} (\varepsilon_1 + \varepsilon_2) dV \\ \int\limits_{V-V'} \varepsilon_3 z^2 dV & \int\limits_{V-V'} (\varepsilon_1 z^2 + \varepsilon_2 z^2) dV & \int\limits_{V'} \varepsilon_3 z^2 dV & \int\limits_{V'} (\varepsilon_1 z^2 + \varepsilon_2 z^2) dV \end{bmatrix} \begin{Bmatrix} Q_{11} \\ Q_{12} \\ Q'_{11} \\ Q'_{12} \end{Bmatrix} = \begin{Bmatrix} 0 \\ 0 \\ F_3 L^3 \\ \frac{F_3 L^5}{3} \end{Bmatrix} \quad (6.29)$$

The linear system derived from the virtual fields of Set 3:

$$\begin{bmatrix} \int\limits_{V-V'} \frac{\pi}{4}\varepsilon_1 \cos(\frac{\pi x}{4}) dV & \int\limits_{V-V'} \frac{\pi}{4}(\varepsilon_2 \cos(\frac{\pi x}{4}) + \varepsilon_3 \cos(\frac{\pi x}{4})) dV & \int\limits_{V'} \frac{\pi}{4}\varepsilon_1 \cos(\frac{\pi x}{4}) dV & \int\limits_{V'} \frac{\pi}{4}(\varepsilon_2 \cos(\frac{\pi x}{4}) + \varepsilon_3 \cos(\frac{\pi x}{4})) dV \\ \int\limits_{V-V'} \frac{\pi}{4}\varepsilon_2 \cos(\frac{\pi y}{4}) dV & \int\limits_{V-V'} \frac{\pi}{4}(\varepsilon_1 \cos(\frac{\pi y}{4}) + \varepsilon_3 \cos(\frac{\pi y}{4})) dV & \int\limits_{V'} \frac{\pi}{4}\varepsilon_2 \cos(\frac{\pi y}{4}) dV & \int\limits_{V'} \frac{\pi}{4}(\varepsilon_1 \cos(\frac{\pi y}{4}) + \varepsilon_3 \cos(\frac{\pi y}{4})) dV \\ \int\limits_{V-V'} \varepsilon_3 dV & \int\limits_{V-V'} (\varepsilon_1 + \varepsilon_2) dV & \int\limits_{V'} \varepsilon_3 dV & \int\limits_{V'} (\varepsilon_1 + \varepsilon_2) dV \\ \int\limits_{V-V'} \varepsilon_3 z^2 dV & \int\limits_{V-V'} (\varepsilon_1 z^2 + \varepsilon_2 z^2) dV & \int\limits_{V'} \varepsilon_3 z^2 dV & \int\limits_{V'} (\varepsilon_1 z^2 + \varepsilon_2 z^2) dV \end{bmatrix}$$

$$\dots \begin{Bmatrix} Q_{11} \\ Q_{12} \\ Q'_{11} \\ Q'_{12} \end{Bmatrix} = \begin{Bmatrix} 0 \\ 0 \\ F_3 L^3 \\ \frac{F_3 L^5}{3} \end{Bmatrix} \quad (6.30)$$

The linear system made from the virtual fields of Set 4:

$$\begin{bmatrix} \int\limits_{V-V'} \varepsilon_1 \exp(x) dV & \int\limits_{V-V'} (\varepsilon_2 \exp(x) + \varepsilon_3 \exp(x)) dV & \int\limits_{V'} \varepsilon_1 \exp(x) dV & \int\limits_{V'} (\varepsilon_2 \exp(x) + \varepsilon_3 \exp(x)) dV \\ \int\limits_{V-V'} \varepsilon_2 \exp(y) dV & \int\limits_{V-V'} (\varepsilon_1 \exp(y) + \varepsilon_3 \exp(y)) dV & \int\limits_{V'} \varepsilon_2 \exp(y) dV & \int\limits_{V'} (\varepsilon_1 \exp(y) + \varepsilon_3 \exp(y)) dV \\ \int\limits_{V-V'} \varepsilon_3 dV & \int\limits_{V-V'} (\varepsilon_1 + \varepsilon_2) dV & \int\limits_{V'} \varepsilon_3 dV & \int\limits_{V'} (\varepsilon_1 + \varepsilon_2) dV \\ \int\limits_{V-V'} \varepsilon_3 z^2 dV & \int\limits_{V-V'} (\varepsilon_1 z^2 + \varepsilon_2 z^2) dV & \int\limits_{V'} \varepsilon_3 z^2 dV & \int\limits_{V'} (\varepsilon_1 z^2 + \varepsilon_2 z^2) dV \end{bmatrix} \begin{Bmatrix} Q_{11} \\ Q_{12} \\ Q'_{11} \\ Q'_{12} \end{Bmatrix}$$

$$= \begin{Bmatrix} 0 \\ 0 \\ F_3 L^3 \\ \frac{F_3 L^5}{3} \end{Bmatrix} \quad (6.31)$$

CHAPTER 7

GENERAL DISCUSSION

7.1 Computational burden comparison

Acquired results revealed the considerable advantages of the improved approaches over classical FEMU and VFM for in-situ mechanical properties reconstruction, both in 2D and 3D. In the RMU method, improved performance was achieved through the combination of a hybrid optimization algorithm and penalty terms added to the objective function. In the RVFM, this was achieved through the implementation of regularization constraints while the addition of a gradient based optimization after MADS optimization led to no considerable improvement in the obtained results. The convergence trends of MADS optimization when implementing the RMU and the RVFM in 2D are compared in Figure 7.1. Faster decrease in the objective function value at the beginning of the identification was one of the most prominent features of the RVFM, when compared with the RMU. This clearly demonstrates that the relevant objective function in the RVFM is much smoother than in the RMU and that it thus converges quicker towards the global minimum. This remarkable feature, along with the much lower computational time required for each objective function evaluation (3 seconds for the RVFM versus 50 seconds for the RMU), emphasizes the computational

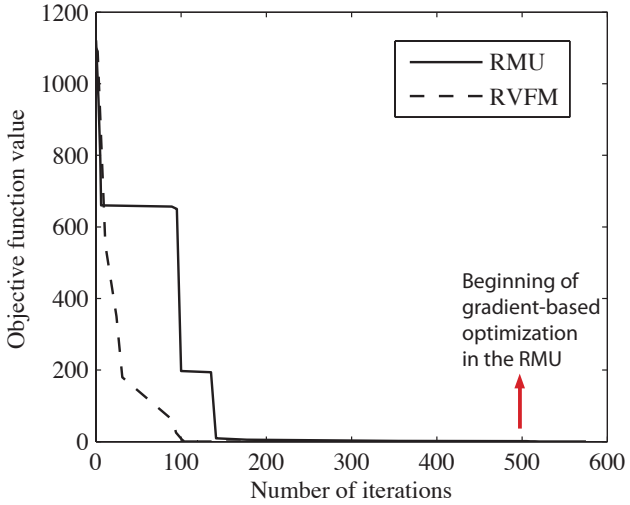

Figure 7.1: Convergence trend in the RMU and the RVFM optimization processes

efficiency of the RVFM. This advantage becomes much more important when dealing with the characterization of 3D composites constituent phases. In this study, the high computational burden associated to simulations of 3D finite element models was convincing enough to stop using the RMU method in 3D. Consider for example a finite element model of a particulate composite with a 3D microstructure. According to numerical simulations completed during the course of this study, each finite element analysis was accomplished in 18 minuses for a microstructure with a fairly fine mesh. Assuming an identification problem consisting 300 objective function evaluations, the total computational time for the whole process could be estimated to be at least 90 hours. As a comparison, for 3D microstructures, each objective function evaluation was accomplished in 15 seconds in the RVFM and the total identification time, with the same number of iterations, was approximately 90 minutes. This shows that parameters identification in 3D using the RVFM can be implemented 60 times faster than RMU, which clearly confirms the usefulness of the method for 3D problems.

7.2 Sensitivity of regularization

In this study, the regularization terms were included in order to penalize large variations in the minimizers and therefore to smooth the solutions in the presence of measurement uncertainties. By a sensible choice of the penalty parameter α (in Eq. (4.6)), which represent the relative importance of the regularization term, a reasonable convergence rate was achieved during optimizations. Large values of α implies that the identified set of parameters is regular, i.e. does not necessarily correspond to minimal discrepancy between the measured and predicted displacement fields. On the other hand, small values of α leads to a solution for which the discrepancy between the measured and predicted displacement fields is small, but the solutions might belong to an undesirable local minimum. Similarly, in the RVFM, the nonlinear regularization constraints parameters (e.g. parameter δ) must be defined reasonably so as to prevent under-constrained situations, which cause undesired minimizers oscillating behavior, or over-constrained situations for which no solution exists. For example, Table 7.1 presents the relative errors of the identified parameters for different values of δ_1 and δ_2.

It should be mentioned that these values were set to 1% of corresponding effective properties in this study. As it can be seen, by increasing the values of δ_1 and δ_2, the optimization problem becomes under-constrained and therefore discrepancies in the obtained parameters increase (especially for the fibers parameters). Identification using values less than 1% were also attempted and led to non feasible solution, which is typical of an over-constrained situation. This preliminary study reveals that the choice of the weighing parameters is also

Table 7.1: The relative errors of identified parameters with respect to the exact values using different values of δ_1 and δ_2

Method	δ_1 and δ_2	E_f $error\%$	ν_f $error\%$	E_m $error\%$	ν_m $error\%$
RVFM	1%	2.8%	10%	1.4%	2.9%
RVFM	3%	6.2%	25%	1.7%	2.6%
RVFM	5%	8.3%	23%	3.1%	3.1%

critical for the method and should be the topic of a more detailed study.

CONCLUSION

Improved inverse identification approaches based on Finite Element Model Updating (FEMU) and the Virtual Fields Method (VFM) were developed in this thesis for characterizing in-situ mechanical properties of composites constituents in 2D and 3D. This research revealed that introducing mechanically relevant constraints based on homogenization models decreased the noise sensitivity of both the FEMU and the VFM approaches, thus increasing the robustness of the inverse problem.

Improvements were first performed on the FEMU approach previously reported in the literature for different materials. Mechanical constrains, consisting of an appropriate homogenization model, were added as regularization schemes to the objective function in order to smoothen the identification process. Moreover, a hybrid strategy, which combined advantages of direct search (MADS) and gradient-based algorithms, was implemented to improve the optimization procedure. Parallelization of the optimization algorithm also contributed to the enhancement of the approach in terms of computational time. The new identification methodology, named Regularized Model Updating, was applied to noisy measured displacement fields of different 2D virtual composites and its performance was compared with the FEMU method. The results of the study revealed that the average accuracy of the solutions obtained by the new Regularized Model Updating method was much higher than that of the FEMU method. Hence, the combination of regularization constraints and a hybrid optimization algorithm demonstrated to be a powerful tool for accurate determination of composites constituents properties. Its low sensitivity to noise effects directly characterized the robustness of this new identification method.

In the second step, an inverse identification approach based on the VFM was developed for the characterization of 2D composites and was then improved. Regularization schemes, similar to those employed for the FEMU method, were included in order to enhance the stability of the identification approach. To this end, the VFM system of equations was solved within a constrained optimization framework rather than a matrix inversion method. The remarkable potential of the approach lied in its high accuracy combined with its low computational costs. The functionalities of the proposed approach was assessed by applying it to noisy full-field measured strains of several 2D virtual composites consisting of different volume fractions and mechanical properties contrasts. The efficiency of this approach was compared to that of the VFM and finite element based identification methods. Obtained results revealed the robustness of the regularized VFM, especially for accurate identification of

reinforcements phase, which exhibited much lower strains and hence had a lower signal/noise ratio than the matrix. Moreover, with similar results accuracy as that of the Regularized Model Updating method, the regularized VFM was implemented in a significantly lower calculation time. The method showed high potentials for characterizing the composites with high contrast of properties having high-order heterogeneity of strain fields. Identification using different sizes of ROI demonstrated that ROIs very close to the RVE size were optimum cases, in the sense that they led to more accurate identified parameters and can better help discriminating constitutive phases in DIC methods. The main purpose of this study was to reconcile two seemingly contradictory advantages, i.e. high reliability of the identified parameters and low computational costs.

In the third and last step, an extension of the VFM and of the regularized VFM to 3D was presented for characterizing 3D composites constitutive phases. The performance of the developed approaches was evaluated by several artificial experiments, which were applied to 3D noisy full-field strain data of several particulate composites with different microstructures. Acquired results demonstrated the capability of both identification methods for identifying mechanical properties of 3D composites constitutive materials. Similar to 2D approaches, the VFM led to lower accuracy of parameters for the reinforcements, whereas the regularized VFM delivered uniform and more accurate parameters. The study on the influence of ROI size on the accuracy of the identified parameters revealed the same trends as that in 2D.

The main contribution of this thesis was the development of accurate inverse identification approaches that are computationally efficient, while yielding appropriate composites constituent parameters in 2D and 3D.

Recommendations for future studies

In the following, important issues raised during this thesis are discussed:

- **Identification of interface mechanical properties:** Further studies are recommended to characterize the interfacial area between matrix and reinforcements. Different experimental strategies such as push-out, pull-out and indentation tests have been proposed in the literature, through which only a limited number of properties such as elastic modulii are identifiable. Studies have also been carried out to identify interfacial properties using FEMU method. However, measurement uncertainties occurring exactly in the interface area can adversely influence the associated identified parameters. The capability of the developed regularized identification approaches for identifying interface properties in a three-phase composite still remains to be investi-

gated. Strategies can be developed to perform i) simultaneous characterization of the three phases; ii) characterization of only the interface area when the mechanical properties of matrix and reinforcements are known. Once successful studies are performed in 2D, the strategy could be extended to 3D composites.

- **Damage detection and quantification:** A regularized piecewise inverse identification approach can be developed for capturing local stiffness reduction and distribution in composites. First, the target surface should be discretized to separate sections regardless of material heterogeneity. Identification algorithms based on FEMU or piecewise VFM should be developed for identifying discrete sections mechanical properties. The accuracy of identification might be degraded since large numbers of unknowns are to be identified in this method. Hence, regularization constraints similar to those employed in this study (i.e. relying on homogenized properties of material) can be included for more accurate capturing of properties distribution. The capabilities of the developed regularized piecewise approach could be compared with those of the Equation Gap Method (EGM) for damage identification. The new approach, once developed, should be validated through a series of artificial and real experiments. As an alternative application, the developed algorithm could be used as a useful and powerful tool in elastography for detecting abnormal tissues and their spatial distribution and magnitude.
- **Comparison to other regularized identification approaches:** A complement to what has been done in this thesis would be to compare the efficiency of both improved approaches with other regularized identification methods such as those developed based on adjoint weighted equation method, modified constitutive equation error method and equation error approach. One interesting matter to verify would be the efficiency of different approaches for the identification of reinforcements phase as well as interfacial area parameters.
- **Applications:** The application of the developed inverse identification approaches to real composites was not investigated in this thesis. As a complement to the simulated experiments, it would be interesting to conduct real experiments. In-situ mechanical testing should be carried out with a tensile/compression testing machine embedded into a SEM or μCT scanner for 2D or 3D imaging, respectively. The ROI size should be a good compromise between a small region that provides enough magnification for images (for better capturing strain heterogeneities in full-field measurement algorithms) and a large enough region to be a RVE. Having prepared the required full-field measured data in 2D or 3D, the regularized identification methods developed in this study could be used for constitutive parameters determination.

REFERENCES

ABRAMSON, M., AUDET, C., COUTURE, G., DENNIS, J. et LE DIGABEL, S. (2011). The NOMAD project. `http://www.gerad.ca/nomad`.

ABRAMSON, M. A. et AUDET, C. (2006). Convergence of mesh adaptive direct search to second-order stationary points. *SIAM Journal on Optimization*, 17, 606–619.

ACHENBACH, J. et ZHU, H. (1989). Effect of interfacial zone on mechanical behavior and failure of fiber-reinforced composites. *Journal of the Mechanics and Physics of Solids*, 37, 381–393.

ALBOCHER, U., OBERAI, A. A., BARBONE, P. E. et HARARI, I. (2009). Adjoint-weighted equation for inverse problems of incompressible plane-stress elasticity. *Computer Methods in Applied Mechanics and Engineering*, 198, 2412–2420.

ANGHILERI, M., CHIRWA, E., LANZI, L. et MENTUCCIA, F. (2005a). An inverse approach to identify the constitutive model parameters for crashworthiness modelling of composite structures. *Composite structures*, 68, 65–74.

ANGHILERI, M., CHIRWA, E., LANZI, L. et MENTUCCIA, F. (2005b). An inverse approach to identify the constitutive model parameters for crashworthiness modelling of composite structures. *Composite structures*, 68, 65–74.

ASMA, F. et BOUAZZOUNI, A. (2005). Finite element model updating using FRF measurements. *Shock and Vibration*, 12, 377–388.

ASMA, F. et BOUAZZOUNI, A. (2007). Finite element model updating using variable separation. *European Journal of Mechanics-A/Solids*, 26, 728–735.

ASTER, R., BORCHERS, B. et THURBER, C. (2005). *Parameter Estimation and Inverse Problems*. (International Geophysics). Academic Press.

AUDET, C. et DENNIS JR., J. E. (2006). Mesh adaptive direct search algorithms for constrained optimization. *SIAM Journal on optimization*, 17, 188–217.

AVRIL, S., BONNET, M., BRETELLE, A., GREDIAC, M., HILD, F., IENNY, P., LATOURTE, F., LEMOSSE, D., PAGANO, S., PAGNACCO, E. *ET AL.* (2008a). Overview of identification methods of mechanical parameters based on full-field measurements. *Experimental Mechanics*, 48, 381–402.

AVRIL, S., GRÉDIAC, M. et PIERRON, F. (2004). Sensitivity of the virtual fields method to noisy data. *Computational Mechanics*, 34, 439–452.

AVRIL, S., HUNTLEY, J. M., PIERRON, F. et STEELE, D. D. (2008b). 3d heterogeneous stiffness reconstruction using mri and the virtual fields method. *Experimental Mechanics*, 48, 479–494.

AVRIL, S. et PIERRON, F. (2007). General framework for the identification of constitutive parameters from full-field measurements in linear elasticity. *International Journal of Solids and Structures*, 44, 4978–5002.

AVRIL, S., PIERRON, F., PANNIER, Y. et ROTINAT, R. (2008c). Stress reconstruction and constitutive parameter identification in plane-stress elasto-plastic problems using surface measurements of deformation fields. *Experimental Mechanics*, 48, 403–419.

BALLESTER, P. J. et CARTER, J. N. (2006). Characterising the parameter space of a highly nonlinear inverse problem. *Inverse Problems in Science and Engineering*, 14, 171–191.

BANERJEE, B., WALSH, T. F., AQUINO, W. et BONNET, M. (2013). Large scale parameter estimation problems in frequency-domain elastodynamics using an error in constitutive equation functional. *Computer Methods in Applied Mechanics and Engineering*, 253, 60 – 72.

BARBONE, P. E. et OBERAI, A. A. (2007). Elastic modulus imaging: some exact solutions of the compressible elastography inverse problem. *Physics in medicine and biology*, 52, 1577.

BARBONE, P. E., OBERAI, A. A. et HARARI, I. (2007). Adjoint-weighted variational formulation for a direct computational solution of an inverse heat conduction problem. *Inverse Problems*, 23, 2325–2342.

BARNSLEY, M. F., DEVANEY, R. L., MANDELBROT, B. B., PEITGEN, D. et VOSS, R. F. (1988). *The Science of Fractal Images*. Springer-Verlag.

BAY, B. (2008). Methods and applications of digital volume correlation. *The Journal of Strain Analysis for Engineering Design*, 43, 745–760.

BAY, B., SMITH, T., FYHRIE, D. et SAAD, M. (1999a). Digital volume correlation: three-dimensional strain mapping using X-ray tomography. *Experimental Mechanics*, 39, 217–226.

BAY, B., SMITH, T., FYHRIE, D. et SAAD, M. (1999b). Digital volume correlation: Three-dimensional strain mapping using x-ray tomography. *Experimental Mechanics*, 39, 217–226.

BONNET, M. et CONSTANTINESCU, A. (2005). Inverse problems in elasticity. *Inverse problems*, 21, R1.

BOS, A. (1998). Aircraft conceptual design by genetic/gradient-guided optimization. *Engineering Applications of Artificial Intelligence*, 11, 377–382.

BOURGEOIS, N. (1994). *Caractérisation et modélisation micromécanique du comportement et de l'endommagement d'un composte à matrice métallique Al/SiCp*. Thèse de doctorat.

BUDIANSKY, B. (1965). On the elastic moduli of some heterogeneous materials. *Journal of the Mechanics and Physics of Solids*, 13, 223–227.

CANAL, L., GONZÁLEZ, C., MOLINA-ALDAREGUÍA, J., SEGURADO, J. et LLORCA, J. (2012). Application of digital image correlation at the microscale in fiber-reinforced composites. *Composites Part A: Applied Science and Manufacturing*, 43, 1630 – 1638.

CHAFRA, M., SMAOUI, H. et BEN ARFA, D. (2010). Identification of Mechanical Properties and Damage of Composites at the Mesoscale based on an Inverse Method Coupled with Homogenization. *Journal of Composite Materials*, 44, 529.

CHALAL, H., MERAGHNI, F., PIERRON, F. et GRÉDIAC, M. (2004). Direct identification of the damage behaviour of composite materials using the virtual fields method. *Composites Part A: Applied Science and Manufacturing*, 35, 841–848.

CHAPARRO, B., THUILLIER, S., MENEZES, L., MANACH, P. et FERNANDES, J. (2008). Material parameters identification: Gradient-based, genetic and hybrid optimization algorithms. *Computational Materials Science*, 44, 339–346.

CLAIRE, D., HILD, F. et ROUX, S. (2002). Identification of damage fields using kinematic measurements. *Comptes Rendus Mecanique*, 330, 729–734.

CLAIRE, D., HILD, F. et ROUX, S. (2007). Identification of a damage law by using full-field displacement measurements. *International Journal of Damage Mechanics*, 16, 179–197.

CÁRDENAS-GARCÍA, J. F. et PREIDIKMAN, S. (2006). Solution of the moiré hole drilling method using a finite-element-method-based approach. *International Journal of Solids and Structures*, 43, 6751 – 6766.

FEDELE, R., RAKA, B., HILD, F. et ROUX, S. (2009). Identification of adhesive properties in glare assemblies using digital image correlation. *Journal of the Mechanics and Physics of Solids*, 57, 1003 – 1016.

FLORENTIN, E. et LUBINEAU, G. (2010). Identification of the parameters of an elastic material model using the constitutive equation gap method. *Computational Mechanics*, 46, 521–531.

FORESTIER, R., MASSONI, E. et CHASTEL, Y. (2002). Estimation of constitutive parameters using an inverse method coupled to a 3D finite element software. *Journal of Materials Processing Technology*, 125, 594–601.

FRANCK, C., HONG, S., MASKARINEC, S., TIRRELL, D. et RAVICHANDRAN, G. (2007). Three-dimensional Full-field Measurements of Large Deformations in Soft Materials Using Confocal Microscopy and Digital Volume Correlation. *Experimental Mechanics*, 47, 427–438.

FRISWELL, M. et MOTTERSHEAD, J. (1995). *Finite element model updating in structural dynamics*. Springer.

GEERS, M., DE BORST, R. et PEIJS, T. (1999a). Mixed numerical-experimental identification of non-local characteristics of random-fibre-reinforced composites. *Composites science and technology*, 59, 1569–1578.

GEERS, M., DE BORST, R. et PEIJS, T. (1999b). Mixed numerical-experimental identification of non-local characteristics of random-fibre-reinforced composites. *Composites science and technology*, 59, 1569–1578.

GENOVESE, K., LAMBERTI, L. et PAPPALETTERE, C. (2004). A new hybrid technique for in-plane characterization of orthotropic materials. *Experimental Mechanics*, 44, 584–592.

GENOVESE, K., LAMBERTI, L. et PAPPALETTERE, C. (2005). Improved global–local simulated annealing formulation for solving non-smooth engineering optimization problems. *International Journal of solids and Structures*, 42, 203–237.

GENOVESE, K., LAMBERTI, L. et PAPPALETTERE, C. (2006). Identification of mechanical properties of bovine bones by combining ps-espi and global optimization.

GEYMONAT, G. et PAGANO, S. (2003). Identification of mechanical properties by displacement field measurement: a variational approach. *Meccanica*, 38, 535–545.

GHOSSEIN, E. et LÉVESQUE, M. (2012). A fully automated numerical tool for a comprehensive validation of homogenization models and its application to spherical particles reinforced composites. *International Journal of Solids and Structures*, 49, 1387–1398.

GHOSSEIN, E. et LEVESQUE, M. (2013). Random generation of periodic hard ellipsoids based on molecular dynamics: A computationally-efficient algorithm. *Journal of Computational Physics*, 253, 471 – 490.

GHOUATI, O. et GELIN, J.-C. (2001). A finite element-based identification method for complex metallic material behaviours. *Computational Materials Science*, 21, 57–68.

GIRAUDEAU, A., GUO, B. et PIERRON, F. (2006). Stiffness and damping identification from full field measurements on vibrating plates. *Experimental Mechanics*, 46, 777–787.

GOCKENBACH, M., JADAMBA, B. et KHAN, A. (2008). Equation error approach for elliptic inverse problems with an application to the identification of lamé parameters. *Inverse Problems in Science and Engineering*, 16, 349–367.

GOKHALE, N., BARBONE, P. et OBERAI, A. (2008). Solution of the nonlinear elasticity imaging inverse problem: the compressible case. *Inverse Problems*, 24, 045010.

GRAS, R., LECLERC, H., ROUX, S., OTIN, S., SCHNEIDER, J. et PÉRIÉ, J.-N. (2013). Identification of the Out-of-Plane Shear Modulus of a 3D Woven Composite. *Experimental Mechanics*, 53, 719–730.

GRÉDIAC, M. (1989). Principe des travaux virtuels et identification. *Comptes rendus de l'Académie des sciences. Série 2, Mécanique, Physique, Chimie, Sciences de l'univers, Sciences de la Terre*, 309, 1–5.

GRÉDIAC, M. (1996). The use of heterogeneous strain fields for the characterization of composite materials. *Composites science and technology*, 56, 841–846.

GREDIAC, M. (2004). The use of full-field measurement methods in composite material characterization: interest and limitations. *Composites Part A: applied science and manufacturing*, 35, 751–761.

GRÉDIAC, M., FOURNIER, N., PARIS, P. et SURREL, Y. (1998). Direct identification of elastic constants of anisotropic plates by modal analysis: experimental results. *Journal of sound and vibration*, 210, 643–659.

GRÉDIAC, M. et PIERRON, F. (2006). Applying the virtual fields method to the identification of elasto-plastic constitutive parameters. *International Journal of Plasticity*, 22, 602–627.

GRÉDIAC, M., PIERRON, F., AVRIL, S. et TOUSSAINT, E. (2006). The virtual fields method for extracting constitutive parameters from full-field measurements: a review. *Strain*, 42, 233–253.

GRÉDIAC, M., TOUSSAINT, E. et PIERRON, F. (2002a). Special virtual fields for the direct determination of material parameters with the virtual fields method. 1–Principle and definition. *International Journal of Solids and Structures*, 39, 2691–2705.

GRÉDIAC, M., TOUSSAINT, E. et PIERRON, F. (2002b). Special virtual fields for the direct determination of material parameters with the virtual fields method. 2—-application to in-plane properties. *International Journal of Solids and Structures*, 39, 2707–2730.

GRÉDIAC, M., TOUSSAINT, E. et PIERRON, F. (2002c). Special virtual fields for the direct determination of material parameters with the virtual fields method. 2–Application to in-plane properties. *International Journal of Solids and Structures*, 39, 2707–2730.

GRÉDIAC, M., TOUSSAINT, E. et PIERRON, F. (2003). Special virtual fields for the direct determination of material parameters with the virtual fields method. 3. application

to the bending rigidities of anisotropic plates. *International Journal of Solids and Structures*, 40, 2401–2419.

GREGORY, J. R. et SPEARING, S. (2005). Nanoindentation of neat and in situ polymers in polymer–matrix composites. *Composites science and technology*, 65, 595–607.

GUICCIARDI, S., MELANDRI, C., SILVESTRONI, L. et SCITI, D. (2008). Indentation grid analysis of nanoindentation bulk and in situ properties of ceramic phases. *Journal of Materials Science*, 43, 4348–4352.

HADAMARD, J. (1902). Sur les problemes aux derivees partielles et leur signification physique. *Princeton University Bulletin*, 13, 49–52.

HAN, B., POST, D. et IFJU, P. (2001). Moiré interferometry for engineering mechanics: current practices and future developments. *The Journal of Strain Analysis for Engineering Design*, 36, 101–117.

HARDIMAN, M., VAUGHAN, T. et MCCARTHY, C. (2012). The effect of fibre constraint in the nanoindentation of fibrous composite microstructures: A finite element investigation. *Computational Materials Science*, 64, 162–167.

HASHIN, Z. et SHTRIKMAN, S. (1963). A variational approach to the theory of the elastic behaviour of multiphase materials. *Journal of the Mechanics and Physics of Solids*, 11, 127–140.

HILD, F. et ROUX, S. (2006a). Digital image correlation: from displacement measurement to identification of elastic properties–a review. *Strain*, 42, 69–80.

HILD, F. et ROUX, S. (2006b). Digital image correlation: from displacement measurement to identification of elastic properties – a review. *Strain*, 42, 69–80.

HOOKE, R. et JEEVES, T. A. (1961). Direct search solution of numerical and statistical problems. *J. ACM*, 8, 212–229.

IENNY, P., CARO-BRETELLE, A.-S. et PAGNACCO, E. (2009). Identification from measurements of mechanical fields by finite element model updating strategies. *European Journal of Computational Mechanics/Revue Européenne de Mécanique Numérique*, 18, 353–376.

JADAMBA, B., KHAN, A. A. et RACITI, F. (2008). On the inverse problem of identifying Lamé coefficients in linear elasticity. *Computers & Mathematics with Applications*, 56, 431–443.

JOENATHAN, C. (1997). Speckle photography, shearography, and espi. *Optical measurement techniques and applications*, 151–182.

KAIPIO, J. et SOMERSALO, E. (2007). Statistical inverse problems: discretization, model reduction and inverse crimes. *Journal of Computational and Applied Mathematics*, 198, 493–504.

KAJBERG, J. et LINDKVIST, G. (2004). Characterisation of materials subjected to large strains by inverse modelling based on in-plane displacement fields. *International Journal of Solids and Structures*, 41, 3439 – 3459.

KANG, Y., LIN, X. et QIN, Q. (2004). Inverse/genetic method and its application in identification of mechanical parameters of interface in composite. *Composite structures*, 66, 449–458.

KANIT, T., FOREST, S., GALLIET, I., MOUNOURY, V. et JEULIN, D. (2003). Determination of the size of the representative volume element for random composites: statistical and numerical approach. *International Journal of Solids and Structures*, 40, 3647–3679.

KIM, G. et PARK, Y. (2004). An improved updating parameter selection method and finite element model update using multiobjective optimisation technique. *Mechanical Systems and Signal Processing*, 18, 59–78.

KIM, J.-H., PIERRON, F., WISNOM, M. et SYED-MUHAMAD, K. (2007). Identification of the local stiffness reduction of a damaged composite plate using the virtual fields method. *Composites Part A: Applied Science and Manufacturing*, 38, 2065–2075.

KOYANAGI, J., SHAH, P. D., KIMURA, S., HA, S. K. et KAWADA, H. (2009). Mixed-mode interfacial debonding simulation in single-fiber composite under a transverse load. *Journal of Solid Mechanics and Materials Engineering*, 3, 796–806.

LE DIGABEL, S. (2011). Algorithm 909: NOMAD: Nonlinear optimization with the MADS algorithm. *ACM Transactions on Mathematical Software (TOMS)*, 37, 1–44.

LE DIGABEL, S., ABRAMSON, M., AUDET, C. et DENNIS, J. (2010). Parallel versions of the MADS algorithm for black-box optimization. *Optimization days*. Montreal.

LE MAGOROU, L., BOS, F. et ROUGER, F. (2002). Identification of constitutive laws for wood-based panels by means of an inverse method. *Composites Science and Technology*, 62, 591–596.

LECOMPTE, D., SMITS, A., SOL, H., VANTOMME, J. et VAN HEMELRIJCK, D. (2007). Mixed numerical-experimental technique for orthotropic parameter identification using biaxial tensile tests on cruciform specimens. *International Journal of Solids and Structures*, 44, 1643–1656.

LECOMPTE, D., SOL, H., VANTOMME, J. et HABRAKEN, A. (2005). Identification of elastic orthotropic material parameters based on espi measurements. *SEM annual conference and exposition on experimental and applied mechanics*.

LEE, H. S., PARK, C. J. et PARK, H. W. (2000). Identification of geometric shapes and material properties of inclusions in two-dimensional finite bodies by boundary parameterization. *Computer Methods in Applied Mechanics and Engineering*, 181, 1 – 20.

LEWIS, R. M. et TORCZON, V. (1999). Pattern search algorithms for bound constrained minimization. *SIAM J. on Optimization*, 9, 1082–1099.

LEWIS, R. M. et TORCZON, V. (2000). Pattern search methods for linearly constrained minimization. *SIAM Journal on Optimization*, 10, 917–941.

LIELENS, G., PIROTTE, P., COUNIOT, A., DUPRET, F. et KEUNINGS, R. (1998). Prediction of thermo-mechanical properties for compression moulded composites. *Composites Part A: Applied Science and Manufacturing*, 29, 63–70.

LUBINEAU, G. (2009). A goal-oriented field measurement filtering technique for the identification of material model parameters. *Computational Mechanics*, 44, 591–603.

MARANON, A., NURSE, A. D. et HUNTLEY, J. M. (2003). Characterization of a single delamination using geometric moments and genetic algorithms. *Optical Engineering*, 42, 1328–1336.

MARTYNIUK, K., SØRENSEN, B. F., MODREGGER, P. et LAURIDSEN, E. M. (2013). 3d in situ observations of glass fibre/matrix interfacial debonding. *Composites Part A: Applied Science and Manufacturing*, 55, 63 – 73.

MEUWISSEN, M., OOMENS, C., BAAIJENS, F., PETTERSON, R. et JANSSEN, J. (1998). Determination of the elasto-plastic properties of aluminium using a mixed numerical-experimental method. *Journal of Materials Processing Technology*, 75, 204–211.

MOLIMARD, J., LE RICHE, R., VAUTRIN, A. et LEE, J. (2005). Identification of the four orthotropic plate stiffnesses using a single open-hole tensile test. *Experimental Mechanics*, 45, 404–411.

MORI, T. et TANAKA, K. (1973). Average stress in matrix and average elastic energy of materials with misfitting inclusions. *Acta metallurgica*, 21, 571–574.

MORTAZAVI, F., GHOSSEIN, E., LÉVESQUE, M. et VILLEMURE, I. (2014). High resolution measurement of internal full-field displacements and strains using global spectral digital volume correlation. *Optics and Lasers in Engineering*, 55, 44–52.

MORTAZAVI, F., LÉVESQUE, M. et VILLEMURE, I. (2011a). Improved Spectral Approach for Continuous Displacement Measurements From Digital Images. *Proceeding of the SEM Annual Conference*. Uncasville.

MORTAZAVI, F., LÉVESQUE, M. et VILLEMURE, I. (2011b). On The Application of a Hybrid Spectral Approach in the Image-Based Measurement of Displacements at Micro-Scale in Composites. *Proceeding of 26th Annual Technical Conference of the American Society for Composites*. Montreal.

MORTAZAVI, F., LÉVESQUE, M. et VILLEMURE, I. (2013a). 3D FULL-FIELD DISPLACEMENTS/STRAINS MEASUREMENTS IN COMPOSITES AT MICRO-SCALE. *Proceeding of ICCM19 Conference*. Montreal.

MORTAZAVI, F., LÉVESQUE, M. et VILLEMURE, I. (2013b). Image-based continuous displacement measurements using an improved spectral approach. *Strain*, 49, 233–248.

MOSEGAARD, K. et SAMBRIDGE, M. (2002). Monte carlo analysis of inverse problems. *Inverse Problems*, 18, R29.

MOULART, R., AVRIL, S. et PIERRON, F. (2006). Identification of the through-thickness rigidities of a thick laminated composite tube. *Composites Part A: Applied Science and Manufacturing*, 37, 326–336.

MOULART, R., PIERRON, F., HALLETT, S. et WISNOM, M. (2011). Full-field strain measurement and identification of composites moduli at high strain rate with the virtual fields method. *Experimental mechanics*, 51, 509–536.

MOULINEC, H. et SUQUET, P. (1998a). A numerical method for computing the overall response of nonlinear composites with complex microstructure. *Computer methods in applied mechanics and engineering*, 157, 69–94.

MOULINEC, H. et SUQUET, P. (1998b). A numerical method for computing the overall response of nonlinear composites with complex microstructure. *Computer Methods in Applied Mechanics and Engineering*, 157, 69 – 94.

MOUSSAWI, A., LUBINEAU, G., FLORENTIN, E. et BLAYSAT, B. (2013). The Constitutive Compatibility Method for identification of material parameters based on full-field measurements. *Computer Methods in Applied Mechanics and Engineering*, 1–14.

NAIR, A., TAGGART, D. et VETTER, F. (2007). Optimizing cardiac material parameters with a genetic algorithm. *Journal of biomechanics*, 40, 1646.

NAN, L., PENGDONG, G., YONGQUAN, L. et Y., W. (2010). The Implementation and Comparison of Two Kinds of Parallel Genetic Algorithm Using Matlab. *Ninth International*

Symposium on Distributed Computing and Applications to Business, Engineering and Science.

NELDER, J. A. et MEAD, R. (1965). A simplex method for function minimization. *The Computer Journal*, 7, 308–313.

NOCEDAL, J. et WRIGHT, S. (1999). *Numerical optimization*. Springer verlag.

OBERAI, A., GOKHALE, N., DOYLEY, M. et BAMBER, J. (2004). Evaluation of the adjoint equation based algorithm for elasticity imaging. *Physics in Medicine and Biology*, 49, 2955.

OKADA, H., FUKUI, Y. et KUMAZAWA, N. (1999). An Inverse Analysis Determining the Elastic-Plastic Stress-Strain Relationship Using Nonlinear Sensitivities. *Computer Modeling and Simulation in Engineering*, 4, 176–185.

PERERA, R. et RUIZ, A. (2008). A multistage fe updating procedure for damage identification in large-scale structures based on multiobjective evolutionary optimization. *Mechanical Systems and Signal Processing*, 22, 970–991.

PIERRON, F., ALLOBA, E., SURREL, Y. et VAUTRIN, A. (1998). Whole-field assessment of the effects of boundary conditions on the strain field in off-axis tensile testing of unidirectional composites. *Composites Science and Technology*, 58, 1939–1947.

PIERRON, F. et GRÉDIAC, M. (2000). Identification of the through-thickness moduli of thick composites from whole-field measurements using the iosipescu fixture: theory and simulations. *Composites Part A: Applied Science and Manufacturing*, 31, 309–318.

PIERRON, F. et GRÉDIAC, M. (2012). *The Virtual Fields Method*. Springer, New York.

PIERRON, F., VERT, G., BURGUETE, R., AVRIL, S., ROTINAT, R. et WISNOM, M. (2007). Identification of the orthotropic elastic stiffnesses of composites with the virtual fields method: sensitivity study and experimental validation. *Strain*, 43, 250–259.

PIERRON, F., ZHAVORONOK, S. et GRÉDIAC, M. (2000a). Identification of the through-thickness properties of thick laminated tubes using the virtual fields method. *International Journal of Solids and Structures*, 37, 4437–4453.

PIERRON, F., ZHAVORONOK, S. et GRÉDIAC, M. (2000b). Identification of the through-thickness properties of thick laminated tubes using the virtual fields method. *International Journal of Solids and Structures*, 37, 4437–4453.

PROMMA, N., RAKA, B., GRÉDIAC, M., TOUSSAINT, E., LE CAM, J.-B., BALANDRAUD, X. et HILD, F. (2009). Application of the virtual fields method to mechanical

characterization of elastomeric materials. *International Journal of Solids and Structures*, 46, 698–715.

RAHMANI, B., MORTAZAVI, F., VILLEMURE, I. et LEVESQUE, M. (2013a). A new approach to inverse identification of mechanical properties of composite materials: Regularized model updating. *Composite Structures*, 105, 116 – 125.

RAHMANI, B., VILLEMURE, I. et LÉVESQUE, M. (2013b). Regularized virtual field method for mechanical properties identification of composite materials. Manuscript submitted on Sep. 27, 2013 in Computer Methods in Applied Mechanics and Engineering.

RAMAULT, C., HEMELRIJCK, M. A. S. H. V., LECOMPTE, D., E., L. et W., V. P. (2009). Development of an Inverse method for Material Characterization using a Biaxially Loaded Cruciform Composite Specimen. *Proceeding of the SEM Annual Conference*.

SALENÇON, J. (2001). *Handbook of continuum mechanics: general concepts, thermoelasticity*. Springer Verlag.

SANPAZ (2008). Material element with stress tensor vectors and its components. `http://en.wikipedia.org/wiki/File:Stress_components_in_element.png`.

SCHAJER, G. S. et STEINZIG, M. (2005). Full-field calculation of hole drilling residual stresses from electronic speckle pattern interferometry data. *Experimental Mechanics*, 45, 526–532.

SILVA, G. H., LE RICHE, R., MOLIMARD, J. et VAUTRIN, A. (2009). Exact and efficient interpolation using finite elements shape functions. *European Journal of Computational Mechanics/Revue Européenne de Mécanique Numérique*, 18, 307–331.

SPRINGMANN, M. et KUNA, M. (2003). Identification of material parameters of the Rousselier model by non-linear optimization. *Computational materials science*, 26, 202–209.

SZTEFEK, P. et OLSSON, R. (2008). Tensile stiffness distribution in impacted composite laminates determined by an inverse method. *Composites Part A: Applied Science and Manufacturing*, 39, 1282–1293.

SZTEFEK, P. et OLSSON, R. (2009). Nonlinear compressive stiffness in impacted composite laminates determined by an inverse method. *Composites Part A: Applied Science and Manufacturing*, 40, 260–272.

TORCZON, V. (1997). On the convergence of pattern search algorithms. *SIAM Journal on Optimization*, 7, 1–25.

TORCZON, V. *ET AL.* (1997). On the convergence of pattern search algorithms. *SIAM Journal on optimization*, 7, 1–25.

TORQUATO, S. (1991). Random heterogeneous media: microstructure and improved bounds on effective properties. *Applied mechanics reviews*, 44, 37.

TOUSSAINT, E., GRÉDIAC, M. et PIERRON, F. (2006). The virtual fields method with piecewise virtual fields. *International Journal of Mechanical Sciences*, 48, 256–264.

TUCKER III, C. L. et LIANG, E. (1999). Stiffness predictions for unidirectional short-fiber composites: review and evaluation. *Composites science and technology*, 59, 655–671.

VAN RATINGEN, M. (1994). *Mechanical identification of inhomogeneous solids: a mixed numerical experimental approach*. Thèse de doctorat, Eindhoven University of Technology.

VAN SOEST, A. et CASIUS, L. (2003). The merits of a parallel genetic algorithm in solving hard optimization problems. *Journal of biomechanical engineering*, 125, 141.

WANG, J., QIN, Q., KANG, Y., LI, X. et RONG, Q. (2010). Viscoelastic adhesive interfacial model and experimental characterization for interfacial parameters. *Mechanics of Materials*, 42, 537–547.

WEBER, B., PAULTRE, P. et PROULX, J. (2007). Structural damage detection using nonlinear parameter identification with tikhonov regularization. *Structural Control and Health Monitoring*, 14, 406–427.

WRIGHT, P., MOFFAT, A., SINCLAIR, I. et SPEARING, S. (2010). High resolution tomographic imaging and modelling of notch tip damage in a laminated composite. *Composites Science and Technology*, 70, 1444–1452.

ZAOUI, A. (2002). Continuum micromechanics: survey. *Journal of Engineering Mechanics*, 128, 808–816.

ZHOU, J., L., Q. et CHEN, G. (2006). New inverse method for identification of constitutive parameters. *Transactions of Nonferrous Metals Society of China*, 16, 148 – 152.